

DOCTORAL THESIS

Micromechanical modeling and experimental characterization of sound and degraded wood cell walls

submitted in satisfaction of the requirements for the degree
Doctor of Science in Civil Engineering
of the Vienna University of Technology, Faculty of Civil Engineering

DISSERTATION

Mikromechanische Modellierung und experimentelle Charakterisierung von intakten und abgebauten Holzzellwänden

ausgeführt zum Zwecke der Erlangung des akademischen Grades eines
Doktors der technischen Wissenschaften
eingereicht an der Technischen Universität Wien, Fakultät für Bauingenieurwesen

von

Leopold Wagner

Matr.Nr.: 0425856

Leitermayergasse 50/9, 1180 Wien, Österreich

Gutachter:

Assoc. Prof. Dipl.-Ing. Dr. techn. **Karin de Borst**

School of Engineering

University of Glasgow

Glasgow G12 8LT, Schottland, Vereinigtes Königreich Großbritannien und Nordirland

Univ. Prof. Dipl.-Ing. Dr. techn. DDr.h.c. **Josef Eberhardsteiner**

Institut für Mechanik der Werkstoffe und Strukturen

Technische Universität Wien

Karlsplatz 13/202, 1040 Wien, Österreich

Univ. Prof. Dr. **Ingo Burgert**

Institut für Baustoffe/Wood Materials Science

Eidgenössische Technische Hochschule Zürich

Stefano-Francini-Platz 3, 8093 Zürich, Schweiz

Wien, im Juni 2014

.....

Acknowledgements

This thesis is based on my work performed as a research assistant at the Institute for Mechanics of Materials and Structures (IMWS), Vienna University of Technology, during the last three and a half years. It would not have been possible without the help of numerous people of whom I would like to address the most important ones in the following.

First of all, I would like to thank Dr. Karin de Borst for opening up the opportunity to pursue a PhD thesis at the IMWS and for her continuous guidance and support throughout the last years - especially after she had left Vienna and she had to do it via Email and Skype.

I am deeply indebted to Dr. Thomas K. Bader for his guidance during this thesis and especially for being there on a daily basis. It was a pleasure to work with him for the last years, and his patience and encouragement helped me through the tough times - although there were hardly any.

Prof. Josef Eberhardsteiner, dean of the Faculty of Civil Engineering and former head of the IMWS as well as the current head of the IMWS Prof. Christian Hellmich are thanked for their support as well as for creating a positive working environment. Prof. Ingo Burgert (ETH Zürich, Switzerland) is thanked for serving as co-examiner of this thesis.

I am thankful to my current and former colleagues in the "wood group" DI Christoph Wikete, DI Michael Schweigler, DI Georg Kandler, DI Wolfgang Lederer, DI Georg Hochreiner, DI Markus Lukacevic, Dr. Josef Füssl, Dr. Stefan Gloimüller, Dr. Johannes Eitelberger and Dr. Michael Dorn as well as to DI Viktória Vass. Gabriele Ostrovski, Astrid Schuh and Mag.(FH) Martina Pöll are thanked for the smooth and quick handling of all administrative issues.

It was a pleasure to cooperate with Dr. Karin Fackler and DI Thomas Ters (Institute of Chemical Engineering, Vienna University of Technology) within the "Innovative Project 2010: Microstructural and chemical characterization of softwood degradation by basidiomycetes and its effects on the mechanical behavior". The Vienna University of Technology is acknowledged for the financial support of this research project. Dr. David Auty (Département des sciences du bios et de la forêt, Université Laval, Quebec, Canada), DI Clémence Bos (currently Institute for Applied Materials, Karlsruhe Institute of Technology, Germany) and Dr. Lauri Rautkari (Department of Forest Products Technology, Aalto University, Helsinki, Finland) are also thanked for their cooperation.

The European Cooperation in Science and Technology (COST) is thanked for supporting a Short Term Scientific Mission (STSM) to the Max Planck Institute for Colloids and Interfaces, Potsdam-Golm, Germany, via the COST Action FP0802 "Experimental and Computational Micro-Characterization Techniques in Wood Mechanics" (special thanks go to Dr. Michaela Eder, the host of the STSM).

Finally I want to thank Martina for her restless support. Without her, completing this thesis would not have been possible.

Abstract

Wood is a natural composite material. Its mechanical properties are determined by its inherent hierarchical microstructure. These so called structure function relationships are only beginning to be understood. The microstructure and composition of wood, and in consequence also its mechanical properties, show great natural variability, which is further enhanced by water uptake and fungal decay. The aim of this thesis is to improve the current understanding of structure function relations of wood. Investigations on the cell wall scale enable ruling out the dominant effect of mass density – and its variations – on the macroscopic mechanical behaviour of wood. Thus, experimental assessment as well as micromechanical modeling of the cell wall stiffness represent the main focus herein.

Wood cell wall stiffnesses are experimentally assessed by means of nanoindentation. Although this method has become a common tool in wood science, effects of sample preparation are a subject of ongoing discussion. A contribution to this discussion is presented, in which effects of individual steps involved in sample preparation are investigated, and a protocol for the assessment of different cell wall layers is proposed. Using this protocol, the effects of (1) water uptake during wood moisture changes, (2) of natural microstructural variability and (3) of wood modifications by decay fungi on wood cell wall stiffnesses are experimentally assessed. In order to identify structure function relations, the microstructure and composition of wood cell walls has to be determined as well. For this purpose, a broad variety of methods is discussed and applied.

The mechanical characterization of wood cell walls reveals common trends of cell wall softening upon moisture uptake across wood species, distinct trends of cell wall stiffness within annual rings, as well as cell wall stiffness changes upon fungal degradation.

Linking the micromechanical to the microstructural and compositional data can be performed using multivariate data analyses, revealing correlations between individual characteristics. When applied to investigating effects of fungal decay, this method could reveal correlations in a vast and highly variable set of compositional, microstructural and micromechanical data. Another – deterministic – approach to establish these links is micromechanical modeling. Using microstructural and compositional data as model input, predictions of cell wall stiffnesses can be compared to experimentally determined ones. For this purpose, a multiscale mechanical model for wood cell wall stiffness, based on homogenization methods, is presented. Using this model, statistical observations can now be elevated to a physical level. Micromechanical modeling reveals the influence of both microstructural and compositional variability on cell wall stiffness trends within trees at different length scales. Micromechanical modeling of fungal degraded wood cell wall stiffness can be used to test hypotheses of – yet unknown – effects of fungal decay, based on the aforementioned statistical observations.

Kurzfassung

Holz ist ein natürliches Kompositmaterial. Die mechanischen Eigenschaften werden von seiner hierarchischen Mikrostruktur bestimmt. Diese so genannten Struktur-Funktions Beziehungen werden erst teilweise verstanden. Die Mikrostruktur und Zusammensetzung von Holz, und in Folge auch das mechanische Verhalten, zeigt große Variabilität, welche während der Wasseraufnahme oder des Abbaus durch Pilze, noch verstärkt werden. Ziel dieser Arbeit ist es das Verständnis der Struktur-Funktions Beziehungen in Holz zu verbessern. Untersuchungen an Holzzellwänden ermöglichen es, den dominanten Effekt der Massendichte von Holz – und seiner Variabilität – auf das mechanische Verhalten zu umgehen. Deshalb liegt der Fokus dieser Arbeit auf der experimentellen Erfassung als auch der mikromechanischen Modellierung von Holzzellwandsteifigkeiten.

Holzzellwandsteifigkeiten werden experimentell mittels Nanoindentation bestimmt. Trotz der verbreiteten Anwendung von Nanoindentation in der Holzforschung sind Effekte der Probenvorbereitung nicht restlos geklärt. Eine Untersuchung von Effekten verschiedener Schritte der Probenvorbereitung wird präsentiert und Testprotokolle für einzelne Zellwandschichten vorgeschlagen. Diese wurden dann auch verwendet, um Einflüsse von (1) Wasseraufnahme bei Änderung der Holzfeuchte, (2) von natürlicher Mikrostrukturvariabilität, und (3) von Modifikationen durch holzerstörende Pilze auf die Zellwandsteifigkeiten experimentell zu untersuchen. Um Struktur-Funktions Beziehungen zu identifizieren, müssen auch Mikrostruktur und Zusammensetzung von Holz bestimmt werden. Zu dem Zweck wurde ein breites Spektrum an Methoden angewandt.

Generelle Trends von Zellwandsteifigkeiten während des Erweichens von Holzzellwänden verschiedener Holzarten durch Wasseraufnahme, Steifigkeitstrends in Jahresringen, sowie Änderungen der Steifigkeiten während des Abbaus durch holzerstörende Pilze werden gezeigt.

Zusammenhänge zwischen den mikromechanischen, mikrostrukturellen und chemischen Daten zur Zusammensetzung der Holzzellwände können mittels Multivariater Datenanalysemethoden gefunden werden, welche Korrelationen zwischen einzelnen Variablen identifizieren. Angewandt auf von Pilzen abgebaute Holzzellwände zeigen diese Methoden Korrelationen in einem großen, durch hohe Variabilität gekennzeichneten, Datenset. Ein anderer – deterministischer – Zugang ist die mikro-mechanische Modellierung. Mit den Daten zu Mikrostruktur und Zusammensetzung als Input, können Vorhersagen von Zellwandsteifigkeiten berechnet und mit experimentellen Ergebnissen verglichen werden. Zu diesem Zweck wird ein mechanisches Mehrskalmodell für die Zellwandsteifigkeit, basierend auf Homogenisierungsmethoden, präsentiert. Mithilfe dieses Modells können statistische Beobachtungen auf ein physikalisches Niveau gehoben werden. Der Einfluss der Variabilität von Mikrostruktur und Zusammensetzung auf Trends von Zellwandsteifigkeiten auf unterschiedlichen Längenskalen innerhalb eines Baumes wird gezeigt. Mikromechanische Modellierung der Steifigkeiten von, von Pilzen abgebauten, Holzzellwänden ermöglicht das Testen von Hypothesen zu – bisher unbekanntem – Effekten des Abbaus, basierend auf den zuvor erwähnten statistischen Beobachtungen.

Contents

Introduction	1
Motivation	1
Wood as Natural Hierarchical Material	1
Wood-Water Interactions	3
Wood Variability	4
Biodegradation of Wood	4
Micromechanics of Wood	5
Nanoindentation of Wood Cell Walls	7
Multiscale Micromechanical Modeling	9
Research Objectives and Outline of the Thesis	15
Contribution of the Author	17
1 Nanoindentation of Wood Cell Walls: Effects of Sample Preparation and Indentation Protocol (Wagner et al., 2014a)	19
1.1 Introduction	20
1.2 Materials and Methods	22
1.2.1 Samples	22
1.2.2 Drying of Wood Samples	22
1.2.3 Embedment and Preparation of NI-Specimens	23
1.2.4 Nanoindentation Tests	25
1.3 Results and Discussion	26
1.3.1 Edge Effects in the Cell Corner Middle Lamella (CCML)	26
1.3.2 Effects of Sample Drying	27
1.3.3 Effects of Embedding Medium	29
1.4 Concluding Remarks	31
2 Effect of Water on the Mechanical Properties of Wood Cell Walls – Results of a Nanoindentation Study (Wagner et al., 2014d)	33
2.1 Introduction	34
2.2 State-of-the-art	35
2.3 Materials and Methods	35
2.3.1 Samples	35
2.3.2 Nanoindentation	36
2.3.3 Environmental Scanning Electron Microscopy (ESEM)	37

2.3.4	Dynamic Vapour Sorption (DVS)	37
2.4	Results	38
2.4.1	ESEM	38
2.4.2	DVS	39
2.4.3	Nanoindentation	39
2.5	Discussion	40
2.5.1	Indentation Moduli	40
2.5.2	Creep Values	45
2.6	Conclusions	46
3	Key parameters controlling stiffness variability within trees: a multiscale experimental-numerical approach (Wagner et al., 2013)	49
3.1	Introduction	50
3.2	Methods	52
3.2.1	Samples	52
3.2.2	SilviScan-3 TM Measurements	53
3.2.3	Local Microfibril Angle Measurements	53
3.2.4	Local Chemical Composition by Thermogravimetric Analysis	54
3.2.5	Ultrasonic Testing	55
3.2.6	Nanoindentation Tests	56
3.2.7	Micromechanical Modeling	56
3.3	Results and Discussion	57
3.3.1	Experimental	57
3.3.2	Micromechanical Modeling	63
3.4	Conclusions	67
	Appendix 1: Multiscale Micromechanical Model for Softwood Stiffness	70
	Converting Mass Fractions to Volume Fractions	70
	Stiffness of the 'Universal' Phases	70
	Continuum Micromechanical Model for the Stiffness of the S2 Cell Wall Layer	71
	Laminate Theory to estimate Softwood Stiffness	73
4	A Combined View on Composition, Molecular Structure and Micromechanics of Fungal Degraded Softwood (Wagner et al., 2014c)	75
4.1	Introduction	76
4.2	Experimental Procedures	77
4.2.1	Materials	77
4.2.2	Methods Outline	78
4.2.3	Attenuated Total Reflectance Fourier Transform Infrared Spectroscopy (ATR FT-IR)	78
4.2.4	Wide Angle X-Ray Scattering (WAXS)	79
4.2.5	Wet Chemical Analysis	79
4.2.6	Nanoindentation	80
4.2.7	Multivariate Data Analysis (MVA)	80

4.3	Results and Discussion	81
4.3.1	Wet Chemical Analysis	81
4.3.2	Wide Angle X-Ray Scattering	81
4.3.3	Nanoindentation	82
4.3.4	Multivariate Analysis of Micromechanical, Microstructural and Chemical Characteristics	83
4.3.5	Relation between ATR FT-IR Spectra and Micromechanical Data	85
4.4	Conclusions	87
	Appendix 2: Compositional, Microstructural and Micromechanical Data . . .	89
5	Fungal Degradation of Softwood Cell Walls: Enhanced Insight through Mi- cromechanical Modeling (Wagner et al., 2014b)	93
5.1	Introduction	94
5.2	Materials and Methods	95
5.2.1	Wood Cell Wall Structure	95
5.2.2	Homogenization Theory - Continuum Micromechanics	96
5.2.3	Multiscale Micromechanical Model for Sound Wood Cell Walls	97
5.2.4	Modeling Fungal Degradation	100
5.2.5	Prediction of Nanoindentation Moduli	101
5.2.6	Microstructural Input Parameters	101
5.3	Results and Discussion	102
5.3.1	Experimental Observations on Cell Wall Stiffness upon Fungal Degradation	102
5.3.2	Results from Micromechanical Modeling	103
5.4	Conclusions	110
	Appendix 3: Compositional and Microstructural Input Data	111
	Appendix 4: Multiscale Micromechanical Model for Fungal Degraded Wood Cell Walls	116
	Distributing the Overall Mass Fractions to the S2 Layer and the Com- pound Middle Lamella	116
	Determining the Moisture Content of the S2 layer and the Middle Lamella	116
	Converting Mass Fractions to Volume Fractions	117
	Stiffness of the 'Universal' Phases	117
	Stiffness of the S2 Cell Wall Layer (S2)	118
	Stiffness of the Compound Middle Lamella (CML)	119
	Summary and Outlook	121
	Main Findings	121
	Perspectives and future research studies	123
	Bibliography	125
	Publications and Conference Contributions	143
	Curriculum Vitae	145

Introduction

Motivation

Wood has always been used as building material as well as to manufacture tools. Therefore the mechanical properties of wood have been a subject of – mainly experimental – investigations for a long time (e.g. see early works of Andréa (1790) or Heß (1895)). Even though research has nowadays gained deep insight into the mechanical properties of wood, the underlying causal relationships between the wood microstructure and its mechanical properties, especially at the cell wall level, are only started to be understood. Thus, the aim of this thesis is to improve the current understanding of these structure-function relationships. The main focus herein lies on the cell wall level. Special emphasis is given to wood-water interactions, to the natural variability of wood properties and to the effects of biodegradation and its implications on the mechanical properties of wood cell walls.

Wood as Natural Hierarchical Material

Wood is produced by a large number of plants and has to fulfil a multitude of purposes in the living organism. Next to storage and transportation of water and nutrients, providing mechanical stability is the most important function of woody plant tissues. Many of these plants, producing wood tissue, appear as trees and their respective tree stems are usually utilized as construction material. The fact that living trees are continuously growing enables the tree to adjust the produced wood material to meet the current requirements given by its environment (Burgert and Jungnikl, 2004; Weinkamer and Fratzl, 2011). This is expressed e.g. in terms of the formation of so called earlywood (EW) and latewood (LW) in temperate zones with growth seasons, or in the formation of reaction wood tissue, i.e. tension and compression wood, enabling the tree to react to external forces. To be able to efficiently accomplish these tasks, the material wood is hierarchically structured (Côté, 1965; Lakes, 1993; Booker and Sell, 1998; Burgert, 2006; Fratzl and Weinkamer, 2007).

This hierarchical microstructure of wood constitutes at multiple levels of observation, separated by at least one length scale (Figure 1). Growth rings, formed by alternating layers of EW and LW, are still visible by the naked eye (Figure 1a). The proportion of EW and LW within the annual rings is one of the main factors determining the overall

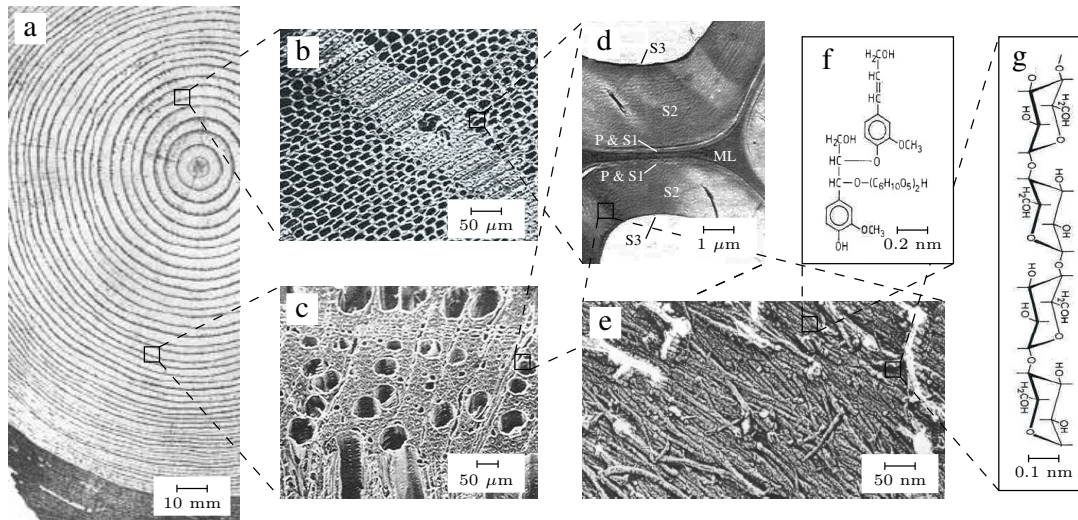


Figure 1: Hierarchical microstructure of wood: (a) cross-section of a log (*Pinus ponderosa*)⁽¹⁾, (b) transverse section through a softwood (*Pinus sylvestris*)⁽²⁾, (c) transverse section through a hardwood (*Fagus sylvatica*)⁽²⁾, (d) section through the cell wall, showing the primary (P) and the three secondary cell wall layers (S1, S2 and S2) as well as the middle lamella (ML) (*Picea abies*)⁽²⁾, (e) fibrillar structure of the S2 cell wall layer (*Pinus thunbergii*)⁽³⁾, (f) chemical structure of lignin⁽²⁾, (g) chemical structure of the cellulose chain⁽²⁾; ⁽¹⁾...from Ross (2010), ⁽²⁾...from Fengel and Wegener (2003), ⁽³⁾...from Hafrén et al. (1999); reproduced from Hofstetter et al. (2005)

mass density. These EW and LW layers are composed of individual wood cells. Depending on the wood species, different types of cells can be found. In gymnosperm trees, i.e. softwood trees (Figure 1b), mainly tracheids are found, fulfilling both tasks of transport and providing mechanical stability (Plomion et al., 2001). In angiosperm trees, i.e. hardwood trees (Figure 1c), these tasks are divided to separate cell types, where transport issues are fulfilled by vessels and the mechanical support is provided by fibers in between the vessels (Déjardin et al., 2010). All wood cells appear as hollow fibers, having lengths of 1-7 mm and diameters of 20-60 μm in softwood and hardwood. The cells exhibit a multi-layered cell wall of 2-5 μm total thickness, and individual wood cells are connected by the so called middle lamella (ML), which ensures the load transfer between them (Figure 1d). A wood cell wall consists of a primary cell wall (P layer) and three secondary cell wall layers (S1, S2 and S3 layer). Of these layers, the S2 layer is the dominant layer by volume, comprising up to about 80% of the entire cell wall (Côté, 1965; Page, 1976; Fengel and Wegener, 2003). These layers are built from a composite material, consisting of cellulose fibrils embedded in a matrix composed of hemicelluloses, lignin and extractives (Figure 1e-g). In the S2 layer, these cellulose fibrils are oriented in parallel and inclined to the cell axis by the so called microfibril angle (MFA). The cellulose fibrils themselves contain crystalline parts, sized 30-40 nm in length and 3-4 nm im thickness (Andersson et al., 2003; Leppänen et al., 2009), which are surrounded by amouphous cellulose. The hemicelluloses are partly associated with

cellulose (glucomannan), forming so called cellulose aggregates, and partly associated with lignin (glucuronoxylan) (Reis et al., 1994; Stevanic and Salmén, 2009). Due to the parallel arrangement of the stiff cellulose fibrils, the mechanical properties of the S2 layer can be assumed to be transverse isotropic. The middle lamella is a lignified pectic layer connecting individual cells (Hafren et al., 2000; Terashima et al., 2012), which is usually very thin ($< 0.5 \mu\text{m}$) but gets thicker towards the cell corner regions. As the cell wall polymers in the ML show no preferential orientation in space, the ML can be assumed to be isotropic.

Wood-Water Interactions

In moist conditions water is incorporated into the whole wood cell wall. The amount of water in the wood cell walls is related to the environmental conditions, i.e. the relative humidity (RH) and temperature. Upon changes of these conditions, wood adsorbs and desorbs water from completely dry stages up to the so called fiber saturation point (FSP), where the cell wall is fully water saturated. The relation between the respective RH, temperature and the wood moisture content (MC) is described by so called sorption isotherms (Kollmann, 1982; Skaar, 1988; Englund et al., 2013).

The mechanical resistance of wood is reduced upon increasing MC, and this issue – together with the concurrent dimensional changes – represents a main barrier against more intensive use of wood in engineering constructions. Next to the loss of mechanical resistance by moisture itself, wood is also at higher risk to be affected by biodegradation by microorganisms such as fungi at higher MC, which will be addressed in the next section.

Wood-moisture relationships have been studied mainly experimentally on the macroscopic scale for a long time. The effect of MC on the stiffness and strength of wood has been determined for different types of wood and for different directions with respect to the fiber grain (e.g. see the review by Gerhards (1982)). The large variability of the microstructural parameters determining the mechanical properties of wood makes it difficult to extract common moisture-related trends for different wood species. Stepping down the hierarchical organization of wood to the cell wall scale enables to rule out density related effects as well as effects of other microstructural characteristics, like e.g. vessels or rays, and identify trends of cell wall properties with changing moisture contents. Investigations on moisture dependent cell wall properties have been conducted on single fibers (Kersavage, 1973; Ehrnrooth and Kolseth, 1984) and directly on the cell wall material (Yu et al., 2011). Extending these approaches to testing different hard- and softwood species, differing in composition and microstructural arrangement of their cell walls, enables to clarify the mechanisms of the mechanical softening of wood with increasing MC, and the role of the different cell wall polymers in the softening process.

Wood Variability

The aforementioned microstructural parameters, e.g. the mass density or the MFA, are not constants, but show great variability. This variability is expressed in (1) differences between wood species, e.g. hardwood and softwood, (2) differences within wood of the same tree species, e.g. caused by climatic conditions on site or fertilization, and (3) differences within single trees. This within-tree variability of wood properties is made up of distinct variability patterns and some random variation on top of these trends, which trends can be observed on different levels of hierarchy. On the clearwood level, pith-to-bark trends as well as base-to-apex trends of mass density or MFA are well known, e.g. increasing mass density and decreasing MFA from pith to bark (Lichtenegger et al., 1999; Donaldson, 2008; Zhang et al., 2007; Zhou et al., 2012; Yin et al., 2011b). One length scale below, distinct patterns of e.g. cell geometry and MFA can be identified within single annual rings, i.e. from EW to LW (Eder et al., 2009). Microstructural variations can even be found within single wood cells (Sarén et al., 2001; Anagnost et al., 2002; Sedighi-Gilani et al., 2006). These variability patterns of microstructural characteristics have also been identified for the mechanical properties of wood (Bendtsen and Senft, 1986; Koponen et al., 2005; Groom et al., 2002; Cramer et al., 2005; Yin et al., 2011b).

Both the effects of silvicultural measures on mass density and MFA (Yang and Evans, 2003; Auty, 2011; Gardiner et al., 2011) as well as for the effect of varying mass density and MFA on the mechanical properties of wood have been predicted using stochastic approaches (Evans, 1999; Evans and Ilic, 2001; Downes et al., 2002; Hein, 2010). However, each microstructural parameter calls for its own statistical model. Furthermore each model is restricted to the specific wood species, it has been developed and validated for. This limits the applicability of such models and calls for a deterministic approach. While the effects of silviculture on the wood microstructure cannot be described in sufficient detail, necessary to establish causal relationships, deterministic links between wood microstructure and the mechanical properties of wood have been established by means of micromechanical modeling (Salmén and de Ruvo, 1985; Astley et al., 1997; Hofstetter et al., 2005; Qing and Mishnaevsky, 2009). Using varying microstructural data at different hierarchical levels as model input, these micromechanical modeling approaches enable to study their influence on the mechanical properties of wood and their respective variability at different length scales.

Biodegradation of Wood

In natural ecosystems there is an equilibrium between continuous buildup and breakdown of woody biomass. Next to some animals, e.g. termites, marine borers, or woodpeckers, microorganisms, such as fungi and bacteria, play a major role in the decomposition of wood. Among these microorganisms decay fungi are the most efficient ones. According to their degradation strategy, they can be categorized into three main types: brown rot, white rot and soft rot fungi (Schwarze, 2007; Schmidt, 2006). While soft

rot decay occurs only in damp conditions, brown rot and white rot decay are of great importance for indoor and outdoor timber constructions. White rot fungi are able to degrade all wood polymers and can be further categorized into selective white rot fungi, which first cleave lignin to get access to the polysaccharides and then utilize them for nutrition, and simultaneous white rot fungi, degrading all wood polymers simultaneously (Blanchette, 1984; Fackler et al., 2011). Brown rot fungi are evolutionary more advanced (Eastwood et al., 2011) and are able to directly utilize the wood polysaccharides for nutrition, leaving behind a modified lignin (Goodell, 2003; Yelle et al., 2011; Arantes et al., 2012).

Due to the fact that the mechanical properties of wood within a tree cross section are highest in the outermost regions of the cross section which shows a high mass density and a low MFA (i.e. mature wood), structural members for timber constructions are preferably cut from these regions. However, the outermost region of a tree stem contains the sapwood, being more vulnerable to biodegradation than the inner heartwood (Taylor et al., 2002). Thus research on the natural durability of sapwood as well as attempts to improve the durability have been subject of numerous studies before (Wilcox, 1978; Winandy and Morrell, 1993; Curling et al., 2001; Bader et al., 2012a,b).

Biodegradation by fungi affects the composition and microstructure of wood. The most striking degradation effect – which is also the easiest effect to assess – is a distinct loss of mass and mass density (Curling et al., 2002; Bader et al., 2012b). Thus, in consequence, the mechanical properties of wood are altered as well (Wilcox, 1978; Winandy and Morrell, 1993; Curling et al., 2002; Bader et al., 2012a). On the macroscopic scale, i.e. for clear wood, stiffness and strength losses were observed and mainly explained as a consequence of the well known relations between mass density and stiffness/strength for wood (Bodig and Jayne, 1982; Kollmann, 1982; Eberhardsteiner, 2002). However, the underlying degradation mechanisms and their effects on the mechanical properties at the cell wall scale are masked by the effects of mass loss and cannot be assessed by means of macroscopic experiments. Investigations on the cell wall scale promise to deliver deeper understanding of the involved decay mechanisms.

Micromechanics of Wood

The mechanical properties of wood are determined by the hierarchical microstructure described above (Niklas, 1992; Salmén, 2004; Salmén and Burgert, 2009). These so called structure-function relationships need to be investigated in order to deepen the current insight into the relationships between wood microstructure and composition on the one hand and the mechanical properties at different length scales on the other hand.

In good approximation the macroscopic mechanical properties of wood can be described to be orthotropic (Bodig and Jayne, 1982; Eberhardsteiner, 2002). The material axes are oriented in a cylindrical coordinate system along the tree stem, i.e. longitudinal direction (L), and the annual rings, i.e. radial (R) and tangential direction (T). The me-

chanical properties of wood can be assessed by means of experiments but also by means of material modeling.

The variability of mechanical properties of wood, originating in the variability of the wood microstructure, has been investigated mainly experimentally (Bendtsen and Senft, 1986; Koponen et al., 2005; Groom et al., 2002; Cramer et al., 2005; Zhou et al., 2012) by the aforementioned methods at different length scales, i.e. from single cells to whole tree cross sections.

Accounting for the hierarchical structure of wood, experiments can be performed at different levels of the hierarchical structure. Starting at the macroscopic scale, where experimental test methods are nowadays described by standards (ASTM D4761, 2013; EN 408, 2012), experiments have been performed also on EW and LW slices (Cramer et al., 2005) and single wood fibers (Page et al., 1971; Burgert et al., 2002). Given that the fiber cross section is known (or measurable), the overall mechanical properties of the cell walls from single cells can be assessed (Burgert et al., 2005a; Eder et al., 2009). Extracting mechanical properties from the uniaxial stress state, resulting from such tests, can be done in a straight forward manner. However, extracting single fibers from a piece of wood is elaborate (Burgert et al., 2002) and the fibers are prone to twisting during drying (Groom et al., 2002; Burgert et al., 2005b).

The direct assessment of mechanical properties of wood at the cell wall scale has been attempted by a variety of methods (Eder et al., 2013; Burgert and Keplinger, 2013). These include micro-compression tests (Zhang et al., 2010) and nanoindentation (Wimmer et al., 1997; Wimmer and Lucas, 1997; Gindl et al., 2004; Tze et al., 2007; Konnerth et al., 2009; Zhang et al., 2012). The disadvantage of relating a compressive three-dimensional stress state underneath the indenter tip to the mechanical properties during nanoindentation – in contrast to the again rather simple uniaxial stress state during micro-compression tests – is compensated by a far less elaborate sample preparation procedure (microcompression test specimens prepared from wood cell walls have to be cut into shape using a focussed ion beam (FIB) under vacuum). Thus nanoindentation has become popular for investigations at the cell wall scale.

Material modeling approaches take advantage of the composite-like arrangement in of the wood microstructure in all levels of hierarchy (Cave, 1968; Salmén and de Ruvo, 1985; Astley et al., 1998; Harrington et al., 1998; Shishkina et al., 2014). Therefore analysis methods, well established in composite engineering, e.g. mean field methods (Hashin, 1983), finite element methods (Zienkiewicz and Taylor, 2000) or laminate theory (El Omri et al., 2000), can be applied.

In the following the two main methods regarding the assessment of mechanical properties of wood cell walls which were used herein are addressed in more detail, namely the fundamentals of continuum micromechanical modeling and nanoindentation.

Nanoindentation of Wood Cell Walls

Nanoindentation has indeed become the method of choice for investigations on the micro- and nanometer scale. While pushing a tip of defined geometry into a flat sample surface, the applied load and the resulting penetration depth are simultaneously recorded. Material properties, namely the indentation modulus M and the indentation hardness H , are derived from the resulting load-penetration depth curve (see Figure 2), following the approach by Oliver and Pharr (1992, 2004):

$$M = \frac{\sqrt{\pi}}{2} \frac{S}{\sqrt{A_C}}, \quad (1)$$

$$H = \frac{P_{max}}{A_C}. \quad (2)$$

where S is the initial unloading stiffness, P_{max} is the ultimate load (see Figure 2) and A_C denotes the contact area. The latter is calculated from the contact depth h_C by the so called tip-area function, which – for the perfect Berkovich indenter – reads as:

$$A_C = 24.5h_C^2, \quad (3)$$

and h_C is defined by:

$$h_C = h_{max} - \epsilon \frac{P_{max}}{S}, \quad (4)$$

where h_{max} is the maximum penetration depth and ϵ is 0.75 for a Berkovich type tip geometry.

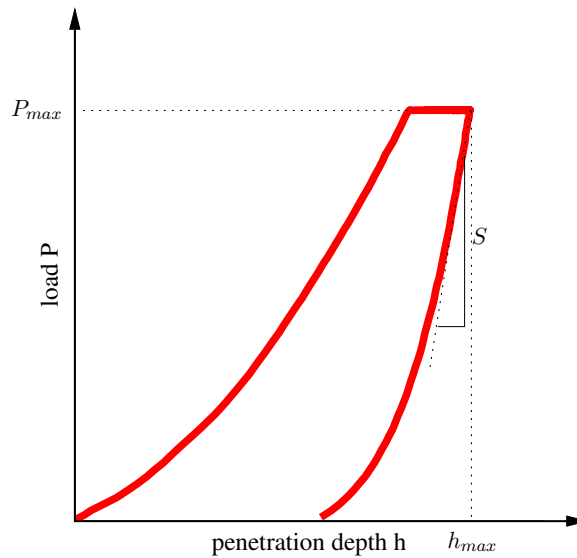


Figure 2: Load-displacement curve of a nanoindentation test, P_{max} denotes the maximum load, h_{max} denotes the maximum penetration depth

This analysis approach implies several – idealized – premises, including the penetration of the indenter tip into an isotropic homogeneous half-space and the assumption of plastic behaviour in the material underneath the indenter tip, leading to either pile-up or sink-in behaviour of the surrounding material during indentation. The indentation modulus M of an isotropic material can be related to its elastic material constants, like Young's moduli and the Poisson's ratios, in a very straight forward manner by:

$$\frac{1}{M} = \frac{1 - \nu^2}{E} + \frac{1 - \nu_i^2}{E_i}, \quad (5)$$

where E & ν and E_i & ν_i are Young's moduli and Poisson's ratios of the tested material and of the indenter, respectively (Oliver and Pharr, 1992).

However, in most applications at least one of these premises is not fulfilled, if natural materials – like wood or bone – are investigated (Zysset, 2009; Jakes et al., 2009). While effects of nearby interfaces or edges may be neglected if sufficiently far away from the indent (Jakes et al., 2009), the anisotropic nature of natural material represents the main challenge for the interpretation of test results. However, Vlassak et al. (2003) presented a further developed approach, based on the work of Swadener and Pharr (2001), accounting for the elastic anisotropy of the indented material.

Nanoindentation was first applied to investigate the mechanical properties of wood cell walls by Wimmer et al. (1997), who reported M and H for the S2 cell wall layer as well as for the middle lamella in the cell corners (Wimmer et al., 1997; Wimmer and Lucas, 1997). Since then, nanoindentation of wood cell walls have been conducted by many authors, but no quantitative link between M and the anisotropic material properties of the S2 cell wall layer was established, until Jäger et al. (2011a,b) applied the approach by Vlassak et al. (2003) to study wood cell walls. They presented approaches to determine the elastic constants of a transversely isotropic material experimentally by indenting the S2 cell wall layer in different directions (Jäger et al., 2011b) and to calculate M from known or predicted elastic constants of the transversely isotropic S2 cell wall layer material (Jäger et al., 2011a). The latter approach will be used herein, using the material properties of the S2 layer, predicted by micromechanical modeling. This enables to compare predicted indentation moduli M_{PRED} to experimentally determined indentation moduli M_{EXP} . Although the ML is assumed to be isotropic, and the Young's modulus could be calculated from M , for reasons of consistency, M_{PRED} is also calculated from the predicted isotropic material properties of the ML and subsequently compared to the corresponding experimental results.

Due to the multi-layered nature of the wood cell wall, its cross section exhibits multiple interfaces, possibly inflicting edge effects (Figure 3) (Jakes et al., 2009). While the thickness of the S2 layer is usually sufficient to place indents there and extract reliable results, the ML can only be assessed in the cell corners, where its thickness often exceeds 1 μm (Wimmer and Lucas, 1997; Gindl et al., 2004).

Although nanoindentation has established itself as useful tool in wood science, possible effects of sample preparation on the determined mechanical properties are still a subject of ongoing discussion. Wood samples are commonly embedded into resins, in

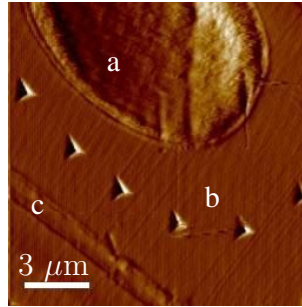


Figure 3: Scanning probe microscopy image of a cross section through an embedded wood cell wall; a...embedding material in the cell lumen, b...S2 layer, c...middle lamella; in the S2 layer the residual imprints after indentation can be seen

order to stabilize the cell walls during preparation and testing (Wimmer et al., 1997; Wimmer and Lucas, 1997; Gindl et al., 2004; Wang et al., 2006; Tze et al., 2007; Konnerth et al., 2009; Yin et al., 2011a). Attempts have been made to investigate the effects of embedding (Kim et al., 2012; Meng et al., 2013), with partly contradictory results. To clarify the effects of the embedding material on the measured cell wall properties, further investigations are needed.

Micromechanical Modeling

To overcome difficulties of experimental testing and to elucidate causal relationships between microstructure, composition and mechanical properties of wood, micromechanical modeling methods can be applied. Effective homogeneous material properties can be predicted from the information on the heterogeneous microstructure at a lower length scale (components and their respective dosages; shape, orientation and distribution of components; properties and interaction of components) by so called homogenization methods. Based on the microstructural information available, different methods lie at hand:

- **Representative volume element (RVE)** based methods, where the microstructure is described in a statistical manner by quasi-homogeneous subdomains, also referred to as material phases
- **Repetitive unit cell (RUC)** based methods, where the microstructural arrangement appears in a periodic manner and the microstructure itself can be discretized

In addition to homogenization methods, **Laminate theory** can be used to calculate effective properties if the observed microstructure appears as alternating layers of different materials.

Micromechanical models, representing the inherent hierarchical microstructure of wood, constitute from application of the aforementioned methods (Hofstetter and Gamstedt, 2009). Recent developments and extensions of a multiscale micromechanical

model for wood stiffness (Hofstetter et al., 2005, 2007; Bader et al., 2011b, 2012c; de Borst and Bader, 2014) form the basis of this thesis. This model uses RVE based homogenization methods (continuum micromechanics) for the cell wall material, RUC based homogenization methods (unit cell analysis) for the effective properties of EW and LW, and finally laminate theory for the effective properties of clearwood. As this work is mainly dedicated to cell wall properties, only the theoretical background of continuum micromechanics is addressed here in more detail (for a mathematical description of the unit cell approach and the laminate theory, see Appendix A in Hofstetter et al. (2007) and Appendix A in Bader et al. (2012c), respectively).

In continuum micromechanics, a material is understood as a micro heterogeneous body filling a RVE (Suquet, 1987; Zaoui, 2002) with characteristic length ℓ , $\ell \gg d$, d standing for the characteristic length of inhomogeneities within the RVE, and $\ell \ll \mathcal{L}$, \mathcal{L} standing for the characteristic lengths of geometry or loading of a structure built from the material defined in the RVE (separation of scales, Figure 4). The goal is to estimate the effective mechanical properties of the material defined on the RVE.

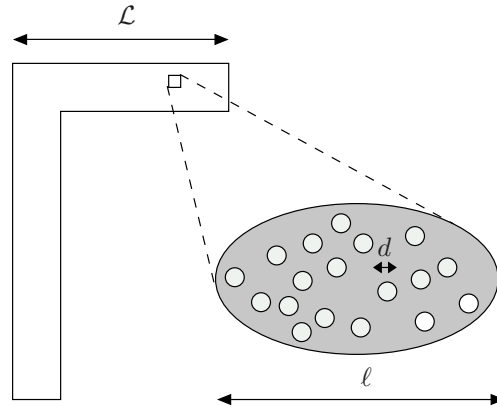


Figure 4: Separation of scales ($\mathcal{L} \gg \ell \gg d$)

For this purpose, homogeneous strains \mathbf{E} are prescribed at the boundary of the RVE, ∂V , in terms of displacements $\boldsymbol{\xi}(\mathbf{x})$ (Hashin, 1983)

$$\boldsymbol{\xi}(\mathbf{x}) = \mathbf{E} \cdot \mathbf{x}, \quad (6)$$

with \mathbf{x} as the position vector within the RVE (Figure 5).

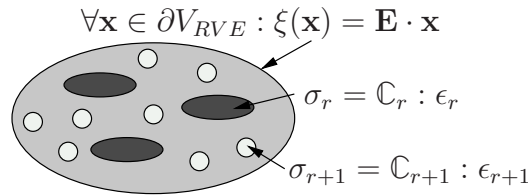


Figure 5: Loading of a representative volume element (RVE), built up by phases r (phase stiffness \mathbb{C}_r): displacements $\boldsymbol{\xi}$, related to a (homogenized) constant strain \mathbf{E} , are imposed at the boundary of the RVE; reproduced from Hellmich et al. (2004)

As a consequence, the resulting kinematically compatible microstrain $\boldsymbol{\epsilon}(\mathbf{x})$ within the RVE can be averaged over the RVE (Hashin, 1983), giving the homogenized macroscopic strain \mathbf{E}

$$\mathbf{E} = \frac{1}{V_{RVE}} \int_{V_{RVE}} \boldsymbol{\epsilon}(\mathbf{x}) dV = \langle \boldsymbol{\epsilon} \rangle. \quad (7)$$

Given that the RVE can be described by (quasi)homogeneous subdomains, or phases, exhibiting the local constitutive behaviour

$$\boldsymbol{\sigma}_r = \mathbb{C}_r : \boldsymbol{\epsilon}_r, \quad (8)$$

Equation 7 can be rewritten as

$$\mathbf{E} = \sum_r \boldsymbol{\epsilon}_r f_r, \quad (9)$$

where f_i are the volume fractions of the single phases within the RVE. Similarly, for traction boundary conditions resulting in equilibrated microstresses $\boldsymbol{\sigma}(\mathbf{x})$ ($\text{div} \boldsymbol{\sigma}(\mathbf{x})=0$), homogeneous macroscopic stresses $\boldsymbol{\Sigma}$ are related to the microstress $\boldsymbol{\sigma}$ by volume averaging as well

$$\boldsymbol{\Sigma} = \frac{1}{V_{RVE}} \int_{V_{RVE}} \boldsymbol{\sigma}(\mathbf{x}) dV = \langle \boldsymbol{\sigma} \rangle, \quad (10)$$

or again for material phases

$$\boldsymbol{\Sigma} = \sum_r \boldsymbol{\sigma}_r f_r. \quad (11)$$

The global (macroscopic) constitutive behaviour of the whole RVE can be written as

$$\boldsymbol{\Sigma} = \mathbb{C}^{hom} : \mathbf{E}, \quad (12)$$

where the macroscopic stresses and strains $\boldsymbol{\Sigma}$ and \mathbf{E} are linked by the sought homogenized 4th order stiffness tensor \mathbb{C}^{hom} of the material filling the RVE. \mathbb{C}^{hom} needs to be linked to the stiffness of the individual phases \mathbb{C}_r . This link is established based on the concept of linking macroscopic strain \mathbf{E} to the average strain within each material phase $\boldsymbol{\epsilon}_r$ by

$$\boldsymbol{\epsilon}_r = \mathbb{A}_r : \mathbf{E}, \quad (13)$$

or, in analogy, linking macroscopic stresses $\boldsymbol{\Sigma}$ to stresses within each material phase $\boldsymbol{\sigma}_r$

$$\boldsymbol{\sigma}_r = \mathbb{B}_r : \boldsymbol{\Sigma}, \quad (14)$$

where \mathbb{A}_r and \mathbb{B}_r ($\langle \mathbb{A}_r \rangle = \mathbb{I}$, $\langle \mathbb{B}_r \rangle = \mathbb{I}$) are the 4th order strain and stress concentration tensors, respectively. Inserting Equation 13 in Equation 8 and applying stress averaging according to Equation 10 leads to

$$\boldsymbol{\Sigma} = \frac{1}{V_{RVE}} \int_{V_{RVE}} \mathbb{C}(\mathbf{x}) : \mathbb{A}(\mathbf{x}) dV : \mathbf{E}. \quad (15)$$

According to Equation 12, the sought \mathbb{C}^{hom} can be written as

$$\mathbb{C}^{hom} = \frac{1}{V_{RVE}} \int_{V_{RVE}} \mathbb{C}(\mathbf{x}) : \mathbb{A}(\mathbf{x}) dV, \quad (16)$$

or re-written for material phases

$$\mathbb{C}^{hom} = \sum_r f_r \mathbb{C}_r : \mathbb{A}_r. \quad (17)$$

To estimate \mathbb{C}^{hom} estimates for \mathbb{A}_r (or \mathbb{B}_r) have to be determined. A simple choice of $\mathbb{A}_r = \mathbb{I}$ or $\mathbb{B}_r = \mathbb{I}$ leads to the well known laws of mixtures according to Voigt (1889) and Reuss (1929). Other estimates have been derived from Eshelby's solution of the inhomogeneity problem (Eshelby, 1957). There an ellipsoidal inhomogeneity H with stiffness \mathbb{C}_H is embedded in an infinite homogeneous elastic matrix with stiffness \mathbb{C}^0 . If the matrix is subjected to a homogeneous strain \mathbf{E}^∞ at infinity, the strain field inside H is found to be uniform and given by

$$\boldsymbol{\epsilon}_H = [\mathbb{I} + \mathbb{P}_H^0 : (\mathbb{C}_H - \mathbb{C}^0)]^{-1} : \mathbf{E}^\infty, \quad (18)$$

with \mathbb{P}_H^0 as the 4th order Hill tensor, accounting for the shape of the inhomogeneity H and the elastic symmetry of the material (Eshelby, 1957; Laws, 1977; Zaoui, 2002). For spherically shaped inclusions and isotropic behavior of the matrix material, \mathbb{P}_{sph}^0 reads as (Hellmich et al., 2004; Bader et al., 2011b)

$$\mathbb{P}_{sph}^0 = \mathbb{S}^{Esh,0} : \mathbb{C}_0^{-1}, \quad (19)$$

$$\mathbb{S}^{Esh,0} = \alpha_0 \mathbb{J} + \beta_0 \mathbb{K}, \quad (20)$$

with

$$\alpha_0 = \frac{3k_0}{3k_0 + 4\mu_r}, \quad (21)$$

$$\beta_0 = \frac{6(k_0 + 2\mu_0)}{5(3k_0 + 4\mu_0)}, \quad (22)$$

where k_0 and μ_0 are the bulk and shear moduli of the matrix phase 0 with stiffness \mathbb{C}_0 ; $\mathbb{J} = 1/3 \mathbb{I} \otimes \mathbb{I}$ and $\mathbb{K} = \mathbb{I} - \mathbb{J}$ are the volumetric and deviatoric parts of the 4th order unity tensor \mathbb{I} with components $I_{ijkl} = 1/2(\delta_{ik}\delta_{jl} + \delta_{il}\delta_{jk})$. For cylindrically shaped inclusions and isotropic matrix behaviour, the non zero components of \mathbb{P}_{cyl}^0 read as (Hellmich et al., 2004; Bader et al., 2011b)

$$P_{cyl,1111}^0 = P_{cyl,2222}^0 = 1/8(5C_{1111}^0 - 3C_{1122}^0)/C_{1111}^0/\mathcal{D}, \quad (23)$$

$$P_{cyl,1122}^0 = P_{cyl,2211}^0 = -1/8(C_{1111}^0 - C_{1122}^0)/C_{1111}^0/\mathcal{D}, \quad (24)$$

$$P_{cyl,2323}^0 = 1/(8C_{2323}^0), \quad (25)$$

$$P_{cyl,1212}^0 = 1/8(3C_{1111}^0 - C_{1122}^0)/C_{1111}^0/\mathcal{D}, \quad (26)$$

where

$$\mathcal{D} = C_{1111}^0 - C_{1122}^0 \quad (27)$$

and

$$C_{2323}^0 = 1/2(C_{1111}^0 - C_{1122}^0). \quad (28)$$

Deriving estimates for the inclusion-based overall stiffness is done by estimating the average stresses and strains in each phase r of the RVE, subjected to macroscopic \mathbf{E} , as those of an ellipsoidal inclusion with stiffnesses \mathbb{C}_r , embedded in a matrix with arbitrary stiffness \mathbb{C}^0 , subjected to \mathbf{E}^∞ .

Re-writing Equation 18 for an ellipsoidal inclusion r , applying strain averaging and resolving for \mathbf{E}^∞ yields

$$\mathbf{E}^\infty = \left\{ \sum_r f_r [\mathbb{I} + \mathbb{P}_r^0 : (\mathbb{C}_r - \mathbb{C}^0)]^{-1} \right\}^{-1} : \mathbf{E}. \quad (29)$$

Inserting the constitutive relationship for the inclusion r (Equation 8) into Equation 29 yields

$$\boldsymbol{\sigma}_r = \mathbb{C}_r : [\mathbb{I} + \mathbb{P}_r^0 : (\mathbb{C}_r - \mathbb{C}^0)]^{-1} : \mathbf{E}^\infty. \quad (30)$$

Applying stress averaging to Equation 30 and inserting \mathbf{E}^∞ , according to Equation 29, a relation between macroscopic $\boldsymbol{\Sigma}$ and \mathbf{E} is found

$$\boldsymbol{\Sigma} = \sum_r f_r \mathbb{C}_r : [\mathbb{I} + \mathbb{P}_r^0 : (\mathbb{C}_r - \mathbb{C}_0)]^{-1} : \left\{ \sum_s f_s [\mathbb{I} + \mathbb{P}_s^0 : (\mathbb{C}_s - \mathbb{C}_0)]^{-1} \right\}^{-1} : \mathbf{E}. \quad (31)$$

\mathbb{A}_r then reads as

$$\mathbb{A}_r = [\mathbb{I} + \mathbb{P}_r^0 : (\mathbb{C}_r - \mathbb{C}_0)]^{-1} : \left\{ \sum_s f_s [\mathbb{I} + \mathbb{P}_s^0 : (\mathbb{C}_s - \mathbb{C}_0)]^{-1} \right\}^{-1}, \quad (32)$$

and finally

$$\mathbb{C}^{hom} = \sum_r f_r \mathbb{C}_r : [\mathbb{I} + \mathbb{P}_r^0 : (\mathbb{C}_r - \mathbb{C}_0)]^{-1} : \left\{ \sum_s f_s [\mathbb{I} + \mathbb{P}_s^0 : (\mathbb{C}_s - \mathbb{C}_0)]^{-1} \right\}^{-1}. \quad (33)$$

The expression for \mathbb{C}^{hom} contains all the necessary information about the microstructure within the considered RVE, i.e. the dosages of the individual phases as their respective volume fractions f_r , the stiffnesses of the individual phases \mathbb{C}_r , and their morphology and shape are accounted for within \mathbb{P}_r^0 . Depending on the interaction of the phases within the considered RVE, \mathbb{C}_0 can be chosen differently

- for a matrix-inclusion like arrangement: $\mathbb{C}_0 = \mathbb{C}_M \rightarrow$ Mori-Tanaka scheme (Mori and Tanaka, 1973; Benveniste, 1987))
- for a polycrystalline like arrangement: $\mathbb{C}_0 = \mathbb{C}^{hom} \rightarrow$ Self-Consistent scheme (Kröner, 1958; Zaoui, 2002))

If a subdomain or material phase exhibits a microstructural arrangement on a lower length scale itself, the homogenization scheme can be repeatedly applied, leading to multiscale homogenization scheme which can account for a hierarchically structured material (Figure 6).

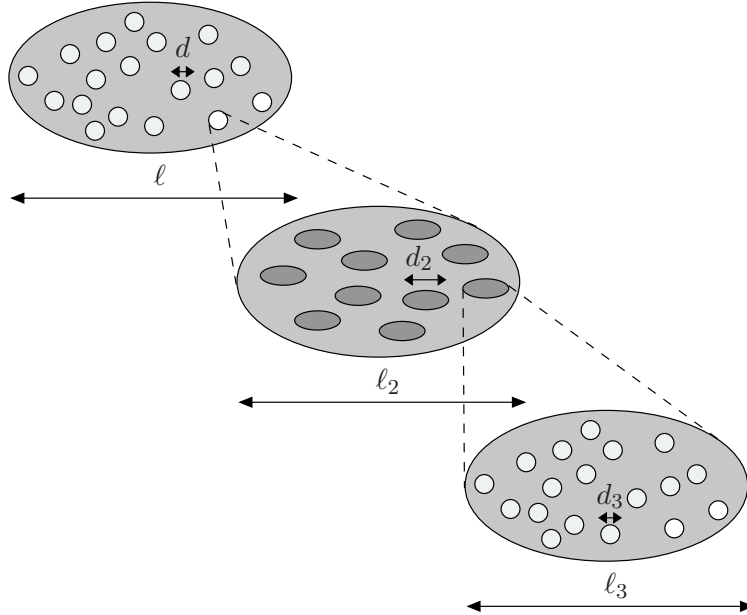


Figure 6: Multiscale homogenization scheme: the properties of the phases (characteristic lengths d , d_2 and d_3) inside the RVEs (characteristic lengths l , l_2 and l_3) are derived from homogenization over smaller RVEs (with characteristic lengths $l_2 \leq d$ and $l_3 \leq d_2$)

Research Objectives and Outline of the Thesis

The research objectives of this thesis are outlined in the following. They are addressed in terms of the objectives of the five publications, of which this thesis is composed.

Publication 1 is dedicated to clarifying how the measurement results from NI tests on wood cell walls may be affected by the way the sample is prepared and the indentation is carried out. Indentation data for different sample preparation techniques and indentation protocols are presented, and the observed differences of the obtained indentation moduli and hardnesses are critically evaluated. Investigations cover the effect of different embedding materials, including testing of non-embedded cell walls, and the effect of repeated exposure to high temperatures during harsh drying before the indentation test. Moreover, potential edge effects are studied for indentation sizes approaching the width of the tested cell wall layer.

Publication 2 deals with effect of water on the mechanical properties of wood cell walls. For this purpose, wood specimens from five different hardwood and softwood species (Norway spruce, Scots pine, Common yew, European oak and European beech) are investigated by means of nanoindentation. The tests are performed at RH ranging from 10% to 80% and in saturated conditions under water. Cell wall stiffness and creep properties of the S2 layer and the ML are tested. Dynamic vapour sorption is used to determine the sorption isotherms from very small amounts of material, close to the position where the samples for nanoindentation have been prepared from. The cross sections of the nanoindentation specimens, which are embedded in a resin, are checked for their ability to swell upon MC changes by means of environmental scanning electron microscopy. The respective stiffness changes and changes in the creep parameters are related to the changing MC during the tests, and the individual contributions of the cell wall polymers to the observed moisture-related effects are discussed.

In **Publication 3**, microstructure-stiffness relationships of Scots pine wood are examined with a focus on the effects of the microstructural variability on the elastic properties of wood at different length scales. For this purpose, microstructural data, acquired from SilviScan-3™ (namely wood density, cell dimensions, EW and LW proportion, microfibril angle) is augmented with local measurements of these quantities and of the chemical composition, derived from wide-angle X-ray scattering, light microscopy, and thermogravimetric analysis, respectively. The stiffness properties are determined experimentally by means of ultrasonic tests at the clear wood scale and by means of nanoindentation at the cell wall scale. In addition, micromechanical modeling is applied to assess the causal relations between structural and mechanical properties and to complement the experimental investigations. A detailed mathematical description of the applied multiscale micromechanical model, which is not included in the original publication, can be found in Appendix 1. Typical variability profiles of microstructural and mechanical properties are shown from pith to bark and across a single growth ring (from EW to LW). Furthermore, the effect of random variability, on top of the observed variability patterns, is discussed.

Publications 4 and **5** deal with the effects of fungal decay on the mechanical properties of softwood. At the macro-scale, the occurring losses of mass and of mass density mask effects of altered chemical composition and microstructure. Thus, it is necessary to step down the hierarchical organization of wood to the cell wall scale in order to resolve these changes and their mechanical impact, as detailed for each publication in the following.

Publication 4 is dedicated to the experimental assessment of fungal decay of softwood cell walls. Fungal decay results in alterations of their composition, microstructure and mechanical properties. It is still unclear whether the structure function relationships of wood cell walls, which are started to be understood in sound condition, also hold for deteriorated wood cell walls. To investigate these relationships, selected annual rings of fungal degraded Scots pine sapwood are analyzed for their composition, microstructure and micromechanical properties by means of X-ray scattering, nanoindentation, attenuated total reflectance Fourier transform infrared spectroscopy and wet chemical methods. The dataset is acquired in the middle lamella and, separately for EW and LW, in the S2 cell wall layer. Multivariate data analysis is applied to identify relationships in the big dataset. Using principle component analysis and partial least squares regression analyses, links between changes of the mechanical properties of wood cell walls (stiffness and hardness) and altered cell wall composition and microstructure are established.

In **Publication 5** the previously established links between composition, microstructure and mechanical properties of the S2 layer and the middle lamella are further investigated. Applying a multiscale micromechanical model for wood cell wall stiffness and using the results of the chemical and microstructural characterization of the fungal degraded softwood cell walls as input, enables to rise these links from a statistical to a physical level, and therefore to identify causal relationships between composition, microstructure and mechanical properties of the S2 layer and the ML. In addition the model allows to test hypotheses on yet unknown effects of fungal decay. The latter include the evolution of porosity, modifications of the cell wall polymers resulting in changes of their stiffnesses, as well as increasing cell wall crystallinity. A detailed mathematical description of the applied multiscale micromechanical model, which is not included in the original publication, can be found in Appendix 4.

Contribution of the Author

This thesis is a cumulative work consisting of five publications in peer-reviewed scientific journals. The author's contributions to the respective publications are as follows:

- **Publication 1:** *Nanoindentation of wood cell walls: effects of sample preparation and indentation protocol (Wagner et al., 2014a)*: The author proposed the investigated modified procedures and sample pretreatments, performed all mechanical tests and statistical data analysis and prepared most of the manuscript.
- **Publication 2:** *Effect of water on the mechanical properties of wood cell walls – results of a nanoindentation study (Wagner et al., 2014d)*: The author performed a part of the mechanical tests, all data analysis and prepared a part of the manuscript.
- **Publication 3:** *Key parameters controlling stiffness variability within trees: a multiscale experimental-numerical approach (Wagner et al., 2013)*: The author performed all microstructural and compositional characterization, all mechanical tests, developed a micromechanical model for calculating stiffness predictions, and prepared most of the manuscript.
- **Publication 4:** *A combined view on composition, molecular structure and micromechanics of fungal degraded softwood (Wagner et al., 2014c)*: The author proposed the concept of the experimental outline, performed all mechanical tests as well as the microstructural characterization and prepared a major part of the manuscript.
- **Publication 5:** *Fungal degradation of softwood cell walls: enhanced insight through micromechanical modeling (Wagner et al., 2014b)*: The author formulated the decay-related hypotheses, performed all micromechanical model calculations to test those hypotheses and prepared most of the manuscript.

Nanoindentation of Wood Cell Walls: Effects of Sample Preparation and Indentation Protocol (Wagner et al., 2014a)

Authored by Leopold Wagner, Thomas K. Bader and Karin de Borst

Published in *Journal of Materials Science*, 49(1):94–102, 2014

Nanoindentation has become a valuable tool in wood science. It enables to examine the mechanical properties of the wood cell walls, which are polymeric, multi-layered structures with typical thicknesses of a few micrometers. Despite the intensive use of the method for the characterization of wood cell walls, it is not entirely clear yet how the measurement results may be affected by the way the sample is prepared and the indentation is carried out. This manuscript contributes to clarifying these issues, by presenting indentation data for a variety of sample preparation techniques and indentation protocols, and by critically evaluating the observed differences of the obtained indentation moduli and hardnesses. Investigations covered the effect of different embedding materials, including testing of nonembedded cell walls, and of repeated exposure to high temperatures during harsh drying before the indentation test. Moreover, potential edge effects were studied when the indentation size approaches the width of the individual cell wall layers. Using different embedding materials as well as testing non-embedded cell walls did not lead to significant changes in the measured properties. Due to damage during the sample preparation, nonembedded cell walls tend to show substantially higher experimental scatter. Repeated drying prior to embedding had no significant effect on the resulting moduli and hardnesses. Finally, it was found that reasonable me-

chanical properties can be extracted from the cell corner middle lamella (CCML), even when the size of the indent approaches the diameter of the CCML.

1.1 Introduction

Over the last decades, nanoindentation, also referred to as instrumented indentation or depth sensing indentation, has become the method of choice when investigating mechanical properties of materials at the micro and nanometer scale. While pushing a tip with a specific geometry into a sample with a flat surface, load and penetration depth are recorded simultaneously. The derivation of material properties, such as the indentation modulus or reduced modulus M and the hardness H , from the resulting load displacement curves generally follows the procedure proposed by Oliver and Pharr (1992, 2004). Over the last fifteen years, nanoindentation has also established itself as a useful tool in wood science for assessing the mechanical properties of native (Wimmer and Lucas, 1997; Wimmer et al., 1997; Gindl et al., 2002; Konnerth et al., 2009; Eder et al., 2013; Wagner et al., 2013) and also modified wood cell walls (Gindl and Gupta, 2002; Konnerth et al., 2010; Yin et al., 2011a). The wood cell wall shows a layered structure. It contains the primary cell wall and three secondary cell wall layers (S1, S2, and S3), which differ in microstructure and, consequently, mechanical properties. The S2 layer is the by far thickest and, thus, mainly responsible for the mechanical stiffness and strength of wood (Salmén and Burgert, 2009). Individual wood cells are connected by the middle lamella.

Despite the intensive use of the method for the characterization of wood cell walls, it is not entirely clear yet how the measurement results may be affected by the way the sample is prepared and the indentation is carried out. This manuscript contributes to clarifying these issues, by presenting indentation data for a variety of sample preparation techniques and indentation protocols, and by critically evaluating the observed differences of the obtained indentation moduli and hardnesses.

Wood samples are commonly embedded into resin in order to stabilize the cell walls during the microtome cutting and the indentation (Wimmer et al., 1997; Wimmer and Lucas, 1997; Gindl and Gupta, 2002; Gindl et al., 2002; Tze et al., 2007; Konnerth et al., 2009, 2010; Yin et al., 2011a; Eder et al., 2013; Wagner et al., 2013). These epoxy resins fill all accessible lumina. It has been proposed that their access to the cell wall ultrastructure is limited (Kamke and Lee, 2007; Konnerth et al., 2008), but it remains uncertain if and to which extent the resin may penetrate the cell walls. Related potential effects of the resin on mechanical properties are difficult to identify due to the generally large experimental scatter.

In general, only few studies have dealt with the influence of embedding material on nanoindentation test results (Kim et al., 2012; Meng et al., 2013). Thereby, alternative sample preparation techniques are used that allow testing (apparently) non-embedded cell walls not affected by potential resin penetration. This provides reference values to which the results obtained in embedded samples can be compared to. The approaches

used include limiting epoxy resin penetration into the cell lumina by pre-curing, which increases the viscosity of the epoxy resin (Kim et al., 2012), or encapsulating the wood specimen in a foil prior to embedding (Meng et al., 2013). While Kim et al. (2012) found no significant effects of the embedding, Meng et al. (2013) reported significantly higher values for embedded wood cell walls. These studies used material with different microstructural characteristics, such as microfibril angle (MFA), which might have contributed to these contradictory results. Also, attempts to test without any embedment have been carried out (Jakes et al., 2008). However, all mentioned strategies prevent penetration of any resin in the cell walls comes at the expense of a less stabilized cell wall during microtome cutting. Therefore the testing surface might be less smooth, and not every tracheid cross section might be suitable for indentation. This might again spoil the indentation results. We herein analyze the influence of the sample preparation method by comparing test results for samples embedded into different embedding materials and also for apparently not embedded cell walls.

In addition, the exposure of samples to heat during the embedment process may affect the material's response in the indentation test. This can happen either prior to the indentation testing – for example when determining the oven-dry mass – or during the sample preparation when curing the resin used for embedding. Typical curing temperatures of embedding resins can go up to 60°C or 70°C. Although the glass transition (GT) temperatures of the wood polymers lignin and hemicellulose are reported to be well above 100°C in the dry state (Back and Salmén, 1982; Irvine, 1984), they are known to decrease with increasing moisture content to just below 100°C for lignin and to around 0°C for hemicelluloses in the green state (Olsson and Salmén, 1997). During heating of wood, not only effects of the GT may induce changes of the micromechanical properties measured by NI, but also the formation of cracks, both macroscopic and microscopic. In the following, we present test results obtained on samples having undergone different numbers of wetting/harsh oven-drying cycles, in order to identify potential effects of heating. Moreover, we investigate if the intensity of drying may result in variations of the material properties across a small sized clear wood sample, typically used for oven-drying, i.e. that regions close to the surface may be more strongly affected by the heating than regions in the interior of the sample.

Finally, the size of the indent in relation to the dimensions of the investigated patch of material may influence the indentation stiffness and hardness. In particular, the effect of interfaces to pores or other materials close to the indent could be substantial. Such effects are commonly denoted as 'edge effects'. Based on comprehensive experimental investigations, Jakes et al. (2008) stated minimum distances from the center of the remaining imprint of an indent in the S2 cell wall layer to the nearest interface, which is either to the cell lumen or to the middle lamella. This distance depends on the experimental setup, i.e. the tipshape, on the load level, and on the tested material. The middle lamella between two adjacent cell walls is usually too narrow to keep this required distance. Sometimes, placing indents in the cell corners can circumvent this problem (Wimmer and Lucas, 1997; Gindl et al., 2004), but also the extension of the cell corner middle lamella (CCML) might be too small. We herein investigate whether

reasonable results in the CCML can also be acquired when the minimum distance is not fulfilled. We increase the extension of the contact area of the indenter tip with increasing penetration depth during indentation, until it is even exceeding the width of the CCML.

1.2 Materials and Methods

1.2.1 Samples

A Norway spruce (*Picea abies* [L.] Karst.) tree was crosscut at the sawmill immediately after harvesting. The boards were gently dried to a moisture content of approximately 12%. Afterwards, they were stored in a climatized room at 20°C and 60±5% relative humidity (RH). A rod of 15x2x2 cm³, in longitudinal, radial, and tangential direction (LxRxT), was cut from a clear wood section within one board (Figure 1.1a). Only material from the same annual ring, i.e. with clear wood of the same cambial age, was used in this study. The samples were shifted in longitudinal direction, but were all taken at the same position in R and T direction. Consequently, low microstructural variability, particularly low variability in microfibril angle (MFA) can be assumed. The rod was cut into five consecutive cubes sized 2x2x2 cm³ (LxRxT) (Figure 1.1b). The mass of each sample at 20°C and 60% RH was determined. The sample REF was excluded from any further treatment and served as reference for investigations of the influences of drying (D) and embedding (E) and of edge effects (see Table 1.1).

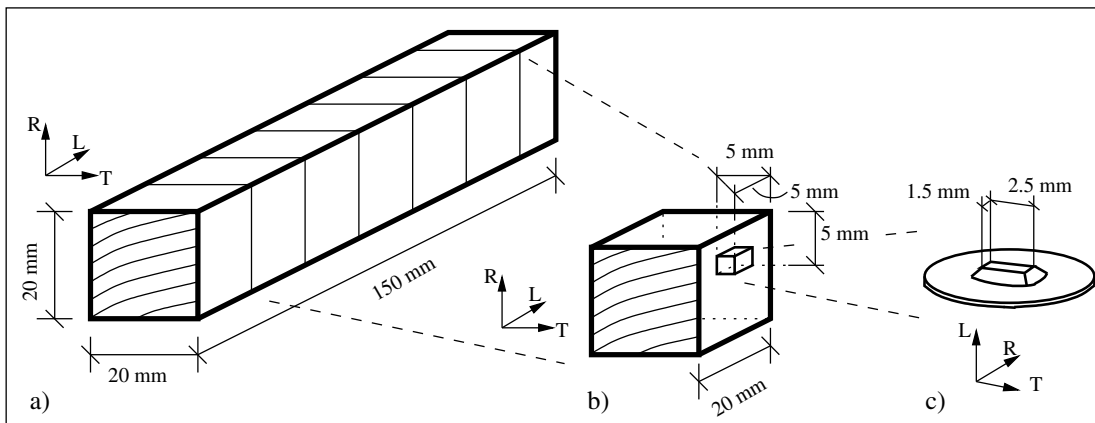


Figure 1.1: Sampling procedure: a) initial rod; b) five consecutive cubical samples (REF to D4) used for drying tests; c) NI-specimen

1.2.2 Drying of Wood Samples

The 2x2x2 cm³ cubes were water saturated under vacuum conditions for 48 h and then placed in a pre-heated muffle furnace at 103±2°C until consecutive weighing after 2 h intervals revealed differences in mass <0.01% (for masses <100 g; see EN 13183-1 (2002)). This procedure was repeated up to four times. The oven dry mass of each

Table 1.1: Overview of sample preparation methods and specimen labels (*italic*) for the different test series

Standard Procedure	
Sample: <i>REF</i>	
<ul style="list-style-type: none"> • Agar Low Viscosity Resin Kit (A-LV) • 30 min vacuum • cured at 60°C 	
Modified Procedures	
“Drying Tests”	“Embedding Tests”
Samples: <i>D1–D4, D4s</i>	Samples: <i>E1 & E2</i>
<ul style="list-style-type: none"> • A-LV • 30 min vacuum • cured at 60°C 	<ul style="list-style-type: none"> • A-LV • no vacuum • cured at 60°C ⇒ <i>E1</i>
Drying/wetting cycles	
<ul style="list-style-type: none"> • 1 × ⇒ <i>D1</i> • 2 × ⇒ <i>D2</i> • 3 × ⇒ <i>D3</i> • 4 × ⇒ <i>D4, D4s</i> 	<ul style="list-style-type: none"> • Struers EpoFix (S-EF) • 30 min vacuum • cured at room temp. ⇒ <i>E2</i>

sample was determined after every cycle. Then, one sample was removed from the set each time. This resulted in a series of four samples (D1 to D4), having undergone one (D1) to four cycles (D4) of water saturation and drying, in addition to the untreated reference sample (REF, Figure 1.2). All samples were stored in a climate chamber after oven drying at 20°C and 60% RH.

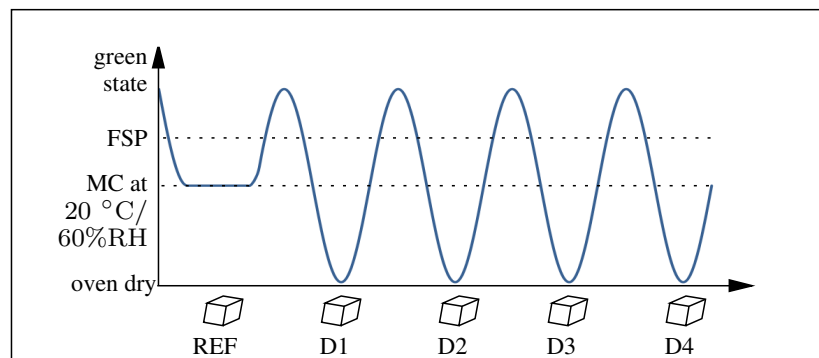


Figure 1.2: Drying-wetting cycles and the corresponding time series of the samples REF to D4

1.2.3 Embedment and Preparation of NI-Specimens

Specimens for NI were prepared according to a standard procedure, which was then partly modified to investigate the aforementioned effects. An overview of the differ-

ent sample preparation procedures, as well as of all prepared NI-specimens is given in Table 1.1.

Standard Procedure

Small specimens of approximately $2 \times 2.5 \times 1.5 \text{ mm}^3$ (LxRxT) were cut, originating from the same annual ring in each sample. The average microfibril angle (MFA) in the late-wood of that specific ring was $12.5 \pm 4.5^\circ$, measured from dried and stained thin sections according to Senft and Bendtsen (1985). The location of the NI-specimens was approximately 5 mm beneath the original surfaces (see Figure 1.1c). The small wood specimens were then embedded in an epoxy resin (AGAR Low Viscosity Resin Kit, *Agar Scientific*, Essex, UK) and exposed to vacuum for 30 minutes. Afterwards the embedded specimens were cured at 60°C for approximately 24 hours. The exact orientation of the axes of the cells in the embedded small wood specimens was determined after the curing by visual inspection under the microscope. A microtome (Leica Ultracut, *Leica Microsystems*, Wetzlar, GER), equipped with a diamond knife, was used to cut smooth the plane surface. The knife was positioned perpendicular to the respective wood cell orientation for this purpose (for further details see e.g. Konnerth et al. (2008) or Wagner et al. (2013)). Specimens were cut in R-direction, taking advantage of the rather straight alignment of the softwood cell walls in this direction. One NI-specimen (REF) was prepared according to this standard procedure, serving as reference for all subsequent modified procedures.

Modified Procedures

For investigating the effects of (repeated) drying and of edge effects in the CCML, material of the $2 \times 2 \times 2 \text{ cm}^3$ cubes that had undergone the repeated wetting/drying cycles was used. The cutting and embedment of the samples followed the standard procedure as described in subsection Standard Procedure ("Drying Tests" in Table 1.1). To investigate a potential depth effect of the drying, one additional NI-specimen (D4s) was cut from the same annual ring directly from the surface of the original sample D4 (rather than from 5 mm beneath the surface). Therefore it contained material that had been exposed to higher gradients of temperature and moisture content (MC) during oven-drying. To determine possible effects of the embedding procedure, two additional specimens (E1 & E2) were prepared from the untreated reference material ("Embedding Tests", Table 1.1). Their embedding procedure was slightly modified compared to the standard procedure outlined in subsection Standard Procedure. One NI-specimen (E1) was embedded in the standard resin (AGAR Low Viscosity Resin Kit), but not subjected to vacuum treatment. This results in limited resin penetration into the cell lumina and in a substantial number of apparently non-embedded tracheids in the center of the specimen. Non-embedded cells were identified by visual inspection under the light microscope. The second NI-specimen (E2) was embedded in a different embedding resin (Struers EpoFix, *Struers A/S*, Ballerup, DEN), which is cured without heating at room temperature for approximately 20 hours. All other preparation steps (i.e. vacuum treatment, cutting, ...) were performed as described in the standard procedure.

1.2.4 Nanoindentation Tests

The nanoindentation tests were performed using a TriboIndenter[®] (*Hysitron Inc.*, Minneapolis, MN, USA), equipped with a three-sided pyramid-shaped tip (Berkovich type) in load controlled mode. Climatic conditions inside the indenter chamber were kept constant at 20°C and 60% RH during the tests, using a RH-200 Relative Humidity Generator (*L&C Science and Technology*, Hialeah, FL, USA). All samples were stored in the acclimatized chamber at least 24 hours before the actual tests, resulting in an average MC of 11% in the NI-specimens. Respective positioning of the indents in the S2 cell wall layer or the CCML was verified using the built-in scanning probe microscope (SPM). A step-wise load function was applied which consists of three consecutive loading, holding and partial unloading steps following the protocol of Tze et al. (2007) for a continuous stiffness and hardness measurement. The maximum load amounted to 250 μN . The resulting imprints were inspected via the SPM. All load-indentation depth curves were evaluated according to the Oliver and Pharr method (Oliver and Pharr, 1992). The slope of the initial unloading path S is related to the elastic material properties, namely to the indentation modulus M , by

$$M = \frac{\sqrt{\pi}S}{2\sqrt{A_C}} \quad (1.1)$$

with A_C as the contact area. Division of the maximum load P_{max} by the contact area yields the indentation hardness H

$$H = \frac{P_{max}}{A_C}. \quad (1.2)$$

For studying the effects of the drying procedures, 25 indents were placed both in the S2 layer of tangential cell walls of latewood (LW) tracheids near the annual ring border ($N_{D,S2}=5 \times 25$) and in the CCML between these LW tracheids ($N_{D,CCML}=5 \times 25$), for each NI-specimen (REF, D1 to D4). The effect of different embedding procedures was only investigated for the S2 layer. Again, 25 indents were placed in tangential cell walls of LW tracheids near the annual ring border ($N_{E,S2}=2 \times 25$) for the two NI-specimens prepared in different manner (E1 & E2). Tangential cell walls were indented rather than radial ones, since local MFA nonuniformities around bordered pits in the radial cell walls (Sedighi-Gilani et al., 2006) would increase the variability of M due to the dependence of M on the MFA (Jäger et al., 2011a). In the CCML, edge effects on M and H were studied. Since the severity of these effects strongly depends on the indentation depth and, thus, the indenter load, a different load function was applied here, consisting of seven-steps and reaching a final maximum load P_{max} of 5000 μN (see Figure 1.3, left). Twelve indents were placed in CCMLs between LW tracheids on the reference NI-specimen REF ($N_{DE,CCML}=12$).

1.3 Results and Discussion

1.3.1 Edge Effects in the Cell Corner Middle Lamella (CCML)

The indentation modulus M and hardness H of the CCML at different loads were plotted against the indentation depth h (Figure 1.3, right). An example of a finally remaining imprint, exceeding the width of the CCML, is shown on the insert in Figure 1.3, left. In this insert, the approximated sizes of the remaining imprints at all load steps are marked and labeled from a to g. The results of step a, exhibiting indentation depths of less than 30 nm, were not considered due to possible contact problems. The indentation depth was in the range of the surface roughness then, so that it cannot be assured that the contact area A_C is determined accurately. This is reflected by a higher H in step a (Table 1.2). For the steps b to g, H did not show a distinct increase, even though the size of the remaining indents clearly exceeded the width of the CCML during the loading steps d to g (Figure 1.3 left). Thus, the indents had been partly placed in the adjacent S2 layer. Jakes et al. (2009) also reported only small effects of nearby edges on their results for hardness. The hardness even showed a slight overall decrease from 0.33 ± 0.02 GPa to 0.30 ± 0.02 GPa at indentation depths from around 200 nm (step b) to around 800 nm (step g, Figure 1.3 & Table 1.2), which represents trends of decreasing indentation hardness with increasing indentation depth, usually present in polymers at low indentation depths, i.e. below $1 \mu\text{m}$ (Briscoe et al., 1998; VanLandingham et al., 2001). Possible origins have been discussed, like tip blunting or other inaccuracies of the tip-area function of the Berkovich tip at low indentation depths (Nix and Gao, 1998). The fact that the CCML and the S2 layer show similar hardnesses (e.g. see Table 1.4) may explain to some extent that only small changes of hardness were observed with indentation depth. Moreover, existing slight differences between hardnesses obtained for different indentation depths might be masked by the generally high experimental scatter. This scatter results to a good part from the variability of the width of the CCML (typically ranging from 1.5 to $2.5 \mu\text{m}$). In more detail, the indentation modulus M did not significantly increase ($p=0.01$, paired t-test) from step b ($h=30\text{-}200$ nm: 7.10 ± 1.18 GPa) to step c ($h=250\text{-}300$ nm: 7.90 ± 0.68 GPa), confirming the results obtained by Jakes et al. Jakes et al. (2009), who also reported only small effects in the CCML from the nearby S2 cell wall layer at similar penetration depths. From step d ($h > 300$ nm: 9.02 ± 1.07 GPa) onwards, significantly higher values were obtained. This suggests 300 nm as a rough estimate for the limit indentation depth at which edge effects in the CCML start to become relevant. The corresponding width of the indent can be determined from the contact area A_C , which is related to the contact depth h_C by the so called tip-area-function $A_C(h_C)$ (Oliver and Pharr, 1992). For a maximum penetration depth h_{max} of 300 nm, which is always larger than h_C if sink-in behavior is present (Oliver and Pharr, 2004), this yields an upper bound of the contact area of $2.55 \mu\text{m}^2$, corresponding to a side length a of approximately $1.7 \mu\text{m}$. That means that the flanks of the Berkovich pyramid might already touch the S2 cell wall layer at a penetration depth of 300 nm for typical dimensions of the CCML in the NI-specimens used herein. Knowing the influence of the indentation depth on the measurement results, the choice of a maximum load of $250 \mu\text{N}$ in the stan-

standard indentation procedure can be checked. This load refers to indentation depths of 150 - 180 nm ($a \sim 0.9 - 1.1 \mu\text{m}$), for which no edge objects were observed in the tests. Moreover, the resulting M and H of the CCML, obtained at these indentation depths, lie within the range of values, reported by Wimmer and Lucas (1997).

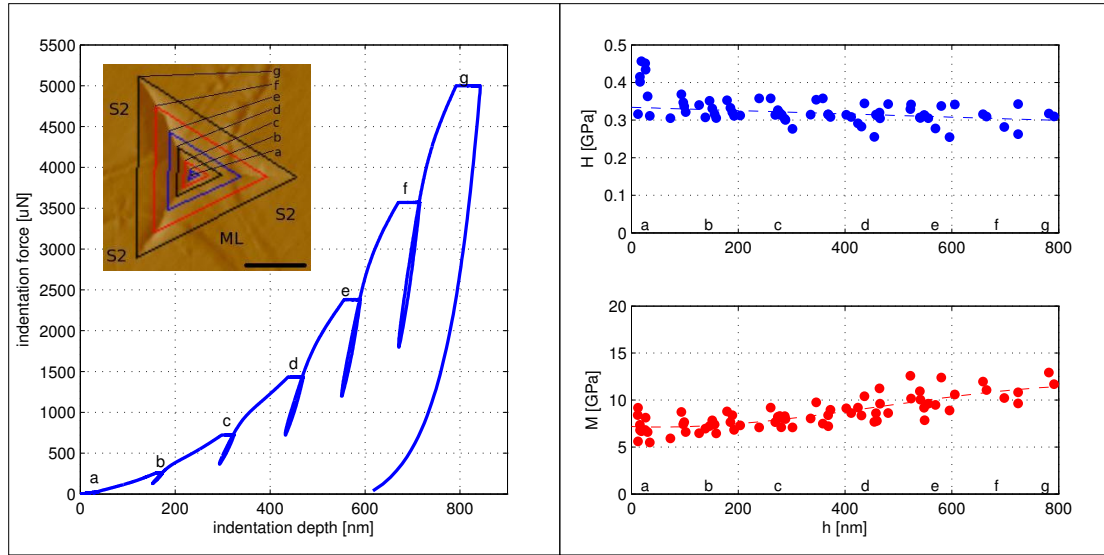


Figure 1.3: Indentation in cell corner middle lamella (CCML); left: approximated remaining imprints of the indentation steps (bar represents $2 \mu\text{m}$) and load-function for the continuous indentation test; right: indentation hardness H and modulus M over the corresponding indentation depths h (a-g) with trend lines

Table 1.2: Indentation modulus M and hardness H of the CCML with the corresponding indentation depth ranges of the steps a to g (Figure 1.3); *significant differences ($p < 0.01$, paired t-test) from values of step b

Step	h [nm]	M [GPa]	H [GPa]
a	<30	7.10 ± 1.18	$0.43 \pm 0.09^*$
b	30-200	7.35 ± 0.82	0.33 ± 0.02
c	250-300	7.90 ± 0.68	0.32 ± 0.03
d	350-500	$8.82 \pm 1.08^*$	0.32 ± 0.03
e	500-600	$10.11 \pm 1.50^*$	0.31 ± 0.03
f	~ 700	$10.74 \pm 0.88^*$	0.30 ± 0.03
g	~ 800	$11.77 \pm 0.90^*$	0.30 ± 0.02

1.3.2 Effects of Sample Drying

A slight loss of oven dry mass occurred after repeated wetting-drying cycles. It amounted to approximately 0.3%, 0.6%, and 0.75% after two (D2), three (D3), and four (D4) cycles, with respect to the dry mass of the small clear wood samples after the first

cycle (see Table 1.3). The equilibrium moisture content (EMC), however, remained unchanged throughout the drying cycles (Table 1.3). This indicates that no carbohydrates were lost, and that the mass loss was most likely caused by the extraction of soluble substances during water saturation and subsequent drying. The drying procedure was severe enough to not only initiate macroscopic lens-shaped cracks in R-direction in the $2 \times 2 \times 2 \text{ cm}^3$ cubes, already after the second cycle, but also microscopic ones in the S2 cell wall layer. The latter were used to determine the microfibril angle on thin sections. The indentation of the CCML yielded mean values of M ranging from 6.75 ± 0.58 to 7.10 ± 0.65 GPa for the samples REF to D4 (see Table 1.4 & Figure 1.4a). The slight increase of M with increasing number of drying cycles is within the range of the observed experimental scatter (Figure 1.4a) and was found not to be significant ($p=0.01$, paired t-test). H of the CCML showed an increase from 0.29 ± 0.02 to 0.32 ± 0.02 GPa for REF to D4 (Figure 1.4b). Only D4 showed significantly increased values. Similar observations were made for the S2 cell wall layer: M did not show any significant increase or decrease upon drying. M of sample D3 (18.55 ± 1.18 GPa) lay above all other measured values (17.32 ± 1.39 GPa to 17.71 ± 1.07 GPa, see Table 1.4 & Figure 1.4c), but this might rather be a consequence of locally smaller MFA in the first rows of LW tracheids (Wagner et al., 2013). H in the S2 cell wall layer also showed a slight overall increase from 0.33 ± 0.03 GPa to 0.36 ± 0.03 GPa for REF to D4, (Table 1.4 & Figure 1.4d). The additional surface specimen D4s showed higher H (by 6%) and M (by 5%) in the CCML than the corresponding specimen D4 from the interior of the same dried sample. Also H and M of the S2 cell wall layer of D4s were higher than in D4, by 4% and 6%, respectively. The slight increase of the hardness of both the CCML and the S2 cell wall layer might be related to the extraction of soluble substances during the drying-wetting cycles mentioned before. Such substances possibly act as plasticizing agents, which reduce the hardness but do not affect the effective stiffness of the material. The fact that M remains constant indicates that any possible re-arrangements of the wood polymers during the glass transition are such that they do not alter the elastic properties of the wood cell wall. The higher M in the specimen D4s, located at the surface of the specimen, might result from a stronger effect of the extraction towards the surfaces of the initial cubes. Moreover, again local MFA variations within the LW of that annual ring might have contributed to the increased stiffness (Wagner et al., 2013). The observed micro-cracks in the S2 cell wall layer apparently do not affect the mechanical properties determined by nanoindentation. This might be because of the compressive loading of the material during the indentation test, which results in crack closure upon loading.

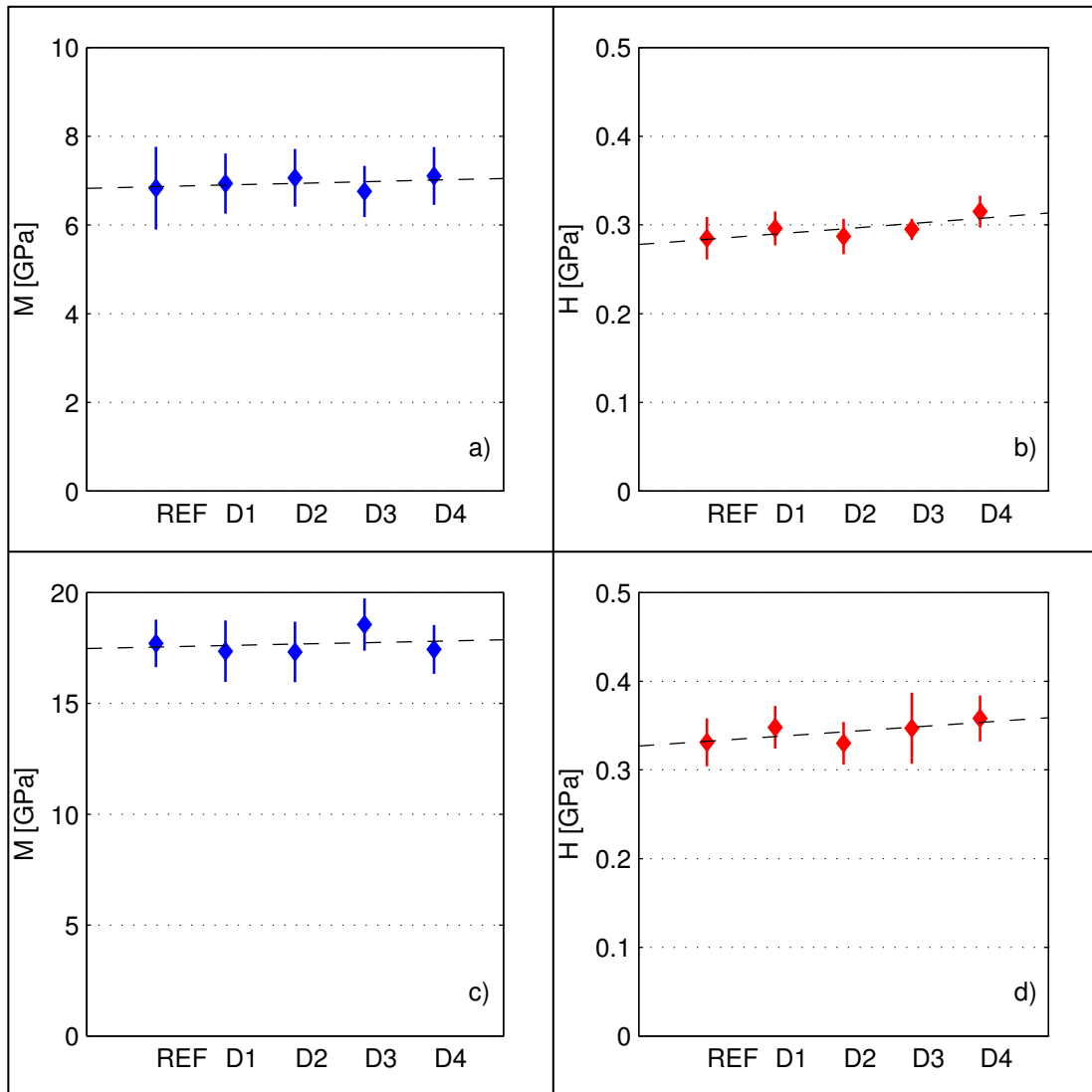


Figure 1.4: a) Indentation modulus M of the cell corner middle lamella (CCML); b) indentation hardness H of the CCML; c) M of the S2 cell wall layer; d) H of the S2 cell wall layer

1.3.3 Effects of Embedding Medium

Embedding in different resins did not result in significantly different M and H in the S2 cell wall layer of the NI-specimens (Table 1.5, $p=0.31$ and $p=0.15$, for M and H , respectively, paired t-test). This indicates that neither the different stiffnesses of the resins nor the different curing temperatures affected the indentation results. Similar findings have been reported for trabecular bone samples embedded in epoxy resins with stiffnesses differing up to a factor of approximately seven (from 0.54 GPa to 3.74 GPa (Mittra et al., 2006)). The mechanical properties of the two different embedding resins used herein were assessed by NI, using the standard procedure (three-step load function,

Table 1.3: Masses and equilibrium moisture contents (EMC) of the samples REF to D4 during repeated wetting and drying cycles, *based on a dry mass of 3.384 g determined afterwards

Step Sample	m_{ini} [g]	EMC_{ini} [%]	Dry #1 [g]	Dry #2 [g]	Dry #3 [g]	Dry #4 [g]	m_{fin} [g]	EMC_{fin} [%]
REF	3.763	11.20*	-	-	-	-	3.756	10.99*
D1	3.735	11.23	3.358	-	-	-	3.726	10.96
D2	3.507	11.33	3.150	3.141	-	-	3.487	11.02
D3	3.513	11.14	3.161	3.148	3.143	-	3.489	11.01
D4	3.407	11.12	3.066	3.056	3.051	3.043	3.378	11.01

Table 1.4: Indentation modulus M and hardness H of the S2 cell wall layer (S2) and cell corner middle lamella (CCML; mean \pm sd); *significant differences from REF (p<0.01, paired t-test)

	CCML		S2	
	M [GPa]	H [GPa]	M [GPa]	H [GPa]
REF	6.83 \pm 0.93	0.29 \pm 0.02	17.71 \pm 1.07	0.33 \pm 0.03
D1	6.93 \pm 0.68	0.30 \pm 0.02	17.35 \pm 1.39	0.35 \pm 0.02*
D2	7.06 \pm 0.65	0.29 \pm 0.02	17.32 \pm 1.36	0.33 \pm 0.02
D3	6.75 \pm 0.58	0.30 \pm 0.01	18.55 \pm 1.18*	0.35 \pm 0.04
D4	7.10 \pm 0.65	0.32 \pm 0.02*	17.43 \pm 1.10	0.36 \pm 0.03*
D4s	7.44 \pm 0.45*	0.33 \pm 0.01*	18.43 \pm 1.92	0.37 \pm 0.03*

250 μ N maximum load, 25 indents per specimen) and resulted in M of 5.12 \pm 0.07 GPa for the Agar Low Viscosity Resin Kit (A-LV) and of 3.97 \pm 0.16 GPa for the Struers EpoFix (S-EF), and H of 0.25 \pm 0.00 GPa for A-LV and of 0.21 \pm 0.02 GPa for S-EF.

Non-embedded LW cells in the center of the NI-specimen, did not show significantly different M and H either, compared to both the A-LV and the S-EF samples (Table 1.5), p=0.76 and p=0.05, for M and H , respectively, paired t-test). However, the standard deviations of M and H obtained for non-embedded cell walls were higher by factors of 3 and 2, respectively, than for embedded ones. Kim et al. (2012) tested apparently non-embedded softwood (Southern pine) LW cells in the center of a specimen, embedded in a pre-cured epoxy resin. They also found no significant differences in both M and H between embedded and nonembedded specimens together with a higher overall variability for the nonembedded specimens.

The higher experimental scatter observed for non-embedded samples might result from various sources. Particularly tangential cell walls are susceptible to delaminations and cracks within the cell wall during microtome cutting in radial direction when left non-embedded. The cracks extend from the plainly cut surface into the underneath material. Delamination may occur between cells in the middle lamella or between individual layers within the cell wall (Figure 1.5), e.g. by pulling off the S3 layer from

the S2 layer as the knife passes the interface from the cell wall to the lumen. Extending from these delaminations in the tangential walls, cracks may occur in the radial cell walls near the cell corners (Figure 1.5).

However, damage during cutting should not only lead to a higher experimental scatter but also to a decrease of the mean values of M and H , which was not observed. It might be that some other effects have counteracted such a decrease of the indentation results. For example, locally higher MFAs in the non-embedded samples might have caused an increased stiffness and hardness of the (sound) cell wall material. Another possible origin of the higher experimental scatter might be slight random misalignments of the specimens in tangential direction. An inclination of the sample around the radial direction with respect to the indentation direction would lead to an apparently higher MFA in one tangential cell wall and an, by the same amount, apparently lower MFA in the opposite tangential cell wall of one wood cell. This might explain the observed increased variability (SD) of the indentation moduli at equal mean values.

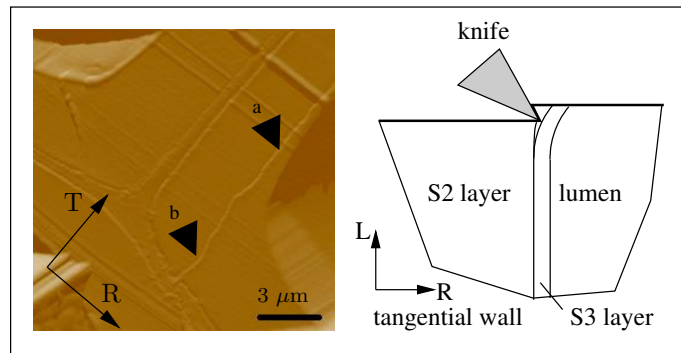


Figure 1.5: Delamination in tangential cell wall (a) and a crack, extending from this delamination, near the cell corner (b), induced during cutting of non-embedded cell wall (left) and proposed delamination mechanism, i.e. S3 layer is pulled off the S2 layer during cutting (right)

Table 1.5: Indentation modulus M and hardness H of the S2 cell wall layer using different embedding materials and techniques (mean±sd)

	REF	E1	E2
Sample	(Agar LV Kit)	(no vacuum, Agar LV Kit)	(Struers EpoFix)
M [GPa]	17.71 ± 1.07	17.67 ± 3.06	18.23 ± 1.36
H [GPa]	0.33 ± 0.03	0.36 ± 0.06	0.35 ± 0.03

1.4 Concluding Remarks

Herein, the influence of (1) potential edge effects during the indentation of the cell corner middle lamella (CCML), (2) of heating and drying during sample preparation,

and (3) of different embedding epoxy resins on the results of nanoindentation tests on softwood cell walls were studied.

No differences in the stiffness and hardness of the CCML were found when the contact area A was increased up to approximately the size of the CCML. Even slightly exceeding this size did not cause an instant drastic increase. Thus, no edge effects, due to interfaces between CCML and the surrounding S2 cell wall layers were observed for indentation depths h up to 150-180 nm in the investigated samples. Rather, the measured indentation moduli M and hardnesses H exhibited usual ranges and scatter. Related contact areas approach typical sizes of the CCML between LW tracheids in Norway spruce.

Water saturation followed by harsh drying hardly affected the measured mechanical properties of the S2 cell wall layer and the CCML. Repeated cycles of water saturation and severe drying, however, resulted in a slight increase of M and H in the CCML. H also increased slightly in the S2 cell wall layer, while no changes of M could be identified there. The observed increases might be explained by the extraction of some soluble agents from the cell wall. Possible rearrangements of the wood polymers lignin and hemicelluloses, in consequence of exceeding the glass transition temperature during the curing of the resin, seem not to change the mechanical behavior of the wood cell wall during indentation tests. Therefore, heating of the samples when curing the resin in the embedment procedure can be expected to not influence the mechanical properties of the wood cell walls as determined by nanoindentation.

Using different embedding materials did not result in changes of the measured mechanical properties of the S2 cell wall layer. Also indentation of apparently non-embedded wood cell walls did not yield significantly different M and H . Due to the lack of support of the cell walls by an embedding material during microtome cutting, the wood cell walls are frequently damaged, leading to a higher variability of the obtained results.

Effect of Water on the Mechanical Properties of Wood Cell Walls – Results of a Nanoindentation Study (Wagner et al., 2014d)

Authored by Leopold Wagner, Clémence Bos, Thomas K. Bader, Lauri Rautkari and Karin de Borst

Submitted to *Holzforschung*, 2014

Water significantly reduces the mechanical resistance of wood. While this effect is well analysed and quantified on the macroscale, few studies have addressed this issue at the cell wall scale. Stepping down in length scales enables to exclude the influence of the inevitable large variability of the cellular structure of wood, which impedes comparisons between samples, and to probe cell wall layers individually. Herein, we report on a nanoindentation study on five different wood species, in which elastic and creep properties of the S2 layer and the middle lamella were determined. Measurements were carried out at relative humidities ranging from 10 to 80% as well as under water. Indentation moduli were found to decrease by about a third in the S2 layer and by about a half in the middle lamella between relative humidities of 10% and 80%. The steepest decline of the indentation moduli is encountered between moisture contents of 5 and 10%, which results for some samples in a pronounced S-shape of the curve showing indentation modulus over moisture content and is ascribed to the plasticisation of hemicellulose. Immersion into water results in a further drop of the indentation modulus to about 20-30% of its value at 10% relative humidity. This may be caused by the additional softening of para-crystalline regions of the cellulose fibres.

2.1 Introduction

Wood is a hygroscopic material and adsorbs and desorbs water in reaction to changes of the environmental humidity. The reduction of the mechanical resistance and the dimensional changes upon moisture uptake are highly adverse effects from an engineering point of view and are considered as one of the main barriers against a more intensive use of wood for constructive purposes. In consequence, the wood-water interactions have been studied intensively already since the early 20th century. Despite the efforts, there is still a lot of uncertainty about the mechanisms how moisture is taken up and incorporated into the structure, and – in consequence – how it affects the material behaviour.

Most experimental investigations were carried out on macroscopic samples. However, wood is a cellular material, and particularly the density and the cell structure are prone to a high natural variability. This makes it difficult to compare results obtained on different samples and species, and to extract the common trends from influences of microstructural variability. This motivates to assess the material properties at the cell wall scale, where the effect of moisture can be tested more immediately, and where influences of the cellular structure and the overall mass density of wood are eliminated. Moreover, testing at smaller length scales allows to probe different cell wall layers individually. Their different composition and structure should deliver enhanced insight into the effects of water on the material and its mechanical behaviour.

Being introduced into wood science by Wimmer et al. (1997), nanoindentation has established itself as one of the main mechanical testing method for wood cell walls (cf. e.g. review by Eder et al. (2013)). Herein, we have applied nanoindentation to samples of five different wood species at four different relative humidities between 10 and 80% and under water. Both the S2 cell wall layer, which constitutes the by far thickest and stiffest layer, and the middle lamella, which connects neighbouring wood cells, were tested. In addition to the indentation modulus, also creep parameters in terms of increased deformation under constant loading were determined. The scope of the study in terms of moisture conditions and variety of samples goes well beyond that of previous investigations. All samples have undergone comprehensive microstructural characterisation (Bader et al., 2012c; de Borst et al., 2012; Wagner et al., 2013), which enables a systematic comparison of the obtained results with respect to the composition and the morphology of the individual samples. This is expected to deliver enhanced insight into the role of specific wood polymers and their arrangement in the cell wall layers in relation to the softening effect of water on wood.

Before the experimental campaign is outlined and discussed, we briefly review and summarise existing test results for the elastic and viscoelastic properties of wood at different moisture contents, as well as the current understanding of wood-water interactions.

2.2 State-of-the-art

The stiffness is commonly found to first slightly increase from the dry state up to moisture contents of about 5%, from where onward the stiffness continuously drops with increasing moisture until the fibre saturation point is reached (e.g. Gerhards (1982); Kollmann (1982); Skaar (1988)). Gerhards (1982) summarized results of a large number of studies on various wood species and arrives at a drop of the elastic modulus in longitudinal direction by 10 to 20% between moisture contents (MC) of 12 and 20%, and by 5 to 25% over the same moisture range in the radial and tangential direction. Changes of similar magnitudes were measured on single wood fibres. Eder (2007) found that the elastic modulus of a wet spruce fibre in fibre direction was lower by 25% compared to the fibre at conditions of 65% RH at 20°C, which relates to approximately 12% MC. Ehrnrooth and Kolseth (1984) obtained ratios between 2.47 and 4.75, with a mean of 3.07, for the elastic modulus of a spruce fibre at 50% RH and water soaked. They observed that the content of hemicelluloses and lignin only marginally affects the measured moduli. Kersavage (1973) tested fibres of Douglas fir at MCs between 0 and 17% and above the fiber saturation point. Compared to their highest value at 6% MC, the modulus in the dry state was 7% lower, and the one at a MC of 17% was 11% lower. In the wet state, it dropped to about half of the maximum. As for creep, Ehrnrooth and Kolseth (1984) report an increase of displacement up to about 10% over a period of 10 s, which depends on the applied load. Olsson et al. (2007) observed a creep strain rate of 0.041 and 0.044%/s in spruce fibres at stresses of 280 MPa and 440 MPa, respectively, at a relative humidity of 80%.

Nanoindentation has already been applied to study the elastic behaviour of wood cell walls at different MCs (Yu et al., 2011; Li et al., 2014). Yu et al. (2011) reported a linear decrease of the indentation modulus of Masson pine by 17% from a MC of 4.5% to a MC of 13.1%. The corresponding creep rate at constant load was about 1.5-1.8 nm/s at MCs between 4.5% and 7.7%, increasing up to 2.2 nm/s at 13.1% MC. Li et al. (2014) reported no significant changes of the creep rate for Masson pine cell walls in a MC range of 5 to 8%, whereas increasing MFA lead to higher creep rates. They also reported the indentation modulus to decrease by 6.5 to 12.3% going from 5 to 11% MC, depending on the MFA. Similar measurements by Jakes et al. (2009) found an increase of 25% in indentation depth over 20 s on Loblolly pine samples.

2.3 Materials and Methods

2.3.1 Samples

Investigations were carried out on wood samples of three softwood species, namely Norway spruce (*Picea abies* [L.] Karst.), Common yew (*Taxus baccata* L.), and Scots pine (*Pinus sylvestris* L.) as well as two hardwood species, namely European beech (*Fagus sylvatica* L.) and European oak (*Quercus robur* L.). The sample material has undergone microstructural and compositional characterisation (Bader et al., 2012c; de Borst

et al., 2012; Wagner et al., 2013), which is summarized in Table 2.1. Small wood specimens (approx. $1.5 \times 2 \times 1 \text{ mm}^3$ in longitudinal, radial, and tangential direction) were cut from the latewood (LW) region of annual rings investigated in the mentioned characterisation campaign. Following the protocol proposed by Wagner et al. (2014a) for the sample preparation, the specimens were embedded in a resin to stabilise the wood cell walls. The cross sectional surface of the embedded samples was cut smooth, using a microtome equipped with a diamond knife. The specimens were stored in ambient conditions of $20 \pm 2^\circ \text{C}$ and 30-40% relative humidity (RH) prior to embedding, and had to be heated during resin curing to 60°C for 24 hours (Wagner et al., 2014a), which will have led to partial drying of the samples. After curing, the samples were conditioned at the same ambient conditions again as before the embedding. It has to be kept in mind that the embedding resin might have restrained the swelling of the wood specimens during the changes in MC and thus have induced stresses and possibly damage such as microcracks.

Table 2.1: Microfibril angle (MFA) and composition in terms of mass fractions of cellulose (w_{CEL}), hemicelluloses (w_{HC}), lignin (w_{LIG}), and extractives (w_{EXT}) of the investigated wood samples (a...(Bader et al., 2012c), b...(Wagner et al., 2013), c...(de Borst et al., 2012))

sample	MFA [$^\circ$]	w_{CEL}	w_{HC}	w_{LIG}	w_{EXT}	ref.
Norway spruce	12.5	49.1	24.4	23.7	2.8	a
Common yew	27.0	44.7	20.8	23.9	10.6	a
Scots pine	12.7	46.6	27.1	23.5	2.5	b
European beech	7.0	49.1	25.0	23.2	2.7	c
European oak	3.0	40.8	32.2	21.0	6.0	c

2.3.2 Nanoindentation

The nanoindentation tests were carried out using a Triboindenter[®] (*Hysitron Inc.*, Minneapolis, MN, USA), equipped with a three-sided pyramid-shaped tip (Berkovich type) in load controlled mode. The measurement chamber of the Triboindenter[®] was climatized to $22 \pm 1^\circ \text{C}$ and in steps to 10, 40, 60, and 80% RH, respectively, using a RH-200 Relative Humidity Generator (*L&C Science and Technology*, Hialeah, FL, USA). For tests under water, i.e. under fully saturated conditions, the sample was put in a small container, which was clamped to the magnetic table of the Triboindenter[®] by the aid of the small steel discs, onto which the specimens were mounted during sample preparation. To limit the variability of the results, all indents at different RH were performed within an area of approximately $200 \times 200 \mu\text{m}^2$ within the LW region of each sample. The position of the indents on the respective cell wall was chosen from scanning probe microscopy (SPM) images, recorded with the in-built SPM in the Triboindenter[®]. For the tests under water, the indenter tip was removed from the surface after SPM imaging and the container was then filled with water until the sample was covered by approximately 2 mm of water. 30 min after immersion the indents were performed (Yu et al.,

2011). Indents were placed in the S2 layer of LW cells as well as in the middle lamella (ML) in the cell corners between those LW cells. The applied two-step load function consisted of loading to the half of the later applied maximum load P_{max} , holding that load level for 15 s, partial unloading to one quarter of P_{max} , reloading to P_{max} , holding that load level for another 15 s, and complete unloading. P_{max} was set to 200 μN for the S2 layer and to 130 μN for the ML, respectively. These loads had to be reduced for the tests at 80% RH and under water to 150 μN (S2) and 90 μN (ML), in order to fulfil the required distance of the indent to the nearest interface to avoid possible edge effects (Jakes et al., 2009). The resulting load-penetration depth curves were analysed following the approach by Oliver and Pharr (1992), relating the initial slope of the unloading segments of the curves (initial unloading stiffness S) to the so called indentation modulus M by:

$$M = \frac{\sqrt{\pi}S}{2\sqrt{A_C}}, \quad (2.1)$$

where A_C is the contact area. In addition the indentation creep C was defined as follows:

$$C = \frac{h_1 - h_0}{h_0} \times 100\%. \quad (2.2)$$

where h_0 and h_1 are the indentation depths at the start and at the end of the holding phases (CSM Instruments, 2002). The indentation depths at half and at full load lie within the range where no effects of the indentation depth on M , beyond the usual experimental scatter, are to be expected (Tze et al., 2007; Wagner et al., 2014a). Thus, M was evaluated at half and full load together. Less is known about potential influences of indentation depth on the creep behaviour, so that C was evaluated separately for the first ($C1$) and the second holding phase ($C2$).

2.3.3 Environmental Scanning Electron Microscopy (ESEM)

Environmental scanning electron microscopy was applied to check whether the cell walls of the embedded wood specimen were able to shrink and swell upon MC changes. Within the same specimen, walls of cells filled with embedding material as well as walls of cells apparently empty were investigated by means of a scanning electron microscope (Quanta 200, FEI, Hillsboro, OR, USA). The images were recorded at a magnification of 15000, using 10 to 20 kV acceleration voltage and the climatic conditions were 20°C and water vapour pressures of 5 and 20 mbar, corresponding to approximately 20 and 75% RH, respectively.

2.3.4 Dynamic Vapour Sorption (DVS)

The equilibrium MCs (EMC) at the set RH were analysed from small matched wood samples of approximately 20 mg which were prepared using razor blade. The analysis was performed using a Dynamic Vapour Sorption Extended Temperature (DVS-ET) apparatus (Surface Measurement Systems, London, UK). First the samples were dried

under dry nitrogen gas flow ($200 \text{ cm}^3/\text{min}$) until a MC 0%, followed by a sorption cycle with RH steps 0-10-40-60-80% at 22°C . The DVS-ET apparatus maintained a constant RH until the change in the sample mass was lower than 0.002% over a 10 min period to ensure a constant equilibrium condition after each RH step.

2.4 Results

2.4.1 ESEM

Figure 2.1 shows exemplary ESEM images of apparently non-embedded European oak cell walls at 20 and 75% relative humidity, respectively. The thicknesses of corresponding cell walls were measured in both states, and their expansion in relation to the values at 20% humidity calculated. This yields a qualitative measure of the deformations of embedded and non-embedded cell walls. Both expansion and compression of cell walls could be detected, ranging from 3.5% compression to 14.5% expansion, regardless of the respective species and whether the cell walls were embedded or non-embedded. This shows the limitations of assessing overall dimensional changes from individual cell wall measures. Similar findings of compressed cell walls with increasing MC have been reported before (Sakagami et al., 2007) and have been associated with inaccuracies of the measurement method – which cannot be ruled out here either – and with the cell geometries and the cell wall microstructure. However, no significant differences of thickness changes between embedded and non-embedded cell walls were detected in the current investigation. Despite the mentioned deficiencies, this observation gives confidence that the embedding has not affected the nanoindentation results.

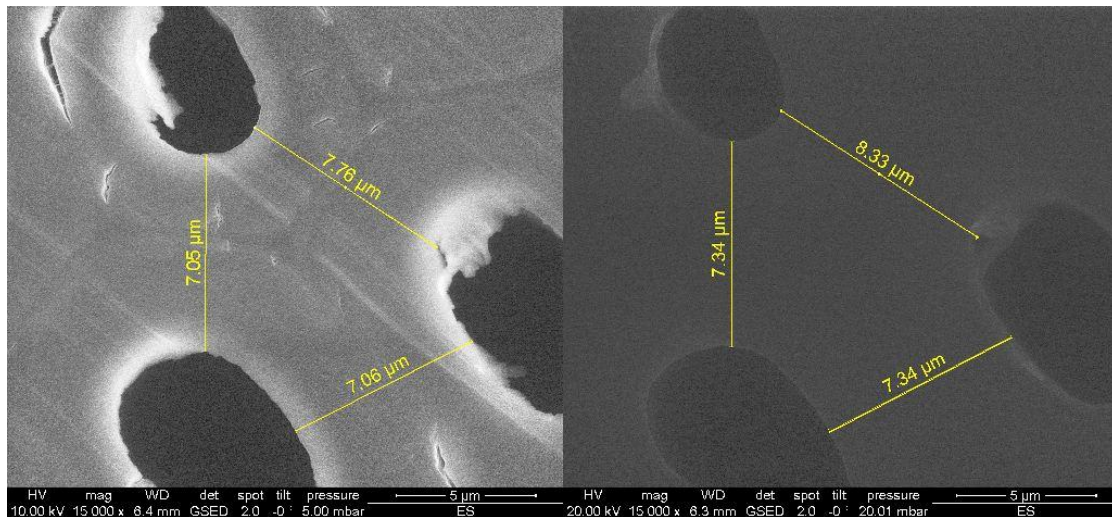


Figure 2.1: ESEM images of non-embedded European oak cell walls at 5 and 20 mbar water vapour pressure, corresponding to approximately 20 and 75% RH

2.4.2 DVS

The equilibrium MCs of the samples, determined by means of DVS, are summarised in Table 2.2. They will be used for the interpretation of the indentation results in the discussion section. It should be noted that the EMCs relate to the whole wood samples, and that the local MC in the ML and the S2 layer, respectively, will slightly deviate from these values. Since the current study focusses on qualitative effects of moisture on cell wall stiffness and creep, no attempt is made to determine these layer-specific EMCs from the measured ones, based on chemical composition and component-specific sorption capacities.

Table 2.2: Moisture contents (MC) of the five different species at the investigated climatic conditions of 22°C and different relative humidities (RH), resulting from the DVS measurements

Species	10%	40%	50%	60%	70%	80%
Scots pine	3.8	7.2	8.2	9.4	11.3	14.6
Norway spruce	3.5	7.0	8.1	9.5	11.5	14.1
Common yew	3.0	4.7	5.5	6.4	8.0	10.6
European oak	2.4	4.6	5.5	6.8	9.1	11.7
Common beech	2.7	5.4	6.4	7.9	10.2	13.1

2.4.3 Nanoindentation

The results of the nanoindentation tests are shown in Figures 2.2-2.4, in terms of the sample-specific indentation moduli and creep parameters of ML and S2, respectively, as functions of relative humidity. Inter-species trends at a certain relative humidity can be identified by markers of the same colour.

The indentation moduli show a pronounced decrease at increasing relative humidity from 10 to 80% RH, followed by a further significant drop to their values in the wet state. The observed trends are similar for the ML and the S2 layer and across all species (Figure 2.2). Also the absolute values are quite similar, except for the moduli of the S2 layer in yew at conditions of 10 to 80% RH, which fall considerably below comparable results obtained for other species.

The influence of moisture is even more pronounced for the creep parameters than for the indentation moduli. Particularly in the ML, the results show a two-level behaviour with a step change between 60 and 80% RH and only little variability of the results with humidity otherwise. The influence of moisture is more gradual in the S2 layer. Only for yew, the described step change is observed in the S2 layer as well.

The influence of moisture is qualitatively the same for both creep parameters. The second creep parameter $C2$ (Figure 2.4), related to the second holding phase at the maximum load, is consistently about 25-30% lower than the first parameter $C1$ (Figure 2.3), related to the first holding phase at half of the maximum load. This counterintuitive

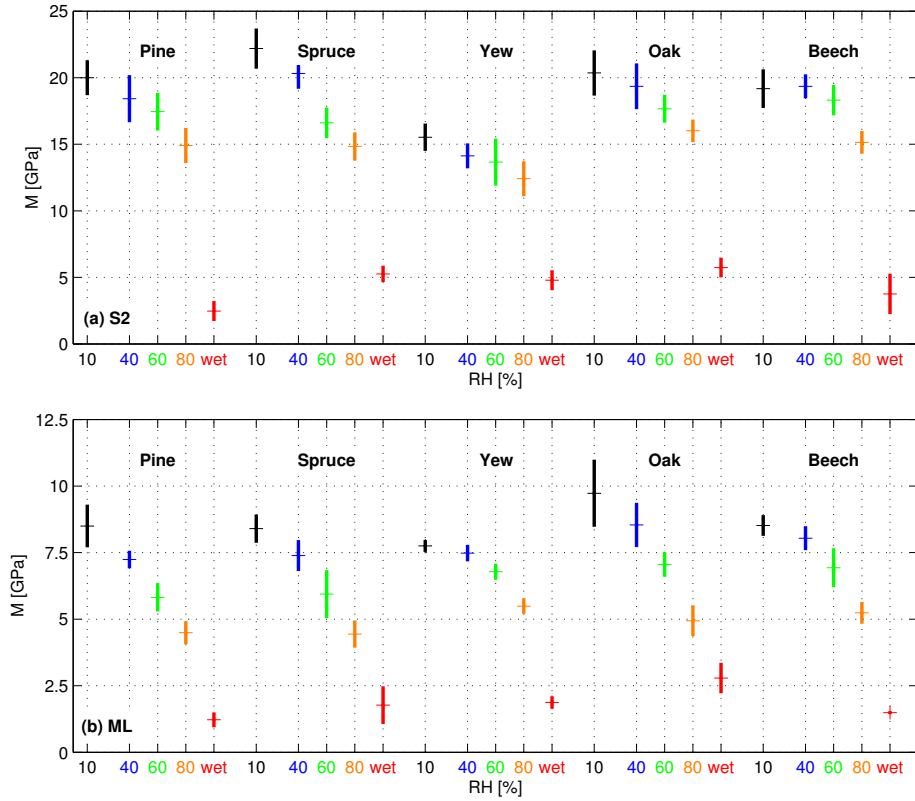


Figure 2.2: Indentation modulus M in (a) S2 layer and (b) middle lamella (ML) at different relative humidities (RH)

trend could be explained by the fact that the higher load causes plastic deformations and potential micro-damage in a larger area and may reduce creep in these zones.

It is unclear why the results for the creep parameters of the ML in beech are consistently lower in the wet state than at 80% RH. This may have been caused by a local inhomogeneity of the sample at the position, where $C1$ and $C2$ were measured. Indeed, while $C1$ and $C2$ were measured at exactly the same point without moving the indenter tip in between the measurements, the tests at different RHs could only be realised in close vicinity to each other.

2.5 Discussion

2.5.1 Indentation Moduli

In order to further elucidate the influence of MC on the indentation results, and to allow comparisons between the samples, relative courses of the indentation modulus over MC were plotted (Figure 2.5), with the values at 10% RH serving as reference. Moisture content has been chosen as independent variable rather than the relative humidity, since it is directly characterising the physical state of the cell wall.

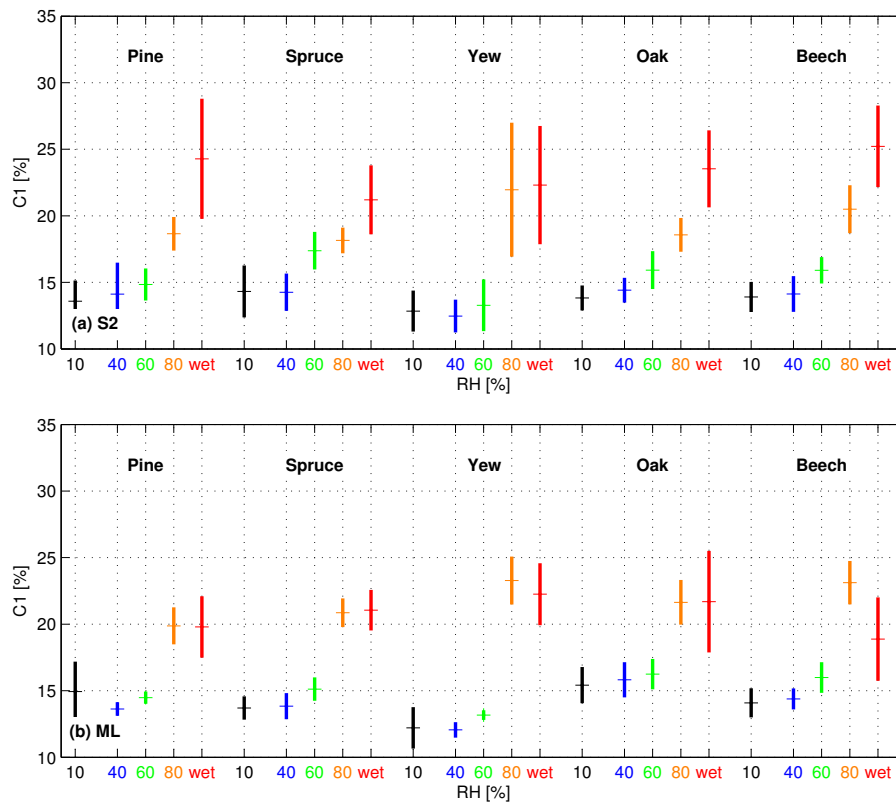


Figure 2.3: First creep parameter $C1$ in (a) S2 layer and (b) middle lamella (ML) at different relative humidities (RH)

All curves show the crucial influence of moisture on the indentation results. In the middle lamella (ML), the modulus at 80% RH is only around half of its value at 10% RH. In the S2 layer, the indentation modulus drops less, with ratios of moduli at 10 and 80% RH, respectively, of around 0.7. The variability of this ratio between species is higher in the S2 layer than in the ML. This variability could stem from the different MFAs of the samples. Indeed, the hardwood samples with lower MFAs exhibit higher ratios than the softwood with higher MFAs (Table 2.1). This is consistent with the fact that the amorphous polymeric matrix in between the cellulose fibres is more affected by moisture than the fibres themselves, and that it more strongly influences the overall cell wall behaviour at higher MFA (Kojima and Yamamoto, 2005). Higher indentation moduli at lower MFA were also measured by Li et al. (2014).

When immersed into water, the indentation moduli in the ML and the S2 layer level out at rather similar values relative to the initial moduli, typically in the range of 20-30% of the values at 10% RH. The ratios tend to be slightly lower for the ML. On the whole, the observed trends are well in line with previous measurements on fibres and cell walls reported in the state-of-the-art section. Due to the limited size of the data set, the moisture sensitivity of the indentation moduli could not be definitively correlated to the chemical composition of the samples (Table 2.1).

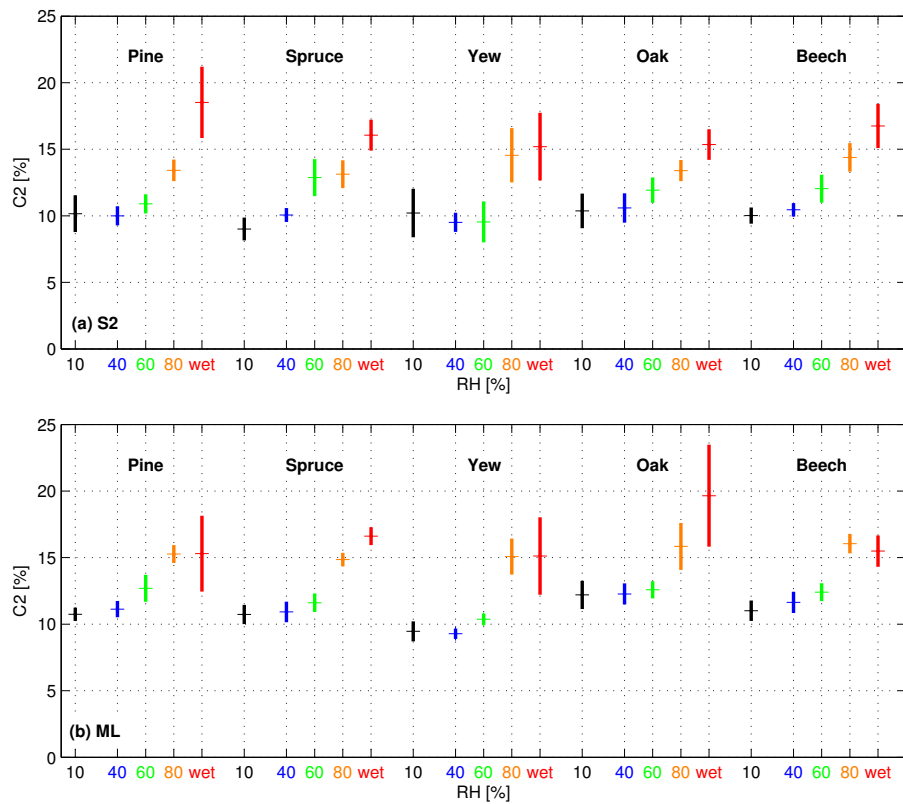


Figure 2.4: Second creep parameter $C2$ in (a) S2 layer and (b) middle lamella (ML) at different relative humidities (RH)

The results for the yew sample showed some peculiarities. The absolute values in the S2 layer were considerably lower than for the other samples, which is most likely because of the high MFA of yew. As regards the moisture influence, rather similar relative reductions of the indentation moduli from 10% RH to 80% RH were found in both the ML and the S2 layer, with ratios of 0.71 and to 0.8, respectively. These ratios are moreover considerably higher than in the other samples. However, also the moisture uptake in yew was much smaller at the same relative humidity. Its equilibrium moisture content of only 10.6% at 80% RH clearly falls below the EMCs of 14-15% for the other softwood samples at this RH (Table 2). This might be a consequence of the high content of extractives in yew, which are particularly concentrated in the ML and might have caused the observed lower moisture influence there. The results in yew at 80% RH compare well with the results in other softwood samples at 60% RH, which relate to comparable MCs. This underlines the physical relevance of the MC rather than relative humidity. In the S2 layer, the positive effect of reduced hygroscopicity of yew could have been outweighed by the high MFA of the sample (Table 2.1), which increases the relative influence of the matrix on the cell wall behaviour (Kojima and Yamamoto, 2005). Interestingly, the relative indentation moduli of yew measured under water are well in line with the results measured on other samples. This might indicate that the

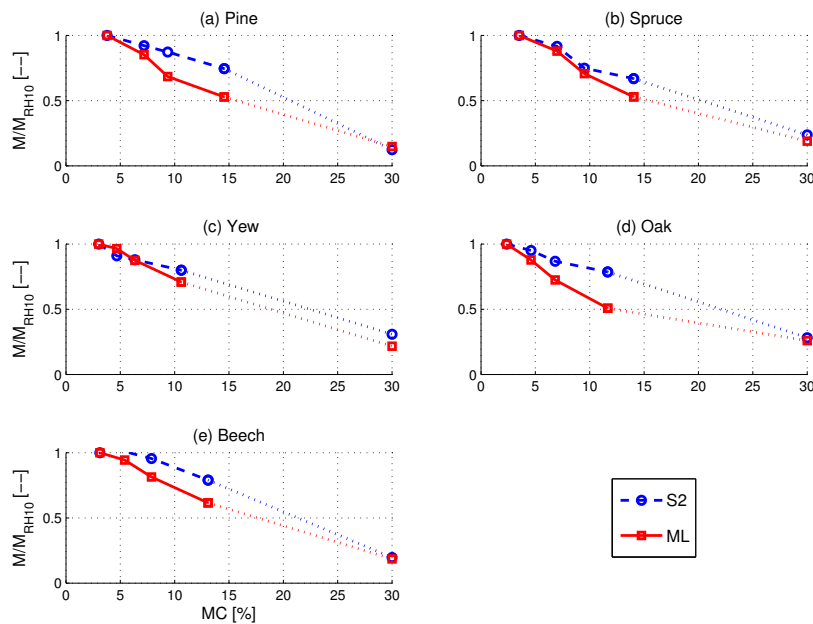


Figure 2.5: Relative course of indentation modulus M over moisture content (MC) – markers relate (from left to right) to 10, 40, 60, 80% RH and the wet state (these curves still need to be edited when the data in Table 5.2 is complete)

final sorptive capacity of yew is similar to that of the other species, but that sorption picks up only at higher relative humidities.

Most curves in Figure 2.5 exhibit the steepest descent at intermediate MCs of 5-10%. This is particularly pronounced for the ML in pine and spruce, and for the S2 layer in spruce and oak, resulting in an S-shaped course of the modulus over MC. It indicates that a transition occurs from a region with high moduli at low MC (<5%) to a region of low moduli at high MC (>10-15%). Indeed, the glass transition of the hemicelluloses has been reported to happen at moisture contents between 10 and 20% at room temperature (Kelley et al., 1987; Stelte et al., 2011), and could be responsible for the observed drop. Cousins (1978) tested extracted hemicellulose and found only a small variation of the Young's modulus in the range of moisture contents between 0 and 10%, but a drop by nearly three orders of magnitude above 10% up to saturation.

The glass transition of the hemicelluloses has been invoked before to explain transitions observed for the mechanical behaviour of wood: Examples include a secondary transition in moist spruce wood at room temperature found by means of DMTA (dynamic mechanical thermal analysis) by Kelley et al. (1987), and a transition at 5°C in spruce at 9% MC measured by the same method by Stelte et al. (2011). Salmén (1982) invoked the glass transition of the hemicelluloses to re-produce experimental data by Carrington (1922), in particular the considerable drop of stiffness at MCs between 10 and 20%, using a micromechanical cell wall model.

The corresponding local MC in the hemicelluloses is expected to be higher than the overall content in wood. An estimate of the MC of the hemicelluloses can be obtained by scaling the overall MC with the concentration of the hydroxyl groups in the hemicelluloses and in wood, respectively, which constitute the main sorption sites for water in wood (Engelund et al., 2013). This yields a MC of 15% in the hemicelluloses at an overall MC of 10% in wood.

In the in-situ state in wood, the local environment of the polymer chains affects the segmental mobility of the polymer chains and, thus, the MC at which the glass transition happens (Struik, 1987). This takes effect particularly in the S2 layer, where the vicinity of crystalline areas can limit polymer mobility and shift the glass transition to higher MCs at a given temperature than would be observed for the polymer in the extracted state. Salmén (1982) concludes for cellulose that the softening occurs over a broad range of MCs, at room temperature ranging from 80% relative humidity to full immersion in water. This brings about a rather gradual transition of the mechanical properties over MC, as observed in the nanoindentation tests, rather than in a step-like decline. It may cause that no S-shape forms at all, as is for example observed for the S2 layer of pine and beech.

The softening effect of water results from the breaking of hydrogen bonds in the wood polymers by the water molecules entering the cell wall. The bond breaking not only increases the polymer mobility and enables the glass transition, but also reduces the stiffness of the polymer. It shows up in a continuous reduction of the indentation modulus over increasing MC. This reduction is superimposed to the more rapid decline upon the glass transition and may also mask the S-shape expected for the latter. This might be the case of the indentation curves for the ML of oak and beech, which show a rather gradually decreasing trend. Moreover, the lack of a backward bend in many curves may be a consequence of investigating only relative humidities up to 80%. It is well possible that the moduli level out again at humidities higher than those observed. Likewise, the lack of a downward bend at low MCs might result from the existence of softening effects from the lowest investigated relative humidity onwards. Investigations at more extreme relative humidities will clarify this in the future.

Upon immersion in water, also the disordered regions of cellulose soften, resulting in a larger drop of the modulus and, thus, another step change compared to the level resulting from the glass transition of the hemicelluloses alone (Salmén, 1982). The restraining effect of the crystalline sections of the cellulose microfibrils can explain the lower reduction of the modulus at high MCs in the S2 layer compared to the ML. However, one would expect that this also brings about a higher variability of the glass transition points in this layer, resulting in a stretch of the transition over a broader moisture range. The opposite is observed, namely a more gradual transition in the ML. It remains a matter of speculation why this is the case.

2.5.2 Creep Values

The creep parameters at half load ($C1$) and at maximum load ($C2$, Figures 2.6 and 2.7) show the transition at MCs between 5 and 15% more clearly. They show a distinct upward bend, while being almost constant at lower MCs. This suggests a significant increase of creep in the rubbery state after going through the glass transition. This observation seems to be in contrast with Li et al. (2014), who report no significant influence of the MC on the creep behaviour. However, the highest relative humidity investigated by these authors was 60% RH. In the current test series, the upward bend of the creep parameters in the pine sample only happens between relative humidities of 60% and 80%. Thus, Li et al. (2014) might have missed this transition.

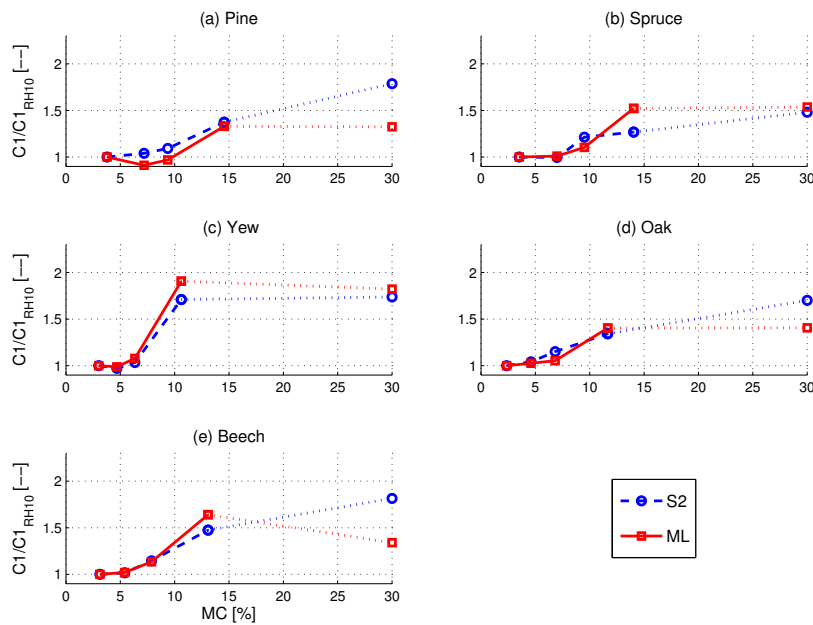


Figure 2.6: Relative course of first creep parameter $C1$ over moisture content (MC) – markers relate (from left to right) to 10, 40, 60, 80% RH and the wet state (these curves still need to be edited when the data in Table 5.2 is complete)

The creep parameters only show a rather small further increase when the sample is immersed to water in the S2 layer. In the middle lamella, they even remain more or less constant. Different from the indentation moduli, the softening of less ordered parts of the cellulose in addition to the hemicelluloses does not seem to cause significant additional creep. As mentioned in the results section, the drop of the creep parameters in the middle lamella of beech is not considered to be physically caused but rather by the local variability of the material.

The creep parameters show similar trends in all samples, though the variability is higher than for the indentation moduli. The transition is generally less pronounced and more gradual in the S2 layer than in the ML, which may be a consequence of the re-

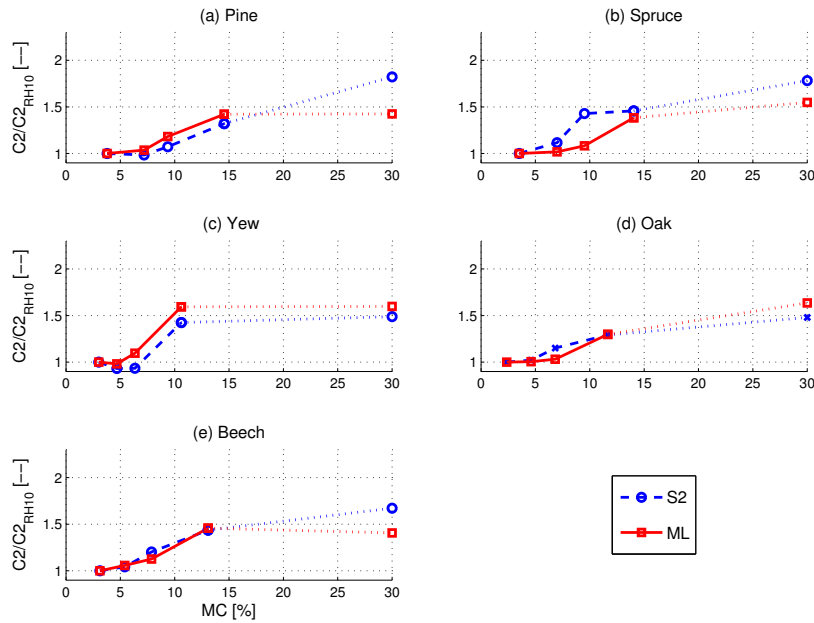


Figure 2.7: Relative course of second creep parameter $C2$ over moisture content (MC) – markers relate (from left to right) to 10, 40, 60, 80% RH and the wet state (these curves still need to be edited when the data in Table 5.2 is complete)

straining effect of the crystalline sections and the resulting spread of the glass transition over a larger moisture range, as explained in relation to the indentation moduli. The transition is most evident in the yew sample, where real step-changes are observed between RHs of 60% and 80%, respectively. Because of the higher MFA of yew, the results show more directly the behaviour of the amorphous matrix, and reduce potential distributing effects of the cellulose microfibrils. Again, the small data set prevents any conclusions on the influences of the chemical composition of the samples (Table 2.1) on the creep parameters and their dependence on the MC.

2.6 Conclusions

Nanoindentation was applied to investigate the influence of moisture on the elastic and creep properties of wood cell walls. The S2 layer and the middle lamella of five different wood species (spruce, pine, yew, beech, and oak) were tested at relative humidities between 10% and 80% as well as immersed in water.

Indentation moduli were found to decrease significantly with increasing humidity. They dropped by about a third in the S2 layer and by about a half in the middle lamella between relative humidities of 10% and 80%. In general, variability is higher in the S2 layer, which might be a consequence of the varying microfibril angle in this layer. Consistent with the stronger effect of moisture on the hemicellulose-lignin matrix compared

to the cellulose fibres, the effect of moisture is more pronounced in the middle lamellae, and it increases in the S2 layer with rising microfibril angle.

The steepest decline of the indentation moduli is encountered between moisture contents of 5 and 10%, resulting for some samples in a pronounced S-shape of the curve showing indentation modulus over moisture content. This indicates a transition in the material, which is ascribed to the plasticisation of hemicellulose. Significant stiffness losses upon the glass transition of the hemicelluloses have been observed before for macroscopic wood samples. Immersion in water results in a further drop of the indentation modulus to about 20-30% of its value at 10% relative humidity. This may be caused by the additional softening of para-crystalline regions of the cellulose fibres.

The creep data exhibit this transition even more clearly. In the softened state, creep is typically 50% higher than in the glassy state. Particularly in the middle lamella, only minor influences of changing relative humidity are observed outside of the transition region, and also immersion in water does not cause any further increase of the extent of creep. In the S2 layer, a further rise of about 30% is observed then, which again indicates that further softening is happening in the cellulosic regions.

Key parameters controlling stiffness variability within trees: a multiscale experimental-numerical approach (Wagner et al., 2013)

Authored by Leopold Wagner, Thomas K. Bader, David Auty and Karin de Borst

Published in *Trees - Structure and Function*, 27(1):321–336, 2013

Microstructural properties of wood vary considerably within a tree. Knowledge of these properties and a better understanding of their relationship to the macroscopic mechanical performance of wood are crucial to optimize the yield and economic value of forest stocks. This holds particularly for the end-use requirements in engineering applications. In this study the microstructure-stiffness relationships of Scots pine are examined with a focus on the effects of the microstructural variability on the elastic properties of wood at different length scales. For this purpose, we have augmented microstructural data acquired using SilviScan-3™ (namely wood density, cell dimensions, earlywood and latewood proportion, microfibril angle) with local measurements of these quantities and of the chemical composition derived from wide-angle X-ray scattering, light microscopy, and thermogravimetric analysis, respectively. The stiffness properties were determined by means of ultrasonic tests at the clearwood scale and by means of nanoindentation at the cellwall scale. In addition, micro-mechanical modeling was applied to assess the causal relations between structural and mechanical properties and to complement the experimental investigations. Typical variability profiles of microstructural and mechanical properties are shown from pith to bark, across a single growth ring and from earlywood to latewood. The clear increase of the longitudinal stiffness as well

as the rather constant transverse stiffness from pith to bark could be explained by the variation in microfibril angle and wood density over the entire radial distance. The dependence of local cell wall stiffness on the local microfibril angle was also demonstrated. However, the local properties did not necessarily follow the trends observed at the macroscopic scale and exhibited only a weak relationship with the macroscopic mechanical properties. While the relationship between silvicultural practice and wood microstructure remains to be modeled using statistical techniques, the influence of microstructural properties on the macroscopic mechanical behavior of wood can now be described by a physical model. The knowledge gained by these investigations and the availability of a new micromechanical model, which allows transferring these findings to non-tested material, will be valuable for wood quality assessment and optimization in timber engineering.

3.1 Introduction

A major asset of wood is its natural origin. Particularly in times of increasing awareness of environmental problems and of rising ambitions regarding a carbon-neutral, sustainable consumption, there has been renewed interest in the use of wood and wood products. Wood proves suitable for a multitude of purposes, including the application to engineering structures. In this context, the natural origin of wood and its inherent high variability are also the biggest obstacles to its use at a wider scale. The main competitors for wood and wood products in the building sector – steel, concrete, and masonry – are all man-made materials, which can be designed for a specific purpose and produced in an industrial environment with only small fluctuations in their properties. Wood, however, has a large variability in the properties of the raw material, and it is impossible to tailor the material behavior to the requirements of the final application. Herein, we elucidate the variability of microstructural and micromechanical characteristics at different length scales and evaluate its effect on the practically relevant macroscopic behavior of wood. Improved knowledge about the factors controlling sawn timber performance will help to better select, categorize, and even breed trees for particular purposes. This will contribute to a more knowledge-based timber production, which has to date concentrated mainly on maximizing volume production. Traditionally, the selection and categorization of logs has commenced in the sawmill yard, after the trees have been harvested and without prior quality assessment. Thus, a large proportion of low-quality material is processed, with associated costs for the timber processing industry.

There is currently a growing interest in earlier preselection of forest material and, beyond that, in influencing the end-use properties by targeted silvicultural practices. Many previous studies have described the relationships between silvicultural practices – expressed for example in terms of rotation length, initial spacing, thinning, and fertilization – and final mechanical performance (see MacDonald and Hubert (2002) for a basic review). These relationships have been commonly expressed within a framework of statistical modeling. In such approaches, the stiffness and the strength of timber have been correlated with tree and stand-level information obtained from forest inven-

tories. The effect of silviculture and site characteristics on wood properties are then interpreted through their effect on tree growth (Eriksson et al., 2006; Mäkinen et al., 2009; Moore et al., 2009; Vihermaa, 2010; Auty, 2011). However, a purely statistical approach does not exploit available knowledge about the causal relations between silviculture and wood anatomy on the one hand and between wood anatomy and mechanical behavior on the other, which is available in forestry and mechanics. The incorporation of such information in models is expected to enhance the significance and the predictive capability of modeling approaches, since statistical correlations, which are subject to experimental scatter and uncertainties, could be replaced by strictly deterministic relations. Due to the hierarchical structure of wood, microstructural characteristics at several length scales determine the macroscopic behavior of the material. Known trends of these characteristics, e.g. from pith to bark or from earlywood to latewood, can be retrieved in trends of mechanical properties. We thus contribute to building the necessary scientific background and to enriching existing silvicultural models by mechanical expertise, using modern methods of material science and engineering. We measure important microstructural characteristics and stiffness properties from the macroscale (centimeter-range) down to the cell wall scale (micrometer-range) and assess the variability of these quantities within a tree at these different scales. We build on measurements of density, cell dimensions, earlywood, and latewood fractions, as well as (ring-averaged) microfibril angle by means of SilviScan-3™ (Auty et al., 2013) and add (localized) microfibril angle (MFA) measurements from Wide Angle X-ray Scattering (WAXS), and stiffness measurements in longitudinal, radial, and tangential direction measured using ultrasound as well as nanoindentation tests. In addition, we apply multiscale modeling to mathematically formulate the investigated microstructure-stiffness relationships (Suquet, 1987; Zaoui, 2002; Hofstetter et al., 2005; Bader et al., 2011b, 2012c). We pursue a purely deterministic approach to elucidate the causal relations between anatomical and mechanical properties. Once established, the models and relationships can be evaluated in a probabilistic context, considering random fluctuations of the independent model parameters. This is subject to future research activities.

Based on these investigations, this study has two main hierarchical aims:

1. To determine how anatomical and mechanical characteristics vary from pith to bark at different length scales and to identify the key parameters controlling the macroscopic mechanical performance of sawn timber in terms of its elastic properties. Investigations at multiple scales are conducted to identify length scale thresholds for microscopic measurements that influence macroscopic behavior of sawn timber.
2. To develop mathematical models linking anatomical and mechanical parameters. Given the physical basis of these models, they might be able to predict mechanical properties for non-tested tissues with higher accuracy than would be possible using only statistical correlations. Moreover, also special tissues, such as compression wood, can be treated, as long as their microstructural characteristics are completely known. This goes beyond the scope of statistical correlations, which

are usually only reliable within the range of microstructural characteristics represented in the tested samples.

Compared with existing investigations on the variability of anatomical and mechanical properties in a tree, the originality of our approach is characterized by (i) the concurrent assessment and joint evaluation of wood properties across several length scales on the same samples and (ii) the application of powerful micromechanical characterization techniques, which are not yet fully established in wood science, such as nanoindentation and multiscale modeling. As a long-term perspective, this may provide the basis for target values of microstructural properties and limits for their fluctuations to design silvicultural practices that fulfill wood quality requirements from a timber engineering point of view.

3.2 Methods

3.2.1 Samples

The samples originate from a large-scale quality survey of timber grown in Scotland and Northern England launched by the Forestry Commission Scotland. In order to incorporate a broad variation in growth conditions and, consequently, in microstructural and mechanical characteristics, samples from four different plantation sites across northeast Scotland were harvested. Discs at different heights were taken, from which radial sections were cut. The North-facing radial sections of the discs, cut at breast height, were used in this study (Figure 3.1a-b). Mean tree and stand characteristics for the different sites are shown in Table 3.1. All sampling sites were mature stands, aged between 73 and 100 years, growing at yield classes of between 6 and 10 m³ ha⁻¹ year⁻¹ at elevations between 10 and 200 m above sea level. Details on growth conditions and social classes, as well as further information can be found in (Auty, 2011).

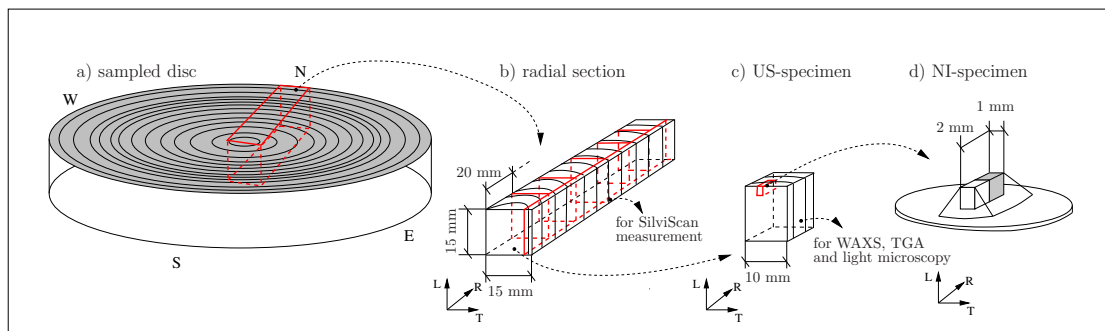


Figure 3.1: Sampling sequence; **a** Disc, cut at breast height; **b** Northfacing radial section, where strips for SilviScan-3TM measurements were cut from - the remaining side part was cut into 4-11 pieces; **c** Specimen for ultrasonic tests (US) and further use for nanoindentation (NI), wide-angle X-ray scattering (WAXS), thermogravimetric analysis (TGA) and light microscopy; **d** NI-specimen prepared from US test samples with 0° ring orientation

Table 3.1: Properties of the investigated trees; DBH...diameter at breast height, RN...number of annual rings

Sample	CU 88-1-N	TV 72-1-N	CM 100-1-N	AC 72-1-N
Site	Culbin	Tomvaich	Cloddymoss	Achneim
Height [m]	15.8	25.6	18.1	22.4
DBH [cm]	23	52	27.4	34.7
RN	73	98	57	63
Yield class	6	10	6	10
Elevation [m]	10	220	10	90

3.2.2 SilviScan-3™ Measurements

Microstructural characterization on the radial sections was performed using SilviScan-3™ technology (Evans, 1999, 2006) at Innventia AB, Stockholm. This instrument uses X-ray diffraction to measure the MFA, combined light microscopy and image analysis for assessing cell geometries, and X-ray densitometry to determine the wood density. The radial sections were soaked in acetone to remove extractives. Next, strips with cross sections of 2x7 mm² in tangential and longitudinal direction (LxT) were cut from the center of the radial sections, using a series of twin-blade circular saws (Figure 3.1b). Prior to the measurements these strips were again extracted (Soxhlet extraction in acetone) to remove any residual extractives and then conditioned at approximately 22°C and 40% relative humidity, resulting in a moisture content of the samples of approximately 7-8%. Mass density and wood cell dimensions were evaluated over intervals of 25 μm. The dataset was then split into earlywood (EW), transition wood (TW), and latewood (LW) for each annual ring, based on the minimum and maximum density of each individual annual ring. If the difference to the minimum density was smaller than 20% of the overall difference of maximum and minimum density, EW was assumed; if the density exceeded the minimum density by at least 80% of the overall difference, LW was assumed; otherwise TW was assumed (Auty, 2011). Following scanning, EW density, TW density, and LW density, as well as the overall mean density of each annual ring were available. The MFA was determined in 5 mm intervals. The sample was moved in the radial direction during exposure, giving average MFA over the given interval. Taking into account the sample dimensions and the range of radial dimensions of pine tracheids, intervals of 5 mm represents an average over approximately 10,000-20,000 tracheids.

3.2.3 Local Microfibril Angle Measurements

In addition to the measurements by SilviScan-3™, MFA was also analyzed by means of X-Ray diffraction (Wide Angle X-Ray Scattering, WAXS). This method provides a more localized measurement and was applied to determine MFA specific of earlywood (EW) and of latewood (LW). Thin sections of EW and LW with thicknesses of 50 and

70 μm , respectively, were cut from the annual rings on which nanoindentation tests had been carried out (Figure 3.1c). A Bruker Nanostar device (*Bruker ASX*, Madison, WI, USA), working with CuK_α radiation (wavelength 1.54 Å) was used. The diffraction patterns were collected with a 2D position sensitive detector at a distance of 13.2 cm from the sample during a 30 min period. Following Cave (1966), the 2D diffraction patterns were radially integrated between the scattering angles 2θ of 20.5° and 23° (002 Reflection), and the resulting intensities were plotted over the azimuthal angle (0° to 360°). The tangents were drawn to the flanks of each peak, and the angle between the intersections of these tangents with the baseline (commonly denoted as 'T-angle') was determined for each sample. Based on these data the MFA was estimated as 0.6 x T-angle (Meylan, 1967). Taking into account the size of the beam spot on the sample of 0.5 mm, as well as the thickness of the section, the resulting MFA represents a mean value over only 30-50 tracheids of either EW or LW. To acquire MFA profiles over one annual ring, with the purpose of studying the within-annual-ring variability, an optical method was applied. For this purpose the residual parts of the US-specimens have been taken, i.e. material adjacent to the NI-specimens (ring 17 of CM 100-1-N and ring 69 of TV 72-1-N, see Figure 3.1c). They were water saturated followed by harsh drying at 103°C. This procedure induces frequent checks in the S2 cell wall layer, which are oriented parallel to the cellulose microfibrils. Senft and Bendtsen (1985) proposed a method using iodine staining of thin sections to improve the visibility of the checks. However, since the checks were well visible in the radial sections, MFA could be determined directly without previous staining, using light microscopy techniques. The MFAs could not be determined directly on the NI-specimens, but were measured on an adjacent piece of wood from the same annual ring. Thus, the MFA profile is not directly related to the row of tracheids which was indented, but to an adjacent row of tracheids, shifted in tangential direction by <1 mm. The applied procedure did not result in equally spaced checks in the cell walls of the various specimens. While almost every cell exhibits visible checks in the S2 layer in ring 17 of CM 100-1-N, less checks were found in ring 69 of TV 72-1-N, even after repeated drying-wetting cycles.

3.2.4 Local Chemical Composition by Thermogravimetric Analysis

The local chemical composition of the cell wall material was studied by means of thermogravimetric analysis (TGA) at the positions where the MFA profiles were determined. In this method the weight of a material and its rate of change are determined during exposure to a controlled heating curve over time in a controlled atmosphere. TGA was performed using a TGA 250 (*TA Instruments*, New Castle, DE, USA) on 10 mg samples of ground wood (0.25 mm mesh) from specific annual rings (ring 17 of CM 100-1-N and ring 69 of TV 72-1-N). The analysis followed a method described by Grønli et al. (2002), delivering weight fractions of hemicelluloses, cellulose, lignin, and extractives. The presence of residual extractives in the ground TGA samples results from the incomplete removal of extractives during the first extraction procedure prior to the SilviScan-3™ measurements. Samples were again obtained from residual material of the specific annual rings, in particular those on which profiles of the indentation

modulus and of MFA across the annual ring had been determined (Figure 3.1c). The chemical composition of larger samples (as used for the ultrasonic tests) was estimated based on literature data (Fengel and Wegener, 2003).

3.2.5 Ultrasonic Testing

Ultrasonic (US) tests were carried out to determine the elastic stiffness in the principal material directions of wood, i.e. the longitudinal (L), the radial (R), and the tangential (T) direction. For these tests, the remaining side parts of each radial section after the removal of the SilviScan-3TM samples were cut into cuboidal samples with dimensions of 15x20x10 mm³ (LxRxT). This results in 4-11 cuboids, depending on the initial stem diameter (Figure 3.1b-c). They will be referred to as US-specimens in the following. Since the radial strips used for the US-specimens did not originate from the very center of the initial radial sections, the annual rings were not always aligned with the edges of the US-specimens. Thus, the measurements do not strictly represent the stiffnesses in radial and tangential directions, but show a slight deviation. The average angular deviation of the annual rings from the tangential direction of the cubes are listed in Table 3.2 for all US-specimens.

Table 3.2: Angular deviation of the annual ring orientation from tangential direction

Sample	Deviation angles of US-specimens [°]
CU 88-1-N	25/0/0/0
TV 72-1-N	30/15/0/0/0/0/0/0/0/15
CM 100-1-N	20/0/0/0/0/0
AC 72-1-N	30/15/0/0/0/0/10/10

Tests were performed at ambient conditions (20°C, 40% relative humidity) in transmission mode, using a pulser-receiver (PR 5077, *Panametrics Inc.*, Waltham, MA, USA), a digital oscilloscope (WaveRunner 62Xi, *Lecroy Corporation*, Chestnut Ridge, NY, USA), a pair of ultrasonic transducers for longitudinal pulses with a frequency of 100 kHz (*Panametrics Inc.*, Waltham, MA, USA), honey as coupling medium, and an auxiliary testing device to hold the transducers and the sample. A delay cylinder (aluminum alloy 5083, 20 mm height, resulting in 3.77 μ s delay time) was used to relocate the receiver signal from the receiver disturbances. A cellophane film was used to prevent the coupling medium from penetrating the microstructure of the wood samples, influencing the resulting elastic stiffness (for further details on the method and setup, see (Kohlhauser et al., 2009)). The oscilloscope provided the time of flight of the ultrasonic wave through the sample t_i ($i \dots$ L, R, T). In combination with the corresponding sample length l_i , the phase velocity in the material direction i , $v_i = l_i/t_i$, was determined. The elastic stiffness in this direction, $C_{i,EXP}$, is related to the phase velocity v_i by

$$C_{i,EXP} = \rho \times v_i^2 \quad (3.1)$$

with ρ being the average mass density of the specific US-specimen at ambient conditions (Bucur, 2006).

3.2.6 Nanoindentation Tests

Small samples (approx. $1.5 \times 2 \times 1 \text{ mm}^3$, LxRxT) for nanoindentation (NI) were cut from selected annual rings of the US-specimens with a 0° ring orientation (Figure 3.1d). Four (CU 88-1-N & AC 72-1-N) to five (TV 72-1-N & CM 100-1-N) NI specimens per stem were prepared, which resulted in 18 specimens. Prior to indentation, the NI-specimens were embedded in an epoxy resin (AGAR Low Viscosity Resin Kit, *Agar Scientific*, Essex, UK). The plane surface (RxT) was cut smooth with a microtome (Leica Ultracut, *Leica Microsystems*, Wetzlar, GER), equipped with a diamond knife (for further details see Konnerth et al. (2008)). Nanoindentation tests were performed at ambient conditions (20°C , 40 % relative humidity), using a TriboIndenter[®] (*Hysitron Inc.*, Minneapolis, MN, USA), equipped with a three-sided pyramidshaped tip (Berkovich type) in a load-controlled mode. Indentations were placed in the S2 cell wall layer of selected LW and EW tracheids. The correct positioning was verified by means of the scanning probe microscope (SPM) included in the TriboIndenter[®]. A five-step load function was applied, consisting of consecutive steps of loading, holding, and unloading (to 50% of the previous load level), reaching a final maximum load of $300 \mu\text{N}$. The section through an embedded wood cell exhibits multiple interfaces between the cell wall layers and between the cell wall and the embedding material. Jakes et al. (2009) proposed a critical distance from the center of the indent to the next interface or edge above which edge effects can be neglected. It is calculated as the square root of the projected contact area, A_C , times a material dependent factor (approx. 1.3 for polymers). In the present tests, the indent and the indentation parameters yielded a minimum distance of approximately $1 \mu\text{m}$, thus allowing to neglect edge effects. The resulting imprints in the cell walls were inspected through the SPM to check whether the remaining imprints lay within this distance to the nearest interface. The load-indentation depth curves were evaluated according to the method proposed by Oliver and Pharr (1992), relating the slope of the initial unloading path to the elastic material properties. This yields the indentation modulus M_{EXP} of the S2 cell wall layer of the selected cells. In addition, profiles of M_{EXP} in radial direction across annual rings were determined for two NI-specimens, with indents in every third cell. Thereby, only tangential cell walls were indented to avoid the influence of microfibril angle non-uniformities, which have been observed in the radial cell walls around bordered pits (Sedighi-Gilani et al., 2005).

3.2.7 Micromechanical Modeling

Micromechanical modeling based on homogenization strategies provides a way to quantitatively link microstructural characteristics to the macroscopic mechanical properties. We apply a model for softwood that was developed by the authors and has proven suitable for the prediction of elastic properties of softwood in a number of validation series and applications (Hofstetter et al., 2007; Bader et al., 2011b, 2012c). Homogenization methods allow the prediction of effective mechanical properties of microheterogeneous materials from their composition (components and their corresponding amounts), their morphology (shape, orientation, and distribution of the components), and mechanical information (stiffness and interactions of components). Depending on the mi-

microstructural morphology, different methods are appropriate. For example, continuum micromechanics suitably describes the effective behavior of composite materials with a random-like arrangement of the microstructural components, invoking solutions for matrix-inclusion problems. The unit cell method, on the other hand, is the best choice for representing materials with a regular microstructure that can be approximated by a periodically repeating unit.

Herein, we apply a micromechanical model for softwood stiffness, as documented in Bader et al. (2012c), which comprises three homogenization steps (Steps I-III in Figure 3.2), extended by a fourth homogenization step for the annual ring structure (Step IV in Figure 3.2a) as described by Bader et al. (2012c). The first three steps predict the effective stiffness properties of the polymer-matrix consisting of hemicellulose, lignin and water (Step Ia), of partially crystalline cellulose (Step Ib), and of the cell wall material (Step II), made up of the two effective materials introduced in Steps Ia and Ib. In Step III, effective stiffness properties of earlywood, transition wood, and latewood are predicted. The stiffnesses and interactions of the components are considered to be tissue-independent. The last step of the model (Step IV) accounts for the annual ring structure and combines earlywood, transition wood, and latewood with stiffnesses as determined in homogenization Step III. Steps Ia, Ib and II are performed using continuum micromechanical methods, while Step III employs the unit cell method, numerically analyzed by means of the commercial finite element code ABAQUS. In Step IV, laminate theory is applied to determine the effective behavior of the layered structure, delivering the sought stiffness properties of softwood at the macroscopic level. The discretization of an annual ring with a continuously changing density and microstructural properties into the different kinds of layers, i.e. earlywood, transition wood, and latewood, follows the conventions of SilviScan-3™.

The model is applied to calculate a sample-specific stiffness for each individual specimen from the mechanical tests. At the macroscopic level, the sample-specific clear wood stiffness is predicted for each US-specimen. At the cell wall level, the sample-specific cell wall stiffness of EW and LW is computed (using only Steps Ia, Ib and II) for each NI-specimen. An estimate of the indentation modulus obtained in the NI tests is calculated by applying anisotropic indentation theory (Jäger et al., 2011a), which allows direct comparison of predicted and measured indentation moduli. The model is also employed to predict the local cell wall stiffness properties across the two selected annual rings. This gives access to trends of mechanical properties across selected paths within a tree. The stiffness values that are predicted by the model are compared with the experimentally determined values at all length scales that have been investigated.

3.3 Results and Discussion

3.3.1 Experimental

Plots of the MFA and the overall mass density determined with SilviScan-3™, ρ_{SS} – both averaged over the length of the corresponding US-specimens – over the distance

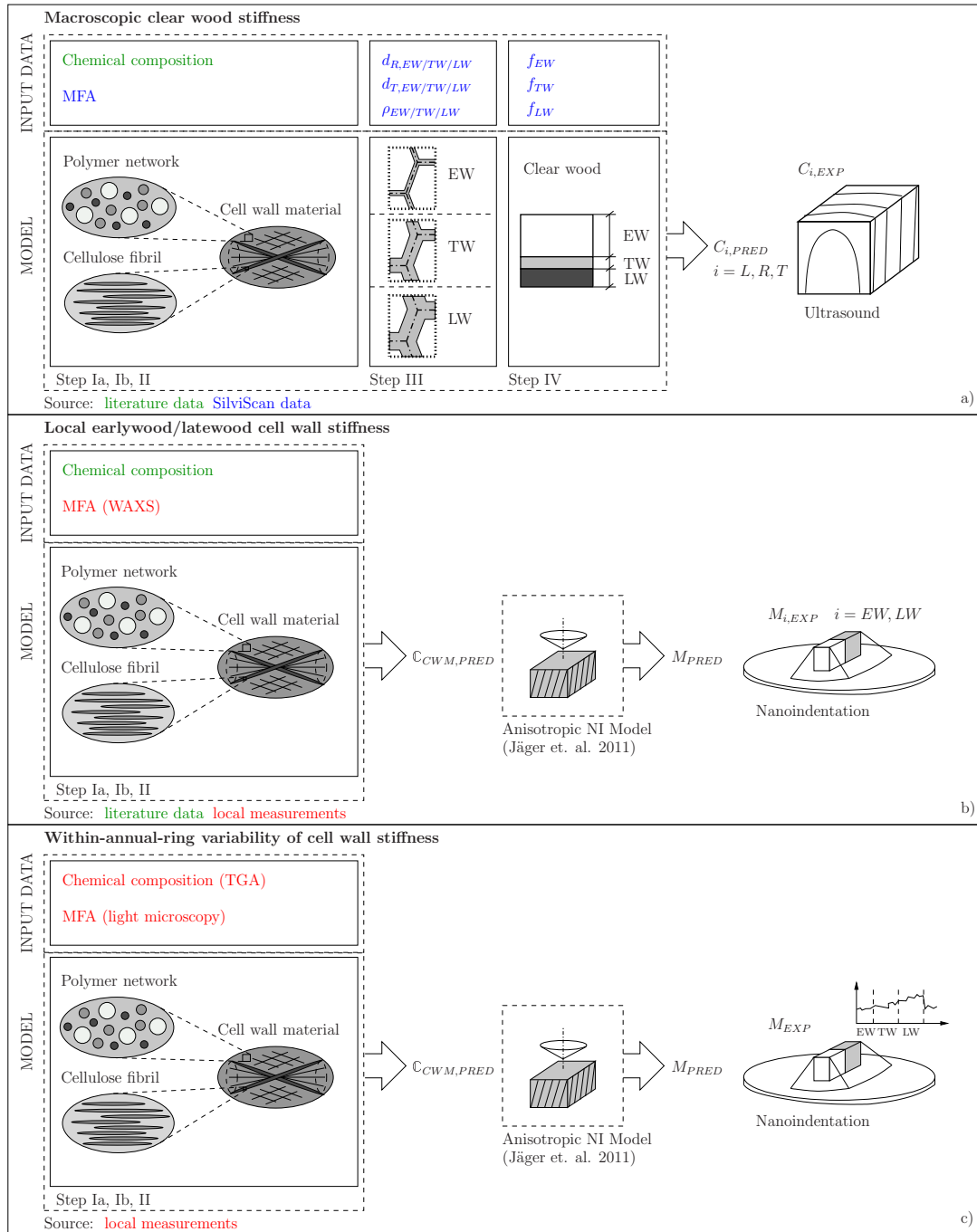


Figure 3.2: Micromechanical model for softwood stiffness and strategy for model predictions. a) Clear wood stiffness predicted using literature and SilviScan-3™ data (compared with results from ultrasonic tests); b) Local EW/LW cell wall stiffness predicted using literature data (chemical composition) and results from local measurements (MFA); c) Within-annual-ring variability of cell wall stiffness predicted using results from local measurements only – b) and c) both compared with results from nanoindentation tests

from the pith (see Figure 3.3, top figures) brings out well-known trends of decreasing MFA and increasing mass density from pith to bark. The MFAs decrease from 19.9-26.9° near the pith to 10.4-14.4° near the bark for the samples CU 88-1-N, TV 72-1-N, and AC 71-1-N. The mass densities of the samples from these three sites increase from 388-414 kg/m³ near the pith to 519-615 kg/m³ for the outermost US-specimens. The decrease of the MFA and the increase of the mass density are the most prominent in the first 15-20 annual rings (juvenile wood), while they both remain fairly constant throughout the rest of the stem (mature wood). The US-specimen from CM 100-1-N closest to the pith exhibits a relatively high mean MFA of 47.9° and a high mass density of 596 kg/m³, compared with the respective samples of the three other sites. This indicates the presence of compression wood near the pith in this specific tree. The longitudinal elastic stiffness, $C_{L,EXP}$, shows an increase from pith to bark by a factor of approximately two (see Figure 3.3, bottom figures). This increase can be explained by the simultaneous increase of the mass density and the decrease of the MFA over this stretch. These trends in MFA and mass density are well known (Cave and Walker, 1994; Zhang et al., 2007; Kollmann, 1982), and their relationship to the dynamic or the static longitudinal stiffness has been shown several times for various softwood species (Koponen et al., 2005; Alteyrac et al., 2006; Bader et al., 2012c). The strong curvature of the annual rings near the pith results in large angular deviations of the annual ring orientations from the edges of the US-specimens near the pith. It therefore does not allow for measurement of the transverse elastic stiffnesses $C_{R,EXP}$ and $C_{T,EXP}$ of these US-specimens. Rather, a mixed stiffness in the transverse direction is obtained, which is difficult to interpret. Nevertheless, these data points are included in the plots of $C_{R,EXP}$ and $C_{T,EXP}$ over the distance from the pith (see Figure 3.3, bottom figures) and show a higher $C_{T,EXP}$ than $C_{R,EXP}$, which contrasts the findings at larger distances from the pith. Except for the data from the innermost US-specimens, the $C_{R,EXP}$ and $C_{T,EXP}$ show only minor variations from pith to bark with no clear increase or decrease. This can be explained by the opposing effects of increasing mass density and decreasing MFA with respect to the transverse stiffness. The transverse elastic stiffness of wood has not been thoroughly investigated, and few data are available on the variation of transverse elastic stiffness from pith to bark (see Figure 3.3, bottom figures). Koponen et al. (2005) observed similar trends of rather constant radial and tangential stiffness over the stem cross section.

The indentation modulus is related to the local microstructure of the wood cell. It therefore crucially depends on the MFA of the wood cell which has been indented. The WAXS measurements provide such a local measure of the MFA of EW and of LW of the individual annual rings and are therefore used for the plots of M_{EXP} and MFA over the distance from the pith in Figure 3.4. Considering the huge number of individual cells along a radius of a cross-section, M_{EXP} and MFA only provide snapshots of local cell wall properties. Since the results refer to the local conditions and do not necessarily reflect trends on a larger length scale (i.e. radial variability from pith to bark) no trend lines are shown in Figure 3.4. M_{EXP} is in a range 14.1-22.5 GPa for LW and 12.3-22.6 GPa for EW tracheids. The typical coefficients of variation (CV = standard deviation divided by mean) of 6-25% result from indenting the tangential and radial cell walls in each tracheid. The presence of bordered pits just beneath the surface (Sedighi-

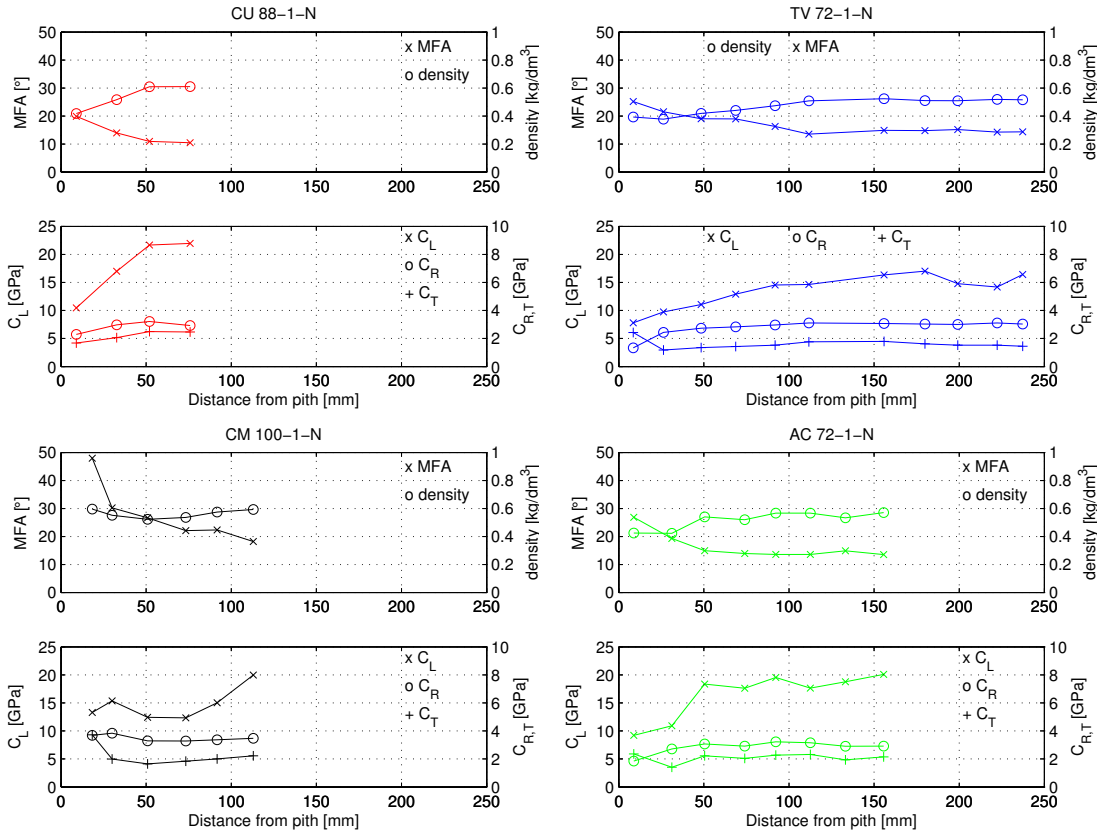


Figure 3.3: MFAs and mass densities (*top figures*) as well as elastic stiffnesses C_L , C_R , and C_T as measured in US-tests (*bottom figures*) from pith to bark

Gilani et al., 2005) of the NI-specimens and small sample tilts, which cannot be avoided (Konnerth et al., 2009), lead to these relatively large coefficients of variation.

The indentation moduli and the MFA show no common trend over the radial distance from pith to bark (3.4, bottom figures). While in three trees (CU 88-1-N, TV 72-1-N & CM 100-1-N) M_{EXP} seems to increase, a decrease of M_{EXP} from pith to bark is observed for the NI-specimens from AC 72-1-N. The MFA seems to increase in tree TV 72-1-N and to decrease in AC 72-1-N, while in CU 88-1-N and CM 100-1-N no overall trend is obvious. Despite the overall variability of M_{EXP} and MFA within a particular tree, the moduli and MFA obtained for EW and LW in the same ring closely follow each other and show similar trends across the different radial measurement positions in the individual trees. The MFA is consistently lower in LW than in EW for two trees (TV 72-1-N & AC 72-1-N), while the other two trees (CU 88-1-N & CM 100-1-N) do not show such patterns (see Figure 3.4, top figures). M_{EXP} in LW is not found to be consistently higher or lower than in EW at the level of individual trees. Half of the overall EW-LW couples show higher moduli in the LW, while the other half has higher moduli in EW. Given the local nature of the measured M_{EXP} , natural variations of the MFA at the length scale of a single cell, which are encountered on top of the

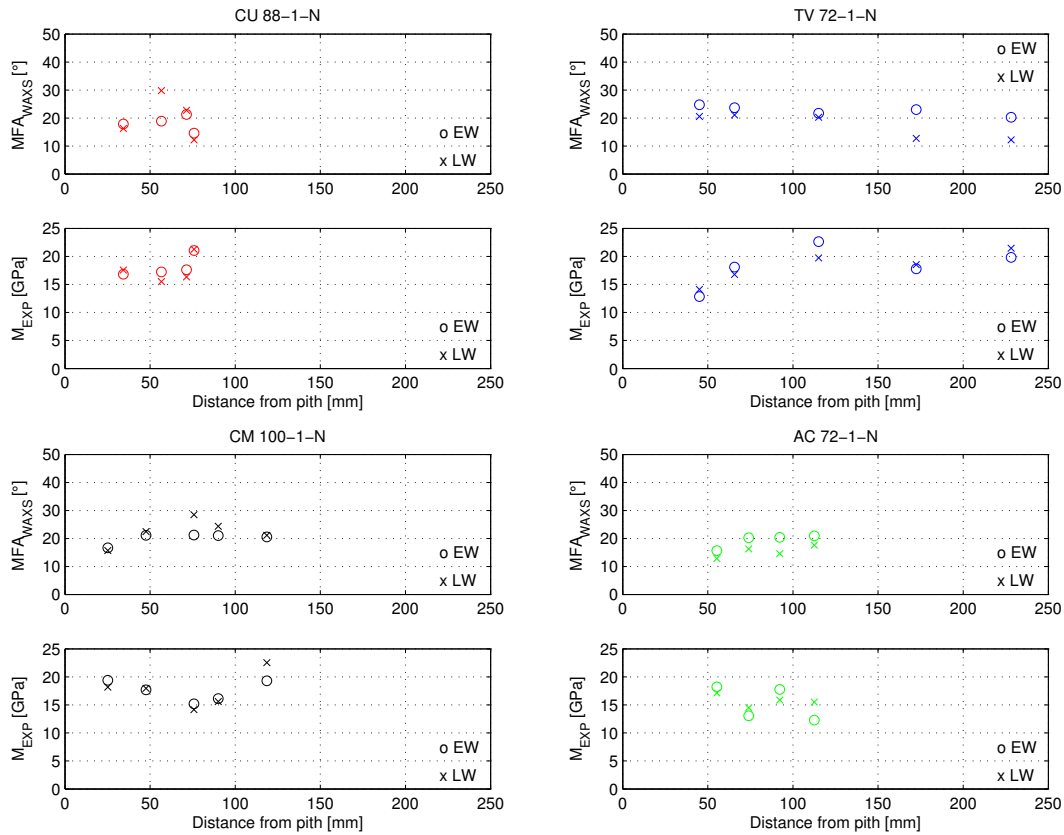


Figure 3.4: MFAs determined by WAXS (*top figures*) and M_{EXP} (*bottom figures*) over distance from pith

general trends from pith to bark and from EW to LW, dominate the resulting variability of M_{EXP} .

Table 3.3 shows a comparison of MFAs determined by SilviScan-3™ and by WAXS, respectively, for EW and LW of two specific annual rings (TV 72-1-N ring 69 and CM 100-1-N ring 17). Using the 5 mm averaging intervals, SilviScan-3™ is not able to resolve the differences between the MFAs in EW and LW, which are captured in the WAXS measurements. However, the pith-to-bark variability of the MFA and of the cell wall stiffness cannot be detected by the small number of WAXS measurements and nanoindentation tests since these influences are overridden by the within-annual-ring variability. In conclusion, variability of M_{EXP} is dominated by effects at annual ring scale.

The variability of the nanoindentation modulus M_{EXP} across a single annual ring is investigated further since the measurements of individual tracheids in one annual ring did not yield common trends from EW to LW. More indents are placed radially across single annual rings in the tangential cell walls for this purpose. The measured courses for ring 69 of TV 72-1-N and for ring 17 of CM 100-1-N are shown in Figure 3.5, where the mean values as well as bands around the means, indicating the standard deviations of the test results, are marked. Also the corresponding MFA profiles are shown there.

Table 3.3: Comparison of different MFA measurement methods at different length scales

NI-specimen	MFA [°]		
	SilviScan-3™	WAXS	Light microscopy min-max
TV 72-1-N ring 69 EW	15.0	23.0	14.9-27.2
TV 72-1-N ring 69 LW	15.0	12.7	8.1-23.4
CM 100-1-N ring 17 EW	26.7	22.5	21.1-28.9
CM 100-1-N ring 17 LW	27.5	21.1	18.1-23.6

For the NI-specimen prepared from ring 69 of TV 72-1-N, the cutting edges of the NI-specimen are shifted against the annual ring borders. Accordingly, M_{EXP} was rather measured in TW than in EW. However, since also the first tracheids of the following annual ring are included in this NI-specimen, the profiles of M_{EXP} and MFA can be drawn across the annual ring border between ring 69 and ring 70 of TV 72-1-N (included with negative values of distance in Figure 3.5), and the full variability across a stretch equal to the width of an annual ring can be analyzed.

Higher values of M_{EXP} in the LW than in the TW and EW are observed together with an increase of MFA from LW to EW in both specimens. Average values and standard deviations of M_{EXP} in the LW and TW of ring 69, and in the EW of ring 70 of TV 72-1-N, as well as from ring 17 of CM 100-1-N, are shown in Table 3.4 as well as the corresponding MFAs.

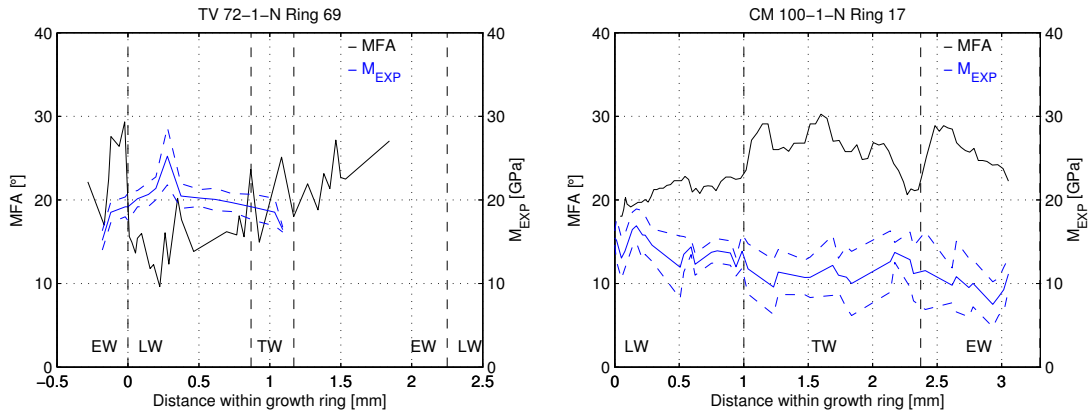


Figure 3.5: Profiles of M_{EXP} and MFA over the radial extension of one annual ring; 0 mm represents the position of the first LW tracheid; widths of LW, TW, and EW resulting from the definitions used by SilviScan-3™; dashed lines correspond to standard deviations of M_{EXP}

In concordance with the present results, Bader et al. (2012c) also reported higher M_{EXP} in individual LW tracheids than in EW tracheids of single annual rings of Norway spruce and Common yew, accompanied by higher MFAs in the EW in both species. However, a distinct local variability of M_{EXP} and MFA, especially in the EW, is evident

Table 3.4: Variability of the indentation moduli M_{EXP} and MFA of the two annual rings, investigated in detail

Sample	M_{EXP} [GPa]	MFA [°]
TV 72-1-N		
Ring 69		
TW	18.02±1.40	21.2±5.5
LW	20.99±1.79	15.0±2.6
Ring 70		
EW	18.01±1.92	24.2±4.5
CM 100-1-N		
Ring 17		
EW	9.79±1.29	26.0±1.9
TW	11.43±1.17	25.9±2.5
LW	14.24±1.46	21.0±1.4

on top of the trends from LW to EW. Low variability in LW was also found by Wimmer and Lucas (1997). These authors reported no significant change in the indentation modulus over the first 12 consecutive LW tracheids in Norway spruce ($\sim 250 \mu\text{m}$), which might indicate only slight changes of MFA within this region (not reported). Eder et al. (2009) performed micro-tensile tests on individual tracheids across one annual ring of Norway spruce and found a small increase of the cell wall stiffness from EW to LW, also accompanied by an increasing MFA from LW to EW.

The series of indents across one annual ring enables studying trends in the cell wall stiffness across the ring from EW to LW. The trend of decreasing M_{EXP} from LW to EW is more pronounced in ring 69 of TV 72-1-N than in ring 17 of CM 100-1-N, while both rings show similar differences in the MFA. This might be a consequence of the overall higher MFA level of ring 17 of CM 100-1-N, as the influence of MFA on the indentation modulus decreases with increasing MFA (Jäger et al., 2011a). As previously noted, CM 100-1-N might contain compression wood near the pith, as indicated by a high MFA and a high density. The dependence of M_{EXP} on the MFA also becomes obvious when comparing local maxima and minima of these two characteristics. A maximum M_{EXP} of 25.24 ± 3.44 GPa is measured in ring 69 of TV 72-1-N, accompanied by the minimum MFA of 9.6° roughly at the same position. In ring 17 of CM 100-1-N, several such couples of high MFA and low M_{EXP} can be observed, e.g. at distances of approximately 0.5 mm and approximately 2.25 mm, respectively, with moduli and MFA of 11.95 ± 3.73 GPa and 22.8° (0.5 mm) and 13.72 ± 1.20 GPa and 20.6° (2.25 mm). The fact that the local peaks of M_{EXP} do not perfectly match with the local minima of the MFA can be explained from differences in the methods for measuring the MFA profiles.

3.3.2 Micromechanical Modeling

Using the experimentally determined microstructural and micromechanical data, structure-function relationships can be described. However, the need for a comprehensive exper-

imental data set restricts the exploration to tested cases and prevents a more general, in-depth investigation of the effect of selected microstructural characteristics on the mechanical performance. This can be accomplished by the micromechanical model introduced previously. The calculated stiffnesses, predicted by means of the collected microstructural/micromechanical data set, as well as the comparison with the experimental results, are summarized in the following:

First, the macroscopic stiffness of each US-specimen is predicted (Figure 3.2a). The prediction relies, on one hand, on the typical chemical composition of Scots pine, specified in the literature (Fengel and Wegener (2003), see Table 3.5) and, on the other hand, on the detailed microstructural characteristics for EW, TW, and LW, determined by SilviScan-3™. The SilviScan-3™ data used for the model evaluations are the radial and tangential wood cell diameters, d_R and d_T , yielding an aspect ratio of the cells (specifying the shape of the unit cell in homogenization Step III), as well as the volume fractions of EW, TW, and LW, $f_{EW/TW/LW}$, and the corresponding mass densities, $\rho_{EW/TW/LW}$. The data are averaged according to the EW-TW-LW classification made by SilviScan-3™ for each US-specimen, i.e. average values of d_R , d_T , f , and ρ are calculated for EW, TW, and LW of each US-specimen, respectively (see Table 3.6). Following the MFA determination by SilviScan-3™, an average MFA of each specific US-specimen is used for the model predictions, ignoring the EW-TW-LW structure. The moisture content is set to 8%, corresponding to the ambient conditions during the SilviScan-3™ measurements and the US tests.

Table 3.5: Literature data on chemical composition (values in brackets refer to composition used for model predictions of clear wood stiffness) and chemical composition of the two annual rings investigated by TGA, used for the model predictions of the within-annual-ring variability of the cell wall stiffness; Cel...cellulose, hemcel...hemicellulose, lig...lignin, ext...extractives; ^afrom Fengel and Wegener (2003)

Sample	Cel [%]	Hemcel [%]	Lig [%]	Ext [%]
Scots pine ^a	41.9-52.2 (47.5)	12.1-30.4 (24.0)	26.3-31.4 (25.0)	<6.0 (3.5)
TV 72-1-N ring 69	46.9	27.1	23.5	2.5
CM 100-1-N ring 17	42.4	29.8	23.8	4.0

The resulting stiffnesses $C_{i,PRED}$, $i = L, R, T$, are lower than those experimentally determined, $C_{i,EXP}$. For example, model predictions for the longitudinal direction range from 7.3 to 13.4 GPa for tree TV 72-1-N compared with corresponding experimental values from 7.8 to 16.4 GPa. The difference between the elastic stiffness obtained from ultrasonic tests and the quasi-static stiffness, predicted by the micromechanical model, stems from the dynamic nature of the ultrasonic test (Bucur, 2006). To enable a comparison of trends of the predicted elastic stiffnesses with those determined experimentally from pith to bark, the predicted and the experimentally determined stiffness values for each tree are related to the particular results of the US-specimens at the greatest distance from the pith. These relative stiffnesses, $rel. C_{i,PRED}$ and $rel. C_{i,EXP}$

are plotted over the distance from the pith in Figure 3.6. In longitudinal direction the predicted relative stiffness profile follows the experimental curve except for the last US-specimens near the pith. The model predictions are calculated using literature data on the chemical composition, which is kept constant across the stem diameter. The lower experimental values near the pith in CU 88-1-N, TV 72-1-N, and AC 72-1-N indicate lower cellulose contents of these specimens. The formation of heartwood, resulting in an altered chemical composition due to the incorporation of extractives, is not accounted for by a constant chemical composition. Considering a lower volume fraction of cellulose near the pith would decrease the elastic stiffness predicted by the model.

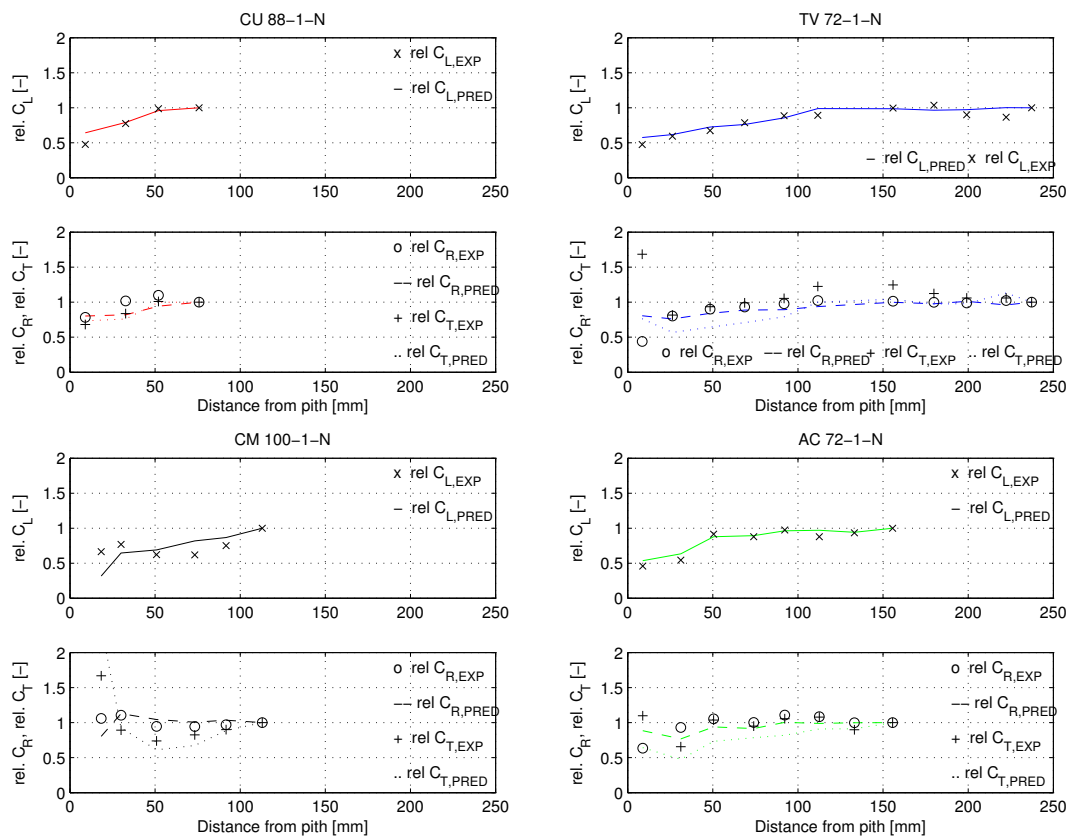


Figure 3.6: Relative changes of $C_{L,EXP/PRED}$ (top figures) as well as $C_{R,EXP/PRED}$ and $C_{T,EXP/PRED}$ (bottom figures) from pith to bark; related to outermost US-specimen beneath the bark

Also in the tangential and radial directions the predicted trends of the relative stiffness agree well with those determined experimentally, again with the exception of the innermost US-specimens. For these US-specimens the US tests no longer yield proper radial and tangential elastic stiffness values, but rather a mixed transversal stiffness. The overall variability of the experimentally determined elastic stiffness in the transverse direction is small, which is also reflected by the model predictions. Tree CM 100-1-N is an exception, as the trend of the predicted elastic stiffness in the longitudinal direction from pith to bark does not agree with the experimentally determined values. The cal-

culated values of *rel. C_{L,PRED}* are too high in the outer part of the stem, while they decrease too rapidly near the pith, possibly a consequence of the assumption of a constant chemical composition.

Predictions of the nanoindentation moduli M_{PRED} are calculated for EW and LW of each investigated annual ring. They are obtained from the same material properties and microstructural (Table 3.6) and compositional data (Table 3.5) also used as input for the macroscopic model predictions, with exception of the MFAs. For this characteristic, EW/LW-specific values are employed instead of the SilviScan-3™ data, as determined by WAXS (see Figure 3.4). The M_{PRED} and M_{EXP} are plotted over the distance from the pith in Figure 3.7. Again, the points are not connected, considering that the values are just snapshots of the local properties and do not necessarily represent pith-to-bark trends. M_{PRED} followed closely the local MFA in EW or LW of each specific annual ring. Accordingly, the same tendencies of a higher M_{EXP} in LW than in EW for trees TV 72-1-N and AC 72-1-N and no consistent trends in trees CU 88-1-N and CM 100-1-N are observed, similar to the local MFAs (see Figure 3.7).

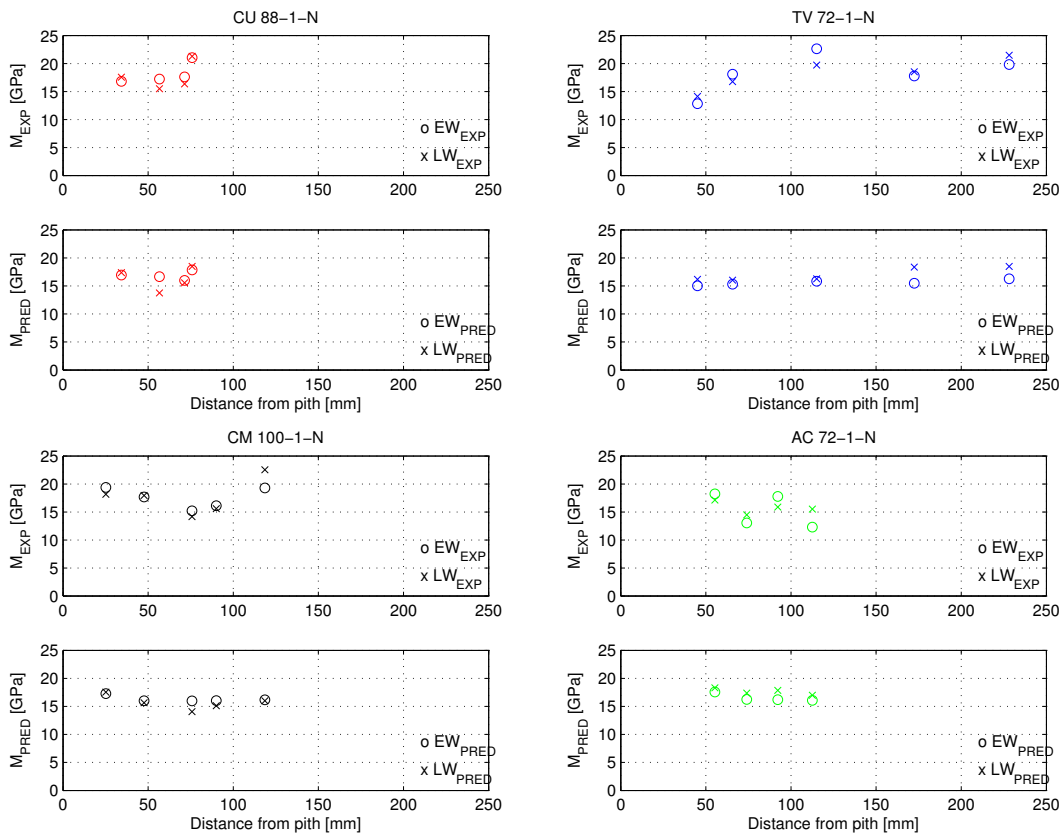


Figure 3.7: M_{EXP} (top figures) as well as M_{PRED} (bottom figures) over distance from pith

Model predictions for profiles of the indentation modulus across selected annual rings are derived based on the MFAs determined by light microscopy and the average chemical composition across that specific annual ring from the thermogravimetric

analysis (Figure 3.2c). The chemical composition of these annual rings shows a lower cellulose content in CM 100-1-N ring 17 (42.4%) compared with TV 72-1-N ring 69 (46.9%, see also Table 3.5).

The variation of M_{PRED} closely follows the variation of the MFA from LW to EW within the annual ring, i.e. high MFAs are always accompanied by low M_{PRED} (Figure 3.8). The higher cellulose content in ring 69 of TV 72-1-N results in overall higher values for M_{PRED} in this sample, compared with those for ring 18 of CM 100-1-N. The difference in M_{EXP} between the two investigated annual rings at positions with the same MFA is higher than the difference of the corresponding M_{PRED} , which might indicate a dominant influence of the local chemical composition, mainly of cellulose content.

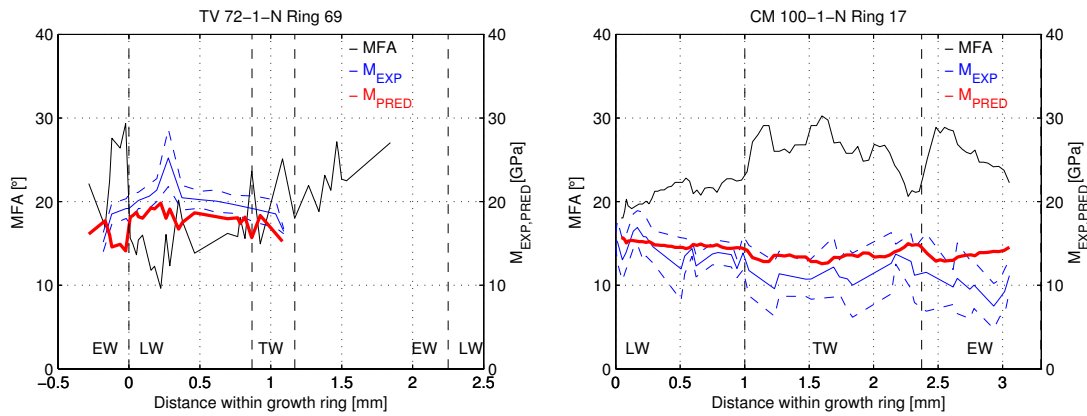


Figure 3.8: Profiles of predicted indentation modulus M_{PRED} across the annual ring; 0 mm represents the position of the first LW tracheid; widths of LW, TW, and EW resulting from the definitions used by SilviScan-3™; dashed lines correspond to standard deviations of M_{EXP}

On the whole, the model proves to deliver reasonable predictions for the stiffness values of wood across the length scales of its hierarchical structure. It confirms that wood anatomy and wood physics are correctly represented by the model, and in sufficient detail. The model thus constitutes a powerful tool for in-depth analysis of wood-stiffness relationships without the need for extensive further experimental test series.

3.4 Conclusions

We investigated structure-function relationships of wood at different length scales based on a comprehensive experimental program for determination of structural and mechanical characteristics. This has enabled us to identify the controlling microstructural properties at different length scales and to assess the effect of their variability on the macroscopic mechanical performance of wood. At the cell wall scale, the microfibril angle (MFA) acts as the dominant microstructural influence parameter on the stiffness, next to the chemical composition. The MFA is a highly variable quantity, and subject to

variability at various length scales. Within a single cell, the vicinity of pits and the location of the measuring spot in either a radial or tangential cell wall may affect the orientation of the cellulose microfibrils. This local variability is the most pronounced. Across a growth ring, a slight decrease of MFA from earlywood to latewood was observed, which was, however, considerably less pronounced than the local fluctuations. Finally, at the macroscopic scale, the MFA drops at small distances from the pith at the transition from juvenile wood to mature wood. Out of all the variations at the different length scales, this is the only variability that takes effect on the macroscopic stiffness of wood. For this reason it is important to average microstructural characteristics, such as the MFA, over sufficiently large sampling lengths to end up with macroscopically relevant parameters. A sampling length of 5 mm for MFA, used during the SilviScan-3™ measurements, turned out to be suitable for such an investigation, while refined measurements using X-ray diffraction delivered too detailed information.

Next to the pith-to-bark trend of the MFA, density is the second main parameter that influences the stiffness at the macroscopic scale. The density increases from pith to bark, as does the longitudinal stiffness. In the transverse direction, the effects of increasing density and decreasing MFA cancel each other and result in a rather constant transverse stiffness within a radial cut. Suitable sampling lengths now depend on the intended application and, as a consequence, on the size of the wooden members of interest. Moreover, the mechanical loading mode must be considered. The mean density over the entire cross-section might be sufficiently accurate to properly describe the longitudinal stiffness of wooden members of characteristic sizes similar to the cross sectional diameter. Under straining in transverse direction, the series connection of regions (juvenile vs. mature wood) and of layers (earlywood vs. latewood) with different microstructural characteristics and, thus, stiffnesses, calls for a more refined approach. Latewood/ earlywood differences and the radial density profile are then crucial for the transverse stiffness, also of larger-sized samples.

Multiscale modeling has proved capable of predicting macroscopic stiffness and of reproducing the proper trends at different length scales, taking the natural variability of microstructural characteristics across the scales into account. It is thus a powerful tool for improving the choice and further processing of timber resources.

Recommendations for silviculture also require the modeling of the influence of silvicultural strategies on (micro-)structural characteristics of the wood anatomy, e.g. mass density and MFA. However, target values for the microstructural characteristics and limits for their fluctuations can already be set, based on the knowledge of their effect on the macroscopic mechanical performance. For example, the model can be employed to determine the size of the juvenile core to be excluded from structural applications. It can link (given) microstructural parameters of the juvenile wood region to the expectable mechanical properties and, from there, provide estimates for the distances from the pith in the particular tree at which threshold values of these properties are reached. In collaboration with forestry, many further applications of the developed model and the in-depth insights gathered into this study are foreseen.

Table 3.6: Microstructural characteristics used for macroscopic stiffness predictions

US-spec.	MFA [°]	d_R [μm]		d_T [μm]		f [-]		ρ [kg/m^3]		ρ_{SS} [kg/m^3]				
		EW	TW	LW	TW	EW	LW	EW	TW	EW	LW	EW	LW	
CU 88-1-N														
1	19.9	34.2	28.8	22.4	31.3	25.8	25.7	0.35	0.58	0.07	325	413	638	399
2	14.0	34.2	30.4	22.7	28.4	28.0	27.0	0.51	0.27	0.22	364	579	811	520
3	10.9	35.0	29.6	21.8	29.2	28.4	28.4	0.53	0.19	0.27	420	695	945	617
4	10.4	35.1	32.2	23.3	30.6	30.3	29.6	0.56	0.22	0.22	458	775	859	615
TV 72-1-N														
1	25.1	30.9	28.7	22.5	26.0	26.4	25.7	0.43	0.45	0.12	301	435	532	388
2	21.5	32.7	32.0	24.7	26.1	26.7	25.7	0.45	0.35	0.20	278	418	545	380
3	19.0	33.0	31.1	24.6	26.5	26.3	25.1	0.46	0.36	0.18	307	454	577	410
4	19.0	34.6	31.8	26.3	27.1	26.4	26.8	0.47	0.31	0.23	324	515	603	446
5	16.3	36.0	32.3	26.0	28.2	28.1	27.3	0.50	0.22	0.28	318	573	682	476
6	13.5	37.2	32.1	25.5	29.5	28.6	28.0	0.49	0.24	0.28	326	623	727	506
7	14.9	35.2	31.7	25.7	28.3	27.9	27.7	0.43	0.26	0.32	348	578	727	528
8	14.8	36.0	31.8	25.7	27.6	27.4	27.2	0.44	0.27	0.29	337	564	717	510
9	15.2	36.5	32.9	25.9	27.3	27.1	26.6	0.43	0.31	0.27	337	557	727	509
10	14.2	36.4	30.8	24.5	28.4	27.8	27.7	0.58	0.20	0.23	347	729	775	519
11	14.4	37.8	33.3	25.5	28.3	28.0	26.6	0.50	0.25	0.25	331	661	755	519
CM 100-1-N														
1	47.9	26.3	24.5	26.0	34.0	33.9	34.0	0.09	0.50	0.41	439	439	821	596
2	30.2	34.0	30.5	24.9	25.9	26.0	26.0	0.41	0.30	0.30	429	487	784	551
3	26.6	37.0	35.3	29.4	27.4	27.8	26.5	0.33	0.32	0.35	357	495	704	523
4	22.1	38.2	35.1	26.2	28.0	28.0	26.6	0.47	0.24	0.29	376	571	765	536
5	22.3	37.8	35.6	25.6	29.5	29.1	28.3	0.47	0.25	0.29	391	642	817	575
6	18.2	37.9	35.6	25.6	29.9	29.4	29.8	0.45	0.24	0.31	401	566	887	593
AC 72-1-N														
1	26.9	30.3	28.3	23.1	26.5	27.2	26.5	0.37	0.50	0.13	345	421	581	414
2	19.3	32.7	29.7	23.6	26.6	27.7	26.6	0.65	0.20	0.15	335	492	707	422
3	14.9	32.9	29.4	24.1	27.8	27.5	27.8	0.52	0.22	0.27	384	593	784	535
4	13.9	33.5	30.6	22.9	27.6	28.4	27.6	0.51	0.25	0.24	375	507	833	519
5	13.6	34.0	31.5	24.5	27.7	29.2	27.7	0.48	0.24	0.28	385	607	839	564
6	13.6	34.5	33.1	24.2	28.4	29.3	28.4	0.47	0.26	0.27	380	554	895	566
7	14.9	35.1	32.1	25.0	28.4	28.0	28.4	0.51	0.29	0.20	388	557	876	535
8	13.5	35.8	32.3	24.5	29.7	30.1	29.7	0.52	0.25	0.23	387	639	911	571

Appendix 1: Multiscale Micromechanical Model for Softwood Stiffness

In the following the mathematical description of the multiscale micromechanical model for softwood stiffness, according to Figure 3.2, is presented. Due to its predominant role, only the S2 cell wall layer is considered for softwood stiffness. Steps Ia, Ib and II are performed using the framework of continuum micromechanics, Step III is performed by unit cell analysis and Step IV uses laminate theory.

Converting Mass Fractions to Volume Fractions

The conversion of the mass fractions of the constituents of wood to volume fractions requires the respective mass densities of the 'universal' phases (i.e. crystalline cellulose, amorphous cellulose, hemicelluloses, lignin, water and extractives) ρ_r , $r \in [\text{crycel}, \text{amocel}, \text{hemcel}, \text{lig}, \text{H}_2\text{O}, \text{ext}]$, which are reported in literature (see e.g. Fengel and Wegener (2003) or Appendix A in Hofstetter et al. (2005)). To determine the crystalline part of cellulose mass fraction the degree of crystallinity with respect to volume C_r is converted into a degree of crystallinity with respect to mass C_{r_w} according to Hofstetter et al. (2005):

$$C_{r_w} = \frac{C_r}{C_r + (1 - C_r)\rho_{\text{amocel}}/\rho_{\text{crycel}}}, \quad (3.2)$$

with ρ_{amocel} and ρ_{crycel} as mass densities of amorphous (amocel) and crystalline cellulose (crycel). The respective mass fractions read as

$$w_{\text{crycel}} = C_{r_w}w_C \text{ and } w_{\text{amocel}} = (1 - C_{r_w})w_C. \quad (3.3)$$

The mass fractions are given with respect to the dry cell wall. To calculate the mass fractions with respect to the wet cell wall, each mass fraction w_r is divided by $(1 + u)$, with u as the respective moisture content. The volume fractions f_r are calculated from

$$f_r = w_r \frac{\rho_{\text{CWM}}}{\rho_r}, \quad (3.4)$$

with the cell wall mass density ρ_{CWM}

$$\rho_{\text{CWM}} = \left(\sum_r \frac{w_r}{\rho_r} \right)^{-1}, \quad r \in [\text{crycel}, \text{amocel}, \text{hemcel}, \text{lig}, \text{H}_2\text{O}, \text{ext}]. \quad (3.5)$$

Stiffness of the 'Universal' Phases

The stiffness tensors of the above mentioned 'universal' phases have to be defined. Using the respective bulk and shear moduli k_r and μ_r of the isotropic phases (amorphous cellulose, hemicelluloses, lignin, water and extractives, see Table 3.7), the stiffness tensor \mathbb{C}_r of the phase r reads as

$$\mathbb{C}_r = 2\mu_r \mathbb{J} + 3k_r \mathbb{K}, \quad (3.6)$$

with $\mathbb{J} = 1/3 \mathbf{I} \otimes \mathbf{I}$ and $\mathbb{K} = \mathbb{I} - \mathbb{J}$ as the volumetric and deviatoric parts of the 4th order unity tensor \mathbb{I} with components $I_{ijkl} = 1/2(\delta_{ik}\delta_{jl} + \delta_{il}\delta_{jk})$. For crystalline cellulose, the stiffness tensor $\mathbb{C}_{crystal}$ is defined by its components $C_{crystal,ijkl}$ (Table 3.7).

Table 3.7: 'Universal' phase properties; a...Eichhorn and Young (2001); b...Cousins (1978); c...Cousins (1976); d...Tashiro and Kobayashi (1991)

phase	material behavior	bulk modulus k [GPa]	shear modulus μ [GPa]	ref.
amorphous cellulose	isotropic	$k_{amocel} = 5.56$	$\mu_{amocel} = 1.85$	a
hemicellulose	isotropic	$k_{hemcel} = 8.89$	$\mu_{hemcel} = 2.20$	b
lignin	isotropic	$k_{lig} = 5.0$	$\mu_{lig} = 2.2$	c
water	isotropic	$k_{H2O} = 2.3$	$\mu_{H2O} = 0.0$	
extractives	isotropic	$k_{ext} = 3.0$	$\mu_{ext} = 0.05$	
stiffness tensor components C_{ijkl} [GPa]				
crystalline cellulose	transeversely isotropic	$C_{crystal,1111} = 34.86$ $C_{crystal,3333} = 167.79$ $C_{crystal,1313} = 5.81$	$C_{crystal,1122} = 0$ $C_{crystal,2233} = 0$	d

Continuum Micromechanical Model for the Stiffness of the S2 Cell Wall Layer

The mathematical description of Step Ia, Step Ib and Step II of the multiscale micromechanical model for the prediction of the S2 cell wall layer stiffness are presented.

The stiffness of the polymer network (poly) – Step Ia – is calculated by means of a Self-Consistent scheme. The homogenized stiffness tensor of the polymer network \mathbb{C}_{poly}^{hom} reads as

$$\mathbb{C}_{poly}^{hom} = \sum_r f_{r,poly} \mathbb{C}_r : [\mathbb{I} + \mathbb{P}_r^0 : (\mathbb{C}_r - \mathbb{C}_{poly}^{hom})]^{-1} :$$

$$\left\{ \sum_s f_{s,poly} [\mathbb{I} + \mathbb{P}_s^0 : (\mathbb{C}_s - \mathbb{C}_{poly}^{hom})]^{-1} \right\}^{-1},$$

$$r, s \in [\text{lig}, \text{hemcel}, \text{H2O}, \text{ext}], \quad (3.7)$$

with the respective volume fractions $f_{r|s,poly}$ (Table 3.5)

$$f_{r|s,poly} = \frac{f_{r|s}}{\sum_{r|s} f_{r|s}}, \quad r, s \in [\text{lig}, \text{hemcel}, \text{H2O}, \text{ext}]. \quad (3.8)$$

The stiffness of the cellulose fibril (CF) – Step Ib – is calculated by means of the Mori-Tanaka method. The homogenized stiffness tensor of the cellulose fibril \mathbb{C}_{CF}^{hom} reads as

$$\mathbb{C}_{CF}^{hom} = \sum_r f_{r,CF} \mathbb{C}_r : \left[\mathbb{I} + \mathbb{P}_r^0 : (\mathbb{C}_r - \mathbb{C}_{amocel}) \right]^{-1} : \left\{ \sum_s f_{s,CF} \left[\mathbb{I} + \mathbb{P}_s^0 : (\mathbb{C}_s - \mathbb{C}_{amocel}) \right]^{-1} \right\}^{-1},$$

$$r, s \in [\text{amocel}, \text{crycel}]. \quad (3.9)$$

with the respective volume fractions $f_{r|s,CF}$ (Table 3.5)

$$f_{r|s,CF} = \frac{f_{r|s}}{\sum_{r|s} f_{r|s}}, \quad r, s \in [\text{amocel}, \text{crycel}]. \quad (3.10)$$

The stiffness of the cell wall material (CWM) – Step II – is calculated by means of Mori-Tanaka method. Since the cellulose fibrils are helically wound, the cellulose needs to be subdivided into an infinite amount of subphases which are characterized by the same latitudinal angle $\bar{\theta}$ – the microfibril angle (MFA) – but different longitudinal angles φ , so that the homogenized stiffness tensor of the cell wall material \mathbb{C}_{CWM}^{hom} reads as (Bader et al., 2011b)

$$\mathbb{C}_{CWM}^{hom} = \left\{ f_{poly} \mathbb{C}_{poly} + f_{CF} \frac{1}{2\pi} \int_{\varphi=0}^{2\pi} \mathbb{C}_{CF}(\varphi, \bar{\Theta}) : \left[\mathbb{I} + \mathbb{P}_{cyl}^{poly}(\varphi, \bar{\Theta}) : (\mathbb{C}_{CF}(\varphi, \bar{\Theta}) - \mathbb{C}_{poly}) \right]^{-1} d\varphi \right\} : \left\{ f_{poly} \mathbb{I} + f_{CF} \frac{1}{2\pi} \int_{\varphi=0}^{2\pi} \left[\mathbb{I} + \mathbb{P}_{cyl}^{poly}(\varphi, \bar{\Theta}) : (\mathbb{C}_{CF}(\varphi, \bar{\Theta}) - \mathbb{C}_{poly}) \right]^{-1} d\varphi \right\}^{-1}, \quad (3.11)$$

with $\bar{\Theta}$ as the microfibril angle (MFA) and the respective volume fractions f_{CF}

$$f_{CF} = f_{amocel} + f_{crycel}; f_{poly} = f_{lig} + f_{hemcel} + f_{H2O} + f_{ext}. \quad (3.12)$$

To calculate estimates of the anisotropic indentation modulus M_{PRED} of the S2 layer, the elastic constants of the cell wall material are required without considering the helically wound arrangement of the cellulose fibrils. Therefore Step II was altered accordingly

$$\mathbb{C}_{CWM}^{hom} = \left\{ f_{poly} \mathbb{C}_{poly} + f_{CF} \mathbb{C}_{CF} : \left[\mathbb{I} + \mathbb{P}_{cyl}^{poly} : (\mathbb{C}_{CF} - \mathbb{C}_{poly}) \right]^{-1} \right\} : \left\{ f_{poly} \mathbb{I} + f_{CF} \left[\mathbb{I} + \mathbb{P}_{cyl}^{poly} : (\mathbb{C}_{CF} - \mathbb{C}_{poly}) \right]^{-1} \right\}^{-1}. \quad (3.13)$$

The stiffness of the cell wall material (Equation 3.13) is on the one hand used to calculate an estimate of the indentation modulus, according to Jäger et al. (2011a), using the five elastic constants of the transverse isotropic stiffness tensor and the MFA. On the other hand the estimated cell wall stiffness, according to Equation 3.11, is used to predict the stiffness of the EW, TW and LW layers by means of the unit cell method (Step III – Figure 3.2). Numerical unit cells are built from the respective cell geometries in each sample and the cell walls are assigned the estimated cell wall stiffness \mathbb{C}_{CWM}^{hom} from Step II (Bader et al., 2012c). The unit cell is analyzed by means of the commercial Finite Element code ABAQUS, yielding the effective stiffness of EW, TW and LW.

Laminate Theory to estimate Softwood Stiffness

The effective stiffness of softwood is calculated from the stiffnesses of EW, TW and LW, taking advantage of the layered arrangement within the annual rings (Step IV – Figure 3.2). Therefore laminate theory is applied, as documented in Bader et al. (2012c), with the extension from two (i.e. EW and LW) to three layers (i.e. EW, TW and LW). According to El Omri et al. (2000) using a tensorial decomposition in plane and antiplane components of the stresses and strains

$$\begin{bmatrix} \sigma_P \\ \sigma_A \end{bmatrix} = \begin{bmatrix} \mathbf{c}_{PP,i} & \mathbf{c}_{PA,i} \\ \mathbf{c}_{AP,i} & \mathbf{c}_{AA,i} \end{bmatrix} : \begin{bmatrix} \epsilon_P \\ \epsilon_A \end{bmatrix}, \quad (3.14)$$

with plane and antiplane components of the stress tensor, exemplarily written in compressed matrix notation as

$$\sigma_P = \begin{bmatrix} \sigma_{RR} & \sigma_{LL} & \sqrt{2}\sigma_{LR} \end{bmatrix}, \quad (3.15)$$

$$\sigma_A = \begin{bmatrix} \sigma_{TT} & \sqrt{2}\sigma_{TL} & \sqrt{2}\sigma_{RT} \end{bmatrix}. \quad (3.16)$$

Within an RVE of softwood, composed of EW, TW and LW layers in parallel arrangement, antiplane stress and plane strain components are uniform

$$\epsilon_{P,EW} = \epsilon_{P,TW} = \epsilon_{P,LW} = E_{P,SW}, \quad (3.17)$$

$$\sigma_{A,EW} = \sigma_{A,TW} = \sigma_{A,LW} = \Sigma_{A,SW}. \quad (3.18)$$

After partly inverting the constitutive relation (Equation 3.14) to a form where only constant stress and strain components stand on the left side of the equation

$$\begin{bmatrix} \sigma_P \\ \epsilon_A \end{bmatrix} = \begin{bmatrix} \mathbf{c}_{PP,i} - \mathbf{c}_{PA,i} : \mathbf{c}_{AA,i}^{-1} : \mathbf{c}_{AP,i} & \mathbf{c}_{PA,i} : \mathbf{c}_{AA,i}^{-1} \\ -\mathbf{c}_{AA,i}^{-1} \mathbf{c}_{AP,i} & \mathbf{c}_{AA,i}^{-1} \end{bmatrix} : \begin{bmatrix} E_P \\ \Sigma_A \end{bmatrix}. \quad (3.19)$$

Terms on the right side can be averaged over the constituents of the laminate. Reassembling Equation 3.19 to the form of Equation 3.14, yields the homogenized stiffness tensor of softwood \mathbb{C}_{SW}^{hom} , the plane and antiplane components reading as

$$\mathbf{C}_{PP,SW}^{hom} = \langle \mathbf{c}_{PP,i} - \mathbf{c}_{PA,i} : \mathbf{c}_{AA,i}^{-1} : \mathbf{c}_{AP,i} \rangle_V - \langle \mathbf{c}_{PA,i} : \mathbf{c}_{AA,i}^{-1} \rangle_V : \langle \mathbf{c}_{AA,i}^{-1} \rangle_V^{-1} : \langle \mathbf{c}_{AA,i}^{-1} \mathbf{c}_{AP,i} \rangle_V, \quad (3.20)$$

$$\mathbf{C}_{PA,SW}^{hom} = \langle \mathbf{c}_{PA,i} : \mathbf{c}_{AA,i}^{-1} \rangle_V : \langle \mathbf{c}_{AA,i}^{-1} \rangle_V^{-1}, \quad (3.21)$$

$$\mathbf{C}_{AP,SW}^{hom} = -\langle \mathbf{c}_{AA,i}^{-1} \rangle_V^{-1} : \langle \mathbf{c}_{AA,i}^{-1} \mathbf{c}_{AP,i} \rangle_V, \quad (3.22)$$

$$\mathbf{C}_{AA,SW}^{hom} = \langle \mathbf{c}_{AA,i}^{-1} \rangle_V^{-1}, \quad (3.23)$$

where $\langle (\cdot) \rangle_V$ denotes the volume average of (\cdot) over the RVE of softwood, discretized by the volume-weighted sum over the three layers

$$\langle (\cdot) \rangle_V = \sum_i f_i(\cdot), \quad i \in [\text{EW}, \text{TW}, \text{LW}]. \quad (3.24)$$

A Combined View on Composition, Molecular Structure and Micromechanics of Fungal Degraded Softwood (Wagner et al., 2014c)

Authored by Leopold Wagner, Thomas K. Bader, Thomas Ters, Karin Fackler
and Karin de Borst

Revisions *Holzforschung*, 2014
submitted to

Fungal decay results in alterations of the composition, the microstructure and the mechanical properties of wood cell walls. Structure-function relationships are started to be understood for sound wood, but it is still unclear whether these relationships hold also for deteriorated wood cell walls. To investigate these relationships, selected annual rings of fungal deteriorated Scots pine sapwood are analyzed for their composition, microstructure and micromechanical properties. The dataset was acquired separately for earlywood and latewood in the S2 cell wall layer and the middle lamella and analyzed by means of multivariate data analysis. Links between altered mechanical properties of wood cell walls (stiffness and hardness) and altered cell wall composition and microstructure could be established. Increased stiffness and hardness of the middle lamella was correlated to the degradation of pectins. In the S2 layer, altered hardness and stiffness were linked to degradation of hemicelluloses and alterations of lignin during fungal decay.

4.1 Introduction

Fungal degradation is among the greatest hazards for the integrity of standing trees as well as of interior and exterior wood constructions. Wood rotting fungi can be categorized according to their mode of degradation into brown rot (BR) and white rot (WR) (Eriksson et al., 1990; Schwarze, 2007). Selective WR fungi first cleave lignin to get access and then decompose the polysaccharide components in the wood cell wall by means of enzymatic substances, while simultaneous WR fungi degrade all wood polymers simultaneously (Blanchette, 1984). BR fungi directly utilize the more nutritious wood polysaccharides, while modifying lignin only to a limited extent (Goodell, 2003). Insight into the different degradation strategies of the fungi and their effects on the wood composition, micro- and ultrastructure has been gained by a variety of methods, including infrared spectroscopy (Pandey and Pitman, 2003; Fackler et al., 2010), wet chemical methods (Kirk and Highley, 1973; Kirk, 1975) as well as X-ray scattering (Lee et al., 2007b; Howell et al., 2009). Studies on the mechanical effects of fungal decay were almost exclusively concerned with linking the overall stiffness and strength losses at the macroscale and the altered wood composition after fungal decay (Wilcox, 1978; Winandy and Morrell, 1993).

The mechanical properties of wood are determined by its inherent hierarchical microstructure. The levels of organization have been identified as the growth ring structure consisting of earlywood (EW) and latewood (LW), the multi-layered wood cell walls with its individual cell wall layers, comprising a primary cell wall (P-layer), three secondary cell wall layers (S1, S2 & S3-layer) and individual wood cells are connected by the middle lamella (ML) (Page, 1976; Fengel and Wegener, 2003). For the macroscopic behavior of wood, the S2 layer – consisting of cellulose fibrils which are oriented in parallel, inclined to the cell axis by the microfibril angle (MFA) and are embedded in a hemicellulose-lignin matrix – and the ML – mainly consisting of a lignified pectin network – play a major role. Establishing causal relationships between changes of composition, ultrastructure, and microstructure and the macroscopic mechanical properties of wood is difficult, as the occurring mass loss often masks the effects of changing composition and microstructure in the remaining wood cell walls. It is thus necessary to step down the hierarchical organization of wood to the cell wall scale, where the fungal degradation actually occurs, in order to enhance the current understanding of the mechanical consequences of fungal degradation.

Local measurement of composition and microstructural features at the cell wall scale, individually for EW and LW, requires experimental methods that are capable of delivering results on small amounts of materials and on samples with small dimensions. Herein we apply Fourier transform infrared spectroscopy (FT-IR) for detecting changes in wood composition and cell wall ultrastructure, X-ray scattering to analyze the wood cell wall microstructure, and nanoindentation (NI) to probe the stiffness of the wood cell wall (Wimmer and Lucas, 1997; Tze et al., 2007; Wagner et al., 2014a).

Herein, the results of investigations on Scots pine sapwood after degradation by either BR or WR up to mass losses of 10% are presented. For selected annual rings, the

S2 cell wall layers and middle lamellae (ML) were analyzed by means of the methods mentioned before, separately for EW and LW. In addition, wet chemical methods are applied in order to determine the chemical composition of the samples, again separately for EW and LW.

The big size of the data set suggests application of multivariate data analysis in order to unravel interrelations between mechanical, microstructural and compositional quantities. Principle component analysis (PCA) is performed on the compositional, microstructural, and micromechanical data. Moreover, partial least square regression (PLSR) analysis is applied to establish a link between mechanical properties of wood cell walls with their chemical composition and molecular structure. This is achieved by regression of FT-IR spectra, containing information on both chemistry and molecular structure, with mechanical properties of the wood cell walls. All multivariate data analysis is carried out separately for EW and LW as well.

4.2 Experimental Procedures

4.2.1 Materials

Investigations are carried out on Scots pine (*Pinus sylvestris* L.) sapwood samples degraded by one fungus causing WR (*Trametes versicolor* [L.] Lloyd) and one fungus causing BR (*Gloeophyllum trabeum* [Pers.] Murril). The samples were degraded in laboratory tests at conditions, specified by EN 113 (1996). The macroscopic changes of their physicochemical and mechanical properties have been reported in detail elsewhere (Alfredsen et al., 2012; Bader et al., 2012a,b). Herein, we focus on changes at the cell wall scale. We consider early stages of degradation only, characterized by mass losses of approximately 1%, 5%, and 10%. This corresponds to two, four, and six weeks of BR (BR2, BR4 & BR6) and to two, six, and twelve weeks of WR (WR2, WR6 & WR12), respectively. Moreover two undegraded reference samples (REF) were analyzed. Cuboidal samples of approximately 20x20x15 mm³ in longitudinal, radial, and tangential direction (LxRxT) were used (Figure 4.1a). First, a 2x20x15 mm³ (LxRxT) slice was cut from the initial cuboids (Figure 4.1b), from which later the NI samples were cut. The remaining blocks (Figure 4.1d) were re-impregnated with deionized water and subsequently tangential thin sections of the EW (200 μm) and LW (150 μm) of the selected annual rings were sliced by means of a sliding microtome (Figure 4.1e). They were used for the FT-IR tests, the X-ray scattering, and the wet chemical analyses. The thin sections did not contain enough material for determination of the lignin content. The residual material (Figure 4.1f) was used for this purpose and was carefully separated into EW and LW for this purpose. For the NI tests, small specimens of approximately 2x2x1.5 mm³ (LxRxT) were cut the aforementioned slices from the same annual rings, from which the thin sections had been prepared (Figure 4.1c). These specimens were then embedded in an epoxy resin (AGAR Low Viscosity Resin Kit, *Agar Scientific*, Essex, UK). The plane surface was cut smooth with a microtome (Leica Ultracut, *Leica Microsystems*, Wetzlar, GER), equipped with a diamond knife.

In total, two REF samples, three BR2 samples, four BR4, BR6, and WR2 samples, and five WR6 and WR12 samples were analyzed, each separated for EW and LW (i.e. 27 EW and 27 LW samples, see Table 4.1).

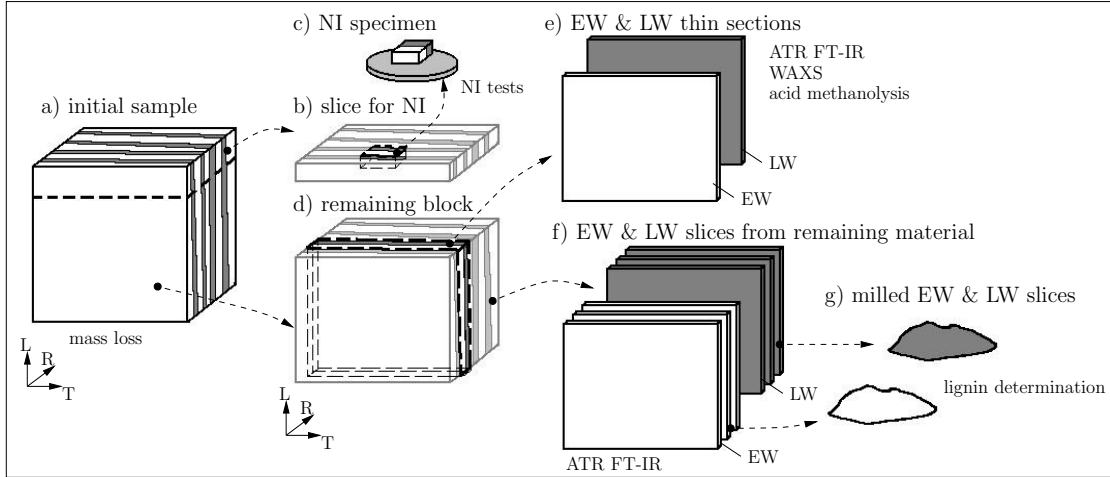


Figure 4.1: Sample preparation; EW – earlywood, LW – latewood, NI – Nanoindentation, ATR FT-IR – Attenuated Total Reflectance Fourier Transform Infrared Spectroscopy, WAXS – Wide Angle X-ray Scattering

4.2.2 Methods Outline

The experimental program was carried out in the following order (cf. Figure 4.1): First attenuated total reflectance Fourier transform infrared spectroscopy (ATR FT-IR) was performed on the thin sections and on the slices of the residual material, followed by wide angle X-ray scattering (WAXS) of the thin sections. Afterwards these sections were used for the determination of the contents of hemicelluloses and pectic sugars by acid methanolysis. Due to the small amount of available sample, the lignin content could not be determined from the thin sections, but it was rather measured from the residual material. In order to link these measurements to the lignin contents of the thin sections, the ATR FT-IR spectra recorded on both the thin sections and the residual material were used, as described in detail later. Besides that, nanoindentation tests were performed on material containing both EW and LW of the investigated annual rings. Finally, multivariate data analysis methods were applied to analyze relationships between micromechanical properties and composition and microstructure.

4.2.3 Attenuated Total Reflectance Fourier Transform Infrared Spectroscopy (ATR FT-IR)

For the ATR FT-IR investigations, the thin sections and the slices of the residual material were freeze-dried. The measurements were carried out using a Bruker Vertex 70 FT infrared spectrometer (*Bruker Optics*, Ettlingen, Germany) equipped with a Platinum

diamond ATR unit and a room temperature DLaTGS detector. At least 4 surface spectra from each thin section and 10 surface spectra from each residual slice were recorded between 4000 cm^{-1} and 600 cm^{-1} (spectral resolution 4 cm^{-1} , zero-filling factor 2). 32 scans per spectrum were averaged to increase the signal-to-noise ratio. 2nd derivatives of the ATR FT-IR spectra were calculated according to Savitzky and Golay (1964) applying 17 smoothing points and 2nd order polynomial fit, followed by a standard normal variate (SNV) normalization in the spectral range between 1855 cm^{-1} and 600 cm^{-1} . This combination of data treatments reduces adverse baseline effects, as well as differences in spectral data, caused by different sample densities and varying pressures applied to the samples during the measurement.

4.2.4 Wide Angle X-Ray Scattering (WAXS)

WAXS was applied to determine the MFA and the crystallinity of the thin sections (Figure 4.1e). A Bruker Nanostar device (*Bruker ASX*, Madison, WI, USA), working with $\text{CuK}\alpha$ radiation (wavelength 1.54 \AA), was used. The scattering patterns were collected using a 2D position sensitive detector at a distance of 4.85 cm from the sample for 1 h. To determine the MFA, the integrated intensity of the 200 reflection was plotted over the azimuthal angle. The MFA was evaluated from the resulting intensity curves according to Meylan (1967).

To determine the degree of crystallinity of the sample (Cr), the obtained 2D scattering patterns were integrated over azimuthal angles from 0° to 360° , and the resulting intensities were plotted versus the scattering angle 2Θ . Cr was estimated by the method according to Segal et al. (1959), using the intensities of the 200 peak (I_{200}) and the local intensity minimum between the 200 and 110 peaks (I_{AM}), representing the amorphous part of the scattering pattern. Cr was then calculated as:

$$Cr = \frac{(I_{200} - I_{AM})}{I_{200}} * 100[\%]. \quad (4.1)$$

4.2.5 Wet Chemical Analysis

The contents of hemicelluloses and pectic sugars as well as of accessible glucose from glucomannan and non-crystalline regions of cellulose were determined according to Sundberg et al. (1996), using 10 mg of material from each thin section. The analysis yielded contents of accessible glucan (acc. glu), arabinan (ara), galactan (gal), galacturonan (galA), glucuronan (glcA), mannan (man), rhamnan (rha) and xylan (xyl), specified in relation to their anhydro forms. As mentioned earlier, the thin sections did not contain enough material to determine the lignin content according to TAPPI Test Method T222 (1988). Therefore, the slices of EW or LW cut from the residual material, from which already ATR FT-IR spectra had been recorded, were used for this purpose. The EW and LW slices were milled separately to a particle size of $80\text{ }\mu\text{m}$. After freeze-drying, the milled wood samples were extracted with a Buechi Speed Extractor (*Buechi Labortechnik AG*, Flawil, SUI), using an acetone/water mixture (95/5 vol.) at 110°C in

four static cycles of 15 min each. Thereafter the total lignin content of each slice, based on non-extracted wood, was determined according to TAPPI Test Method T222 (1988). These results were related to the (yet unknown) lignin contents of the thin sections via the ATR FT-IR spectra, recorded on both materials. In particular, cross-validated PLSR models were built, using the lignin content from the wet chemical analysis as y-variable and 10 averaged pre-treated ATR FT-IR spectra, recorded on the slices of residual material before milling, extraction and determination of the lignin content, in the range from 1855 - 600 cm^{-1} as x-variables (Figure 4.1).

4.2.6 Nanoindentation

The NI tests were performed using a TriboIndenter[®] (*Hysitron Inc.*, Minneapolis, MN, USA) in a load controlled mode. The sample chamber was climatized at $20 \pm 2^\circ\text{C}$ / $60 \pm 2\%$ relative humidity, using a RH-200 Relative Humidity Generator (*L&C Science and Technology*, Hialeah, FL, USA). A three-sided pyramid-shaped tip (Berkovich type) was used. Indents were placed in the S2 layer of selected EW and LW tracheids as well as in the middle lamellae (ML) in the cell corners in EW and LW. Positioning was verified using the built-in scanning probe microscope (SPM). A three step load function, consisting of consecutive loading, holding and unloading (to 50% of the previous load level) steps was applied, reaching a maximum load P_{max} of 150 μN . The cross section of an embedded wood cell exhibits multiple interfaces between cell wall layers and between the cell wall and the embedding material. According to Jakes et al. (2009), potential edge effects can be neglected if the center of an indent shows a distance to the next interface or edge of at least the square root of the contact area, $A_C^{0.5}$, times a material dependent factor of approx. 1.3 (for polymers), resulting in approximately 1 μm for the setup used herein. The resulting imprints in the cell walls were all inspected via the SPM. Indents not fulfilling the required distance were discarded. The load-indentation depth curves were evaluated according to the Oliver and Pharr (1992) method. The slope of the initial unloading (= initial unloading stiffness S) is related to the elastic material properties and thus used to determine the indentation modulus M from:

$$M = \frac{\sqrt{\pi}}{2} * \frac{S}{\sqrt{A_C}}, \quad (4.2)$$

where A_C denotes the contact area. The indentation hardness H follows from dividing the maximum force P_{max} by A_C .

4.2.7 Multivariate Data Analysis (MVA)

MVA allows the reduction of multidimensional data, data visualization, and separating effects due to degradation from noise due to measurement inaccuracies. Herein, principle component analysis (PCA) was performed on the directly determined compositional data (contents of lignin, hemicelluloses, and pectic sugars), the mechanical properties of the cell walls (M and H of the S2 layer and the ML), as well as Cr , using the Unscrambler (v9.7, *Camo Software AS.*, Oslo, NOR). PCA is a method of data

analysis that is well suited to show correlations of variables in a multivariate data set. It allows identifying similarities and dissimilarities among the investigated samples and to visualise sample characteristics. Moreover, it facilitates finding correlations between variables in a descriptive way in scores and loadings plots of only a few – here, only two – dimensions. PCA further allows for the quick differentiation between more and less important variables in the data set. Here PCA was applied to visualize the processes during fungal degradation of wood at cell wall scale, to assign the most important changes during WR and BR degradation, and to find relations between the obtained chemical and microstructural data and the mechanical cell wall properties. To normalize the scale of the data, variables were weighted by dividing them by the standard deviation (SD) within the respective variable, and mean centering was applied before PCA. PCAs were performed separately for EW and LW.

To analyze possible relations between micromechanical and spectroscopic data, PLSR analysis was performed using the micromechanical data, i.e. indentation moduli of the S2 layer and the ML, as y-variables and the individual ATR FT-IR spectra, recorded from the surfaces of the thin sections, as x-variables, using the Unscrambler (v9.7). EW and LW, as well as BR and WR wood were analyzed separately. Here PLSR was employed to find relations between spectroscopic data and micromechanical properties. Only cross-validated calibration models will be shown and discussed. Preliminary regression models were calculated from the pretreated spectral data. These models were further processed using Martens' uncertainty test (Westad and Martens, 2000) to extract the most important spectral variables to describe the correlation.

4.3 Results and Discussion

4.3.1 Wet Chemical Analysis

The results of the wet chemical analyses in terms of EW and LW specific composition of the individual samples are summarized in Table 4.1 in the Appendix. Trends in the composition of the remaining cell wall material upon BR and WR decay are obvious only for some cell wall components. Basically, these trends are the same for both EW and LW. The lignin content decreases during WR and increases during BR degradation. The contents of the pectic sugars (i.e. ara, gal, galA & rha) and of xyl decrease, while the contents of glcA and of acc. glu increase. For the other components, no clear trends during WR and BR decay can be seen from the raw data (Table 4.1). Since the deteriorated material has not been characterized before fungal decay, some observed changes might partly also originate from differences between these samples and the reference samples already existing before degradation.

4.3.2 Wide Angle X-Ray Scattering

X-Ray scattering yielded the MFA and C_r of all samples. By far most of the samples show lower MFAs in LW than in EW, with MFAs of 7.0-14.1° in LW and of 9.6-24.9° in

EW (Table 4.2). However, the results for some samples deviate from this trend, e.g. with MFAs of 23.4° in LW and 17.7° in EW. This might be a consequence of using samples only 150-200 μm thick (in R-direction) for determining the MFA. Such thin samples are susceptible to the random variability of the MFA, on top of the known EW-to-LW trends (Wagner et al., 2013).

Average C_r values of the reference samples amount to 32.2% in EW and to 31.9% in LW (Table 4.2). In general, C_r shows hardly any changes during WR (31.4% and 31.8% for EW and LW, respectively), while a slightly decreasing C_r can be observed during BR (28.8% and 29.8% for EW and LW, respectively; Table 4.2). The observed changes of C_r might be a consequence of the fungal decay (Howell et al., 2009). It cannot be ruled out that some changes also emerged during the kiln drying (Bhuiyan et al., 2000), which was performed after the degradation according to EN 113 (1996). Again, some variability might also originate from pre-existing differences of the C_r between the samples before degradation.

4.3.3 Nanoindentation

The indentation modulus M and the indentation hardness H were determined separately for the S2 cell wall layers in EW and LW (M_{S2EW} & M_{S2LW} and H_{S2EW} & H_{S2LW}) and for the middle lamellae (M_{ML} & H_{ML}). The S2 cell wall layer exhibits anisotropic elastic material properties (Page, 1976; Salmén and Burgert, 2009), having its main material axis aligned with the cellulose microfibrils. Thus M_{S2EW} and M_{S2LW} depend on the inclination of the cellulose microfibrils to the indentation direction, i.e. on the MFA (Jäger et al., 2011a,b). Accordingly, the variation of MFA among the samples prevents from directly comparing M_{S2EW} and M_{S2LW} at different degradation stages. The correction of the measurement results for the (known) MFA of each sample would require knowledge of the indentation moduli in several directions (Jäger et al., 2011b). Yet, samples with similar MFA can be compared, revealing a tendency of higher M_{S2EW} in the WR samples. H of the S2 cell wall layer has been experimentally shown to not depend on the MFA (Tze et al., 2007). This allows assessing the changes of H_{S2EW} and H_{S2LW} during degradation on the basis of the test results (Table 4.2). H_{S2EW} and H_{S2LW} show small increases from 0.38 ± 0.00 GPa and 0.39 ± 0.01 GPa for the REF samples to 0.41 ± 0.03 GPa (+8.5%) and 0.42 ± 0.01 GPa (+10.1%) for BR6 samples in EW and LW. According values for the EW and LW of the WR12 samples are 0.42 ± 0.03 GPa (+11.1%) and 0.41 ± 0.02 GPa (+6.0%) (Table 4.2).

The ML shows isotropic material behavior, enabling to directly compare results obtained for different samples and to study the evolution of both M_{ML} and H_{ML} over the degradation time for this layer. M_{ML} increases from 6.44 ± 0.31 GPa for the REF samples to 7.30 ± 0.35 GPa (+13.4%) for BR6 and to 7.37 ± 0.35 GPa (+14.4%) for WR12. H_{ML} also increases from 0.32 ± 0.03 GPa for the REF samples to 0.38 ± 0.01 GPa (+17.8%) for BR6 and to 0.35 ± 0.01 GPa (+10.0%) for WR12 (Table 4.2).

4.3.4 Multivariate Analysis of Micromechanical, Microstructural and Chemical Characteristics

The scores plot of the PCA of EW (Figure 4.2a) shows that a major share of data variance (PC1=34%) can be allocated to degradation time and, thus, to mass loss. Non-degraded samples and samples in early degradation stages (REF, BR2, WR2 and WR6) have lower PC1 scores than samples in later degradation stages. BR4 and BR6 samples have the highest scores on PC1. PC2 (21%) separates samples according to their degradation type, with WR samples having positive PC2 scores and most BR samples and non-degraded samples showing negative PC2 scores. Degraded samples separate from non-degraded ones, except for one sample in early BR and early WR. This shows that this multivariate approach using chemical and micromechanical properties of wood is well suited to identify early wood degradation processes. The remaining PCs (45%) represent the variability of the raw material in terms of composition and microstructure (e.g. MFA).

PC loadings (Figure 4.2c) allow for characterizing wood degradation processes, because they show differences in variables related to chemistry, molecular structure and micromechanical properties of the S2 cell wall layer and the middle lamella. Here, variables (i.e. sample characteristics) with negative loadings on PC1 are more pronounced in non-degraded samples, while variables with positive loadings on PC1 are related to degradation. Variables with positive loadings on PC2 are higher in WR degraded samples, while those with negative loadings are higher in BR degraded samples.

Variables in EW, where trends could be seen already in the raw data (Tables 4.1-4.2), showed the highest loadings on PC1 and PC2. In EW these characteristics are higher contents of pectic sugars (gal, ara, rha and galA) and xyl and higher Cr in non-degraded condition, as well as higher contents of acc. glu and higher M_{ML} , H_{ML} and, to a lesser extent, also H_{S2EW} in degraded conditions. Less important characteristics of degradation, i.e. PC1 close to 0, were changes in man content and M_{S2EW} . Due to increasing lignin content during BR and decreasing lignin content in WR, lignin has also PC1 close to 0. Most obvious on PC2 were the positive loadings of M_{S2EW} and H_{S2EW} , revealing higher values after WR degradation, and the negative PC2 loadings of lignin content, indicating higher lignin content after BR decay. However, as mentioned above, M_{S2EW} depends on the respective MFA in that specific sample. Thus, direct allocation of M_{S2EW} to either degraded or non-degraded conditions as well as to WR or BR is prevented by the considerable variation of MFA in EW (Table 4.2). Higher H_{S2EW} on the other hand can be associated to degradation effects, because H_{S2EW} is not affected by the MFA.

In LW (Figure 4.2b), a minor share of the samples separates from non-degraded ones on PC1 (28%), indicating the smaller (relative) differences in LW due to degradation. Positive scores of WR12 and BR6 samples, exhibiting a similar mass loss, are quite similar in LW, while pronounced differences are observed in EW on PC1 (Figure 4.2a). Degradation types again separate along PC2 (22%), with WR samples scoring negatively and BR samples scoring positively. To be able to qualitatively compare the results

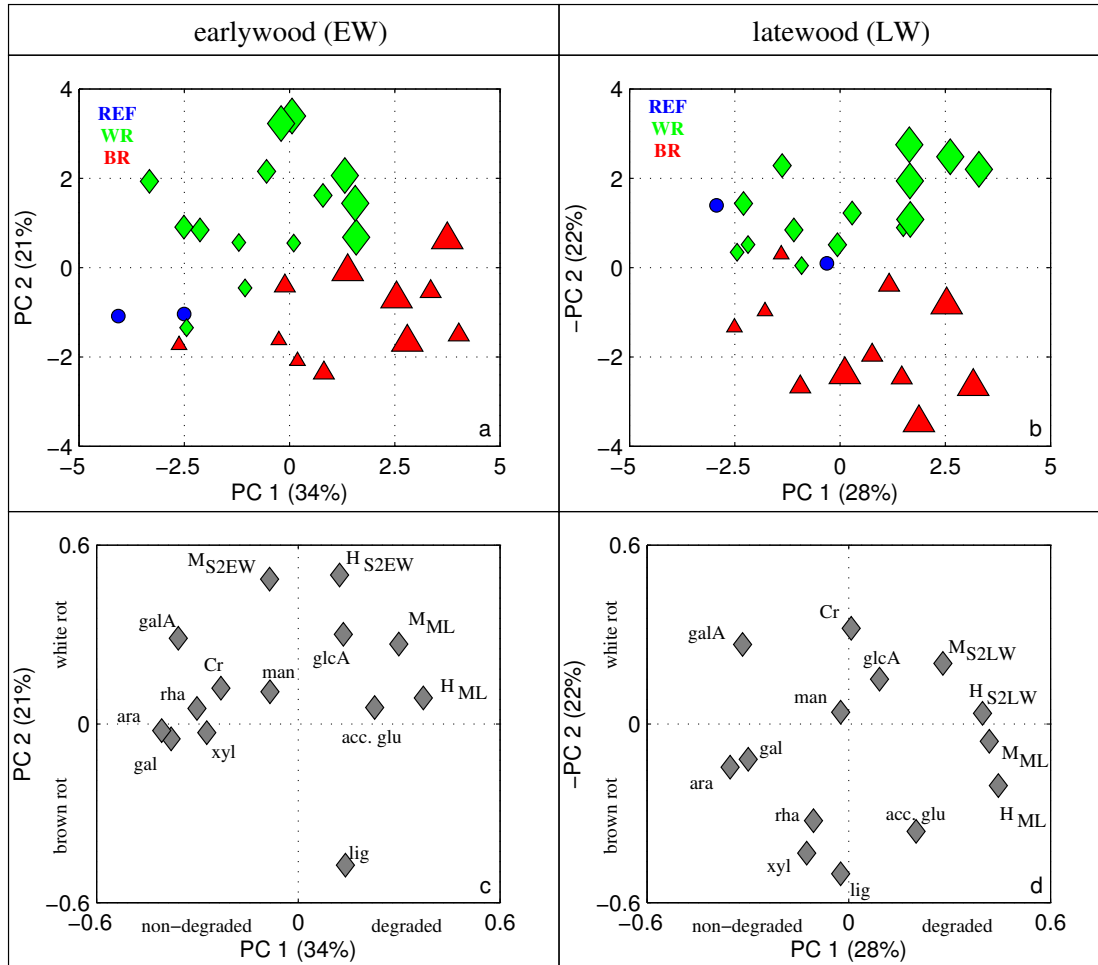


Figure 4.2: PCA scores (a,b) and loadings (c,d) plots of earlywood (EW, a,c) and latewood (LW, b,d) samples. (a,b) The degradation time is indicated by the size of the symbols (small – REF, WR2, BR2; medium – WR6, BR4; large – WR12, BR6); (c,d) ara – arabinan, gal – galactan, galA – galacturonan, rha – rhamnan, xyl – xylan, man – mannan, glcA – glucuronan, acc. glu – accessible glucan, *Cr* – crystallinity, M_{S2EW} – indentation modulus of S2 layer in EW, H_{S2EW} – indentation hardness of S2 layer in EW, M_{ML} – indentation modulus of middle lamella, H_{ML} – indentation hardness of middle lamella. PC2 for LW (b,d) was inverted for better comparability with EW (a,c)

of the PCA for LW, PC2 was inverted for the plots in Figure 4.2b,d. The remaining PCs (50%) again represent raw material variability.

The PCA loadings of LW samples (Figure 4.2d) reveal again differences in chemistry, molecular structure, and micromechanical properties, which are more pronounced than for EW samples.

Again, variables showing clear trends already in the raw data (Tables 4.1-4.2), exhibit the highest loadings on PC1 and PC2. Degraded LW cell walls are also depleted in pectic sugars ara, gal and galA, show higher M_{S2LW} and H_{S2LW} as well as higher M_{ML}

and H_{ML} , and have more acc. glu. Differences in contents of rha, xyl, man, and glcA, as well as in Cr , between degraded and non-degraded samples, are less evident in LW. As observed in EW, the increasing lignin content during BR and the decreasing lignin content in WR caused the PC1 loading of lignin to lie close to 0. The loadings of PC2 in LW reflect the differences between decay types, namely higher contents of xyl and lignin after BR decay, and more pronounced increase of the amount of acc. glu after WR decay. Cr is also shown to be higher in WR samples, resulting from the decrease in Cr upon BR decay (see also Table 4.2). As stated above for M_{S2EW} , the variability of the MFA prevents from allocating higher M_{S2LW} directly to degraded or non-degraded material and to WR or BR samples.

PCA of chemical, microstructural, and micromechanical data of EW and LW cell walls reveal a strong negative correlation of the content of pectic polysaccharides with M_{ML} and H_{ML} after both BR and WR decay. It is well known that pectic polysaccharides are mainly found in ML and primary cell walls (Fengel and Wegener, 2003). Their degradation coincides with the increase of M_{ML} and H_{ML} . The reason for this increase, however, has to remain a matter of speculation. Pectins are non-crystalline polysaccharides and due to their high degree of substitution and branching very flexible molecules. Their degradation might lead to an overall increase in stiffness of the ML. On the other hand, lignin, having its highest concentration in ML, is modified during BR degradation (Davis et al., 1994; Yelle et al., 2011) and broken down during WR decay, which might also cause alterations in mechanical properties in the ML. Furthermore, as stated before, the samples were heated for kiln drying to stop the fungal degradation process. This heating might have caused rearrangements of the cell wall polymers, contributing to the observed increase in ML and S2 layer stiffnesses.

4.3.5 Relation between ATR FT-IR Spectra and Micromechanical Data

The relationship between ATR FT-IR spectroscopic and micromechanical data was investigated by means of partial least squares regression (PLSR) analysis, which was performed for the spectral data from EW and LW during WR and BR decay and the indentation moduli M obtained from the ML and the S2 layer in EW and LW, to calculate predictions of M . In the following, PLSR models showing (1) M in the S2 layer ($M_{S2EW,PRED}$) for WR, (2) M in the ML ($M_{ML,PRED}$) for BR and (3) $M_{ML,PRED}$ for WR are presented, predicted from the EW spectra of the respective samples.

In Figure 4.3a) the correlation between $M_{S2EW,PRED}$ and the experimentally determined M_{S2EW} (mean values) within the EW sections is presented. The high coefficient of determination ($R^2=0.88$) indicates the correlation between $M_{S2EW,PRED}$ predicted from ATR FT-IR spectra and M_{S2EW} . This relation is not unexpected because mechanical properties of wood cell walls are determined by their chemistry and molecular structure, which are reflected in FT-IR spectra. However, it becomes evident, that a lot of variation is still present not only in the micromechanical properties (not shown in Figure 4.3), but also in the spectral data recorded within the same annual ring. SD

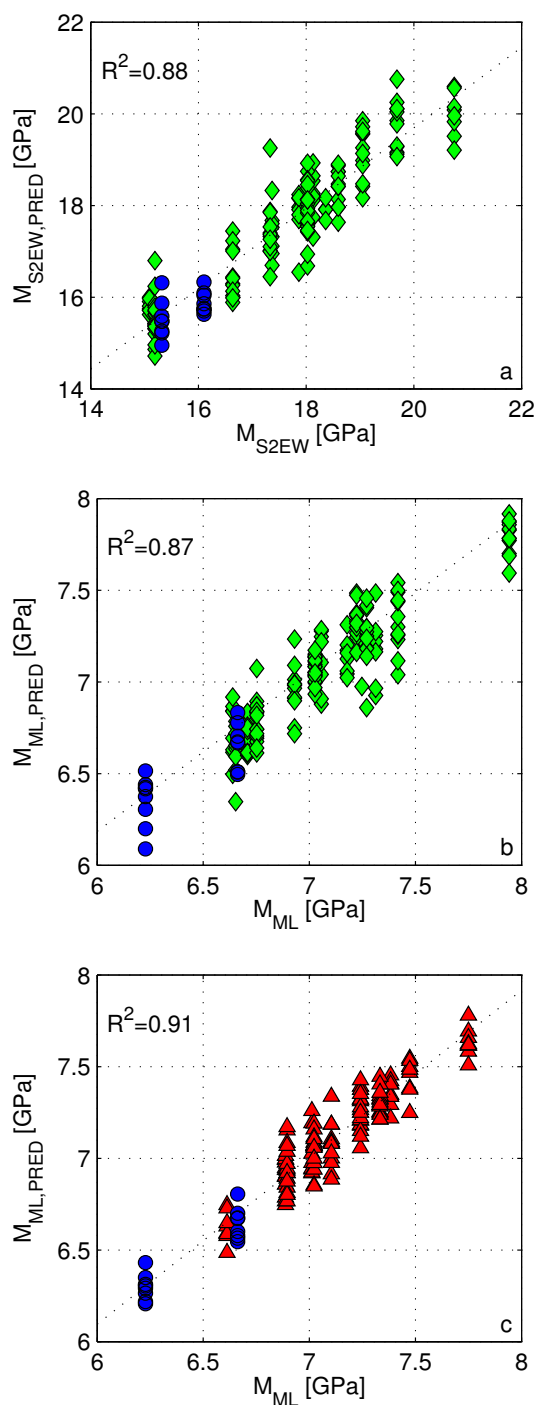


Figure 4.3: Predicted indentation moduli M from the PLSR models over the respective experimentally determined mean value of M for (a) the S2 layer in EW ($M_{S2EW,PRED}$) during WR decay and (b) the ML ($M_{ML,PRED}$) during WR and (c) BR decay predicted from the ATR FT-IR spectra of the respective EW sections; blue – REF, green – WR, red – BR samples

of $M_{S2EW,PRED}$ amounted to 0.13-0.68 GPa, as compared to the experimental SD of M_{S2EW} of 1.09-4.14 GPa (Table 4.2). The spectra and PLSR coefficients, which are not shown here, reveal well-known chemical and ultrastructural alterations (Fackler and Schwanninger, 2012) that are correlated to higher M_{S2EW} in WR compared to non-degraded cell walls. An increase of M_{S2EW} due to WR degradation is correlated to: (1) lower lignin content, (2) C α -oxidation of lignin moieties and (3) xyl degradation and therefore (4) relative increase of the native cellulose crystal allomorph I β . Significant regression coefficients (SRC) according to Martens' uncertainty test related to lignin content and lignin oxidation were therefore found at 1670 cm⁻¹ (conjugated p-substituted aryl-ketones), 1506 cm⁻¹ (aromatic skeletal vibrations of lignin), 1465 cm⁻¹ (asymmetric C-H bend of methoxyl groups). Xyl degradation was reflected in SRC at molecular vibrations due to acetyl groups of xyl (1731 cm⁻¹). Further SRC that could be assigned to the molecular structure of pine wood were found near 713 cm⁻¹ (cellulose crystal allomorph I β). The lower lignin and xylan content as well as the relative increase of C_r in EW during WR decay are indicated also already in the PCA for EW (Figure 4.2). Due to highly overlapping bands of all the various polysaccharides in pine wood (Schwanninger et al., 2004; Kačuráková et al., 2000), reflected in the high number of SRC in the spectral region from 1140-980 cm⁻¹ (C-O-C and C-O stretching vibrations), and due to their relatively low content (Table 4.1), the degradation of pectic polysaccharides did not become evident in the ATR FT-IR spectra of EW undergone WR decay.

$M_{ML,PRED}$ from ATR FT-IR spectra of WR and BR degraded EW sections (including the references) and the experimentally determined M_{ML} are clearly correlated, as shown again by high coefficients of determination ($R^2=0.87$ and 0.91 for WR and BR, respectively, Figure 4.3b-c). Again variability of the predictions for the same sample becomes evident, amounting to SD of 0.06-0.18 GPa for WR and of 0.06-0.13 GPa for BR, respectively. However, this variability is small, compared to the experimentally determined SD of 0.29-1.05 GPa for WR and of 0.20-0.76 GPa for BR, respectively (Table 4.2). The regression coefficients of the PLSR model for $M_{ML,PRED}$ in WR reflect similar features to those already described before for $M_{S2EW,PRED}$, with SRC at the above described wavenumbers. However, SRC related to lignin C α -oxidation (1670 cm⁻¹) and specifically to the crystal allomorph of cellulose (near 715 cm⁻¹) were absent in this case. Those of the BR model indicate degradation of man (867 cm⁻¹), which is more pronounced than that of xyl, which also became evident during the PCA (Figure 4.2c). Furthermore, significant regression coefficients, according to Martens' uncertainty test, are observed in the region of C-O stretching vibrations from approximately 1160-980 cm⁻¹ (Schwanninger et al., 2004), indicating substantial modifications of polysaccharides, including pectins.

4.4 Conclusions

Composition, microstructure and micromechanical properties of wood cell walls are changed differently by WR and BR fungi, and these alterations are highly variable. Nevertheless, investigations on the cell wall scale clearly showed that these alterations

were related to each other and could be detected already in very early stages of degradation. Differences between the observed changes during WR and BR decay have been caused by the different degradation mechanisms of the respective fungi. Chemical investigations revealed the well-known increase of lignin content during BR decay, as well as its decrease during WR decay. Pectic sugars were degraded during BR and WR decay. Hardness increased in the S2 layer as well as in the ML during BR and WR decay. PCA showed that the increased hardness of the ML is correlated to the decrease of pectic polysaccharides during both BR and WR decay. The increases in hardness of the S2 layer due to fungal decay were smaller than in the ML and are mainly associated to the loss of hemicelluloses. Differences between of these increases during BR and WR, i.e. higher hardness of the S2 layer after WR than after BR, coincide with the, relatively, higher Cr of the cell walls after WR decay. Increased stiffness after BR and WR decay could be detected in the ML, while the anisotropic nature of the S2 layer, together with the observed MFA variability among the samples, made it difficult to directly follow the modification of stiffness in the S2 layer. PLSR analysis could deliver links between the stiffness of the S2 layer and ultrastructural changes of lignin, lignin content as well as to ultrastructural changes of cellulose during fungal degradation. The increased stiffness of the ML is also correlated to the degradation of pectins.

Appendix 2: Compositional, Microstructural and Micro-mechanical Data

The following tables show the compositional data of the earlywood (EW) and latewood (LW) samples (Table 4.1) as well as their micromechanical and microstructural properties of the S2 layers and middle lamellae (Table 4.2).

Table 4.1: Chemical composition of earlywood (EW) samples; lig...lignin, ara...arabinan, xyl...xylan, rha...rhamnan, man...mannan, gal...galactan, acc. glu...accessible glucan, galA...galacturonan, glcA...glucoronan

Sample		lig [%]	ara [%]	xyl [%]	rha [%]	man [%]	gal [%]	acc. glu [%]	galA [%]	glcA [%]
REF.1	EW	26.88	2.47	6.21	0.39	11.53	2.82	3.71	2.36	0.57
	LW	26.86	1.71	4.33	0.25	14.51	2.45	4.47	1.44	0.49
REF.2	EW	26.86	1.83	5.98	0.59	10.86	2.41	3.88	1.82	0.34
	LW	25.53	1.37	4.83	0.30	16.26	2.05	5.26	1.17	0.49
BR2.1	EW	26.25	1.56	4.46	0.28	7.30	1.68	2.61	1.02	0.56
	LW	23.71	1.67	5.83	0.23	15.37	2.23	4.75	1.24	0.69
BR2.2	EW	26.69	1.97	7.55	0.41	10.49	2.71	4.25	1.52	0.53
	LW	24.31	1.74	6.73	0.34	13.18	2.21	4.63	1.20	0.52
BR2.3	EW	27.59	1.50	5.56	0.28	16.73	1.94	4.71	0.87	0.38
	LW	25.92	1.47	5.54	0.31	15.52	3.33	4.69	1.08	0.43
BR4.1	EW	28.90	1.11	4.74	0.21	7.95	1.20	6.69	0.77	0.46
	LW	25.24	1.33	5.51	0.37	13.53	1.64	7.09	0.85	0.52
BR4.2	EW	27.70	0.97	5.12	0.22	7.11	1.33	4.14	0.97	1.73
	LW	26.32	1.40	6.5	0.26	11.86	1.80	5.67	0.89	0.61
BR4.3	EW	26.33	1.55	6.54	0.34	12.82	1.99	5.12	1.27	0.43
	LW	25.53	1.61	7.22	0.33	18.05	2.27	6.08	1.03	0.54
BR4.4	EW	28.12	1.54	5.86	0.30	11.25	2.61	4.71	0.98	0.59
	LW	26.10	1.26	4.47	0.23	10.51	3.14	4.11	0.69	0.33
BR6.1	EW	27.57	1.35	5.41	0.28	9.08	1.56	7.61	1.03	1.26
	LW	27.44	1.36	6.44	0.29	16.37	3.56	5.90	1.05	0.68
BR6.2	EW	27.54	1.47	7.30	0.36	12.62	2.27	6.82	0.99	0.54
	LW	25.16	1.21	5.71	0.23	9.66	1.48	5.25	0.67	0.48
BR6.3	EW	27.31	1.21	4.25	0.22	11.28	1.97	4.78	1.09	0.62
	LW	26.01	1.56	7.08	0.34	16.02	2.02	7.45	0.94	0.63
BR6.4	EW	27.77	1.05	4.81	0.35	13.60	1.48	6.48	0.99	0.63
	LW	26.84	1.23	5.61	0.35	9.48	1.58	6.23	0.92	0.57
WR2.1	EW	26.12	1.70	5.89	0.40	13.38	2.42	4.83	2.01	0.53
	LW	23.91	1.36	4.81	0.40	15.06	2.00	4.49	1.39	0.65
WR2.2	EW	26.51	1.78	6.30	0.43	12.12	2.49	4.35	1.92	0.42
	LW	23.30	1.63	5.42	0.31	14.44	2.22	4.59	1.52	0.61

Continued on next page

Continued from previous page

Sample		lig	ara	xyl	rha	man	gal	acc. glu	galA	glcA
		[%]	[%]	[%]	[%]	[%]	[%]	[%]	[%]	[%]
WR2.3	EW	27.16	1.79	5.63	0.24	16.17	2.27	5.41	1.47	0.64
	LW	23.60	1.35	5.07	0.16	14.33	1.90	4.84	1.02	0.39
WR2.4	EW	26.25	1.49	5.55	0.29	12.57	2.49	4.14	1.64	0.53
	LW	23.62	1.41	5.48	0.27	15.37	3.87	4.11	1.37	0.51
WR6.1	EW	23.64	1.69	7.38	0.45	13.71	2.33	5.78	1.81	0.62
	LW	23.08	1.63	5.75	0.26	13.21	2.02	4.37	1.32	0.55
WR6.2	EW	24.21	1.64	5.64	0.38	12.30	2.24	5.02	1.69	0.70
	LW	22.63	1.18	4.23	0.32	14.23	1.88	4.91	1.20	0.48
WR6.3	EW	24.31	2.35	6.84	0.34	10.12	2.69	4.29	2.65	0.98
	LW	22.62	1.64	5.46	0.2	12.77	2.14	4.71	1.61	0.78
WR6.4	EW	24.29	2.07	5.24	0.38	11.09	2.49	4.49	2.11	0.58
	LW	22.67	1.75	5.21	0.27	12.03	2.18	4.29	1.26	0.48
WR6.5	EW	24.08	1.23	4.32	0.27	10.38	1.69	3.86	1.35	1.22
	LW	23.42	1.34	4.71	0.35	14.03	1.83	4.77	0.99	0.50
WR12.1	EW	23.14	1.66	6.07	0.44	12.63	2.07	5.44	1.90	2.12
	LW	21.85	1.21	4.19	0.30	17.07	1.75	5.65	1.26	0.40
WR12.2	EW	24.30	1.12	4.56	0.30	10.29	1.54	4.29	1.42	1.49
	LW	22.57	0.93	3.75	0.2	14.71	1.54	4.97	0.88	1.39
WR12.3	EW	23.92	1.08	4.68	0.30	13.70	1.69	5.98	1.40	1.71
	LW	22.12	0.92	4.57	0.28	16.91	1.46	6.31	1.11	1.89
WR12.4	EW	23.32	1.27	4.99	0.33	9.87	2.75	3.86	2.20	1.22
	LW	21.09	1.10	4.65	0.20	12.73	2.16	4.67	1.24	0.55
WR12.5	EW	24.33	1.44	4.63	0.31	11.61	1.79	4.31	1.49	0.31
	LW	21.42	1.05	3.59	0.25	14.52	1.58	4.38	1.06	0.40

Table 4.2: Microfibril angle (MFA) and sample crystallinity C_r of the S2 layer in earlywood (EW) and latewood (LW), as well as indentation moduli (M_{S2}) and hardness (H_{S2}) the S2 layer in EW and LW and in the middle lamella (ML)

Sample		S2				ML	
		MFA [°]	C_r [%]	M [GPa]	H [GPa]	M [GPa]	H [GPa]
REF.1	EW	11.6	31.7	16.10±1.62	0.38±0.02	6.23±0.29	0.30±0.02
	LW	7.8	31.5	18.81±1.19	0.38±0.02		
REF.2	EW	17.6	32.6	15.32±4.14	0.38±0.09	6.66±0.62	0.34±0.02
	LW	7.8	32.2	18.74±1.92	0.39±0.08		
BR2.1	EW	16.4	31.3	15.29±1.75	0.35±0.04	6.61±0.29	0.32±0.02
	LW	13.4	29.7	18.39±2.38	0.39±0.04		
BR2.2	EW	9.3	32.0	15.67±1.80	0.34±0.03	7.01±0.46	0.31±0.02
	LW	17.7	29.4	19.08±1.71	0.37±0.02		
BR2.3	EW	11.0	31.7	16.70±2.35	0.36±0.04	6.89±0.49	0.30±0.03
	LW	17.3	27.8	17.82±1.24	0.33±0.03		
BR4.1	EW	14.3	29.4	15.55±2.46	0.39±0.05	7.38±0.21	0.37±0.02
	LW	7.7	30.3	17.12±2.81	0.38±0.05		
BR4.2	EW	21.0	30.5	14.89±2.65	0.39±0.04	7.47±0.68	0.36±0.03
	LW	9.2	30.8	16.51±1.49	0.37±0.03		
BR4.3	EW	14.3	31.6	16.68±1.98	0.39±0.04	7.10±0.66	0.34±0.02
	LW	9.6	30.1	15.88±2.86	0.37±0.05		
BR4.4	EW	19.3	27.8	14.50±2.22	0.36±0.05	7.02±0.20	0.36±0.02
	LW	11.1	28.0	18.53±1.72	0.43±0.04		
BR6.1	EW	19.6	15.9	15.75±1.59	0.39±0.04	6.90±0.34	0.36±0.03
	LW	7.5	29.9	18.34±2.51	0.43±0.05		
BR6.2	EW	15.7	27.8	16.92±2.41	0.43±0.03	7.24±0.28	0.38±0.01
	LW	7.0	31.5	18.13±1.59	0.43±0.02		
BR6.3	EW	9.9	30.3	12.24±2.08	0.38±0.04	7.33±0.46	0.39±0.03
	LW	8.5	28.7	20.17±1.14	0.41±0.03		
BR6.4	EW	15.0	28.3	16.71±2.19	0.44±0.05	7.75±0.76	0.39±0.02
	LW	13.6	29.0	18.81±1.31	0.43±0.03		
WR2.1	EW	9.6	30.1	18.36±2.39	0.39±0.03	7.25±0.77	0.33±0.02
	LW	8.3	29.3	18.07±1.37	0.36±0.03		
WR2.2	EW	19.9	32.7	15.09±2.22	0.36±0.05	6.64±0.36	0.32±0.03
	LW	8.7	29.1	17.68±1.71	0.35±0.03		
WR2.3	EW	15.7	31.5	17.87±2.37	0.41±0.03	7.31±0.48	0.34±0.01
	LW	8.4	29.3	20.43±0.82	0.43±0.02		
WR2.4	EW	16.6	31.2	17.37±1.55	0.39±0.06	6.65±0.44	0.32±0.02
	LW	8.1	29.5	18.61±1.61	0.39±0.04		
WR6.1	EW	24.9	31.7	16.64±2.96	0.41±0.04	6.71±0.63	0.32±0.02
	LW	10.7	30.6	18.57±1.68	0.41±0.03		

Continued on next page

Continued from previous page

Sample		S2				ML	
		MFA [°]	Cr [%]	M [GPa]	H [GPa]	M [GPa]	H [GPa]
WR6.2	EW	22.5	28.7	20.75±1.09	0.44±0.02	7.06±0.34	0.33±0.02
	LW	9.7	30.6	19.51±0.98	0.38±0.02		
WR6.3	EW	14.7	34.8	18.13±1.48	0.41±0.02	7.18±1.05	0.32±0.02
	LW	9.9	34.2	18.35±1.09	0.36±0.03		
WR6.4	EW	18.7	32.8	18.03±1.81	0.4±0.02	6.75±0.47	0.31±0.02
	LW	19.0	33.6	17.29±1.93	0.35±0.03		
WR6.5	EW	10.5	31.4	19.05±1.11	0.42±0.02	6.93±0.42	0.32±0.02
	LW	9.7	31.3	19.17±1.69	0.39±0.04		
WR12.1	EW	18.2	30.0	18.60±1.24	0.43±0.03	7.42±0.82	0.36±0.03
	LW	10.4	29.6	20.72±1.15	0.40±0.02		
WR12.2	EW	23.9	34.4	18.03±1.53	0.42±0.02	7.22±0.76	0.35±0.04
	LW	14.1	32.3	18.99±1.93	0.41±0.04		
WR12.3	EW	11.3	31.0	15.20±3.61	0.38±0.03	7.03±0.31	0.34±0.02
	LW	11.9	33.3	17.73±2.15	0.36±0.02		
WR12.4	EW	15.5	30.2	19.69±1.12	0.46±0.02	7.27±0.48	0.35±0.01
	LW	7.5	32.9	20.79±2.78	0.42±0.03		
WR12.5	EW	10.6	31.3	17.33±2.78	0.41±0.04	7.94±0.53	0.37±0.03
	LW	15.8	30.8	20.75±2.57	0.42±0.03		

Fungal Degradation of Softwood Cell Walls: Enhanced Insight through Micromechanical Modeling (Wagner et al., 2014b)

Authored by Leopold Wagner, Thomas K. Bader, Josef Eberhardsteiner and Karin de Borst

Accepted for publication *International Biodeterioration and Biodegradation*, 2014
DOI: [10.1016/j.ibiod.2014.05.010](https://doi.org/10.1016/j.ibiod.2014.05.010)

Fungal degradation is among the greatest hazards for standing trees as well as timber constructions. Herein we aim at gaining more detailed insight into the degradation strategies of wood destroying fungi and the consequences on the mechanical performance of wood. At the macroscale, the occurring losses of mass and of mass density mask effects of altered chemical composition and microstructure. Thus, it is necessary to step down the hierarchical organization of wood to the cell wall scale in order to resolve these changes and their mechanical impact. We present a multiscale micromechanical model which is used to estimate the stiffnesses of the S2 cell wall layer and the compound middle lamella of fungal degraded wood. Data from a detailed chemical, microstructural and micromechanical characterization of white rot and brown rot degraded Scots pine sapwood is analyzed. Comparing predicted cell wall stiffnesses with measured ones confirms the suitability of the approach. The model enables to establish structure-stiffness relationships for fungal degraded wood cell walls and to test hypotheses on yet unknown effects of fungal decay. The latter include the evolution of porosity, modifications of the cell wall polymers resulting in changes of their stiffnesses, as well as increasing cell wall crystallinity. The model predictions in general showed

good agreement with the predictions not considering pores in the cell wall. However, this finding does not rule out the formation of porosity. Other degradation related effects like modifications of the cell wall polymers as well as increased crystallinity have the potential to account for stiffness decreases upon the formation of pores.

5.1 Introduction

Fungi play a major role in the degradation processes of all biological materials in nature and thus, also in wood decay. Fungal degradation is among the greatest hazards for the integrity of standing trees as well as of interior and exterior timber constructions.

The macroscopic mechanical behavior of wood is determined by its inherent microstructure which is hierarchically organized. The levels of organization have been identified as the growth ring structure consisting of earlywood (EW) and latewood (LW), the individual wood cell walls, the cell wall layers, and the arrangement of the wood polymers in these layers in the fashion of a fiber-reinforced composite (Page, 1976; Fengel and Wegener, 2003).

The different degradation strategies of wood decaying fungi and the consequences on the wood cell wall composition and microstructure have been the subject of many research studies (Blanchette, 1984; Eriksson et al., 1990; Goodell, 2003; Lee et al., 2007a; Howell et al., 2009; Yelle et al., 2011; Bader et al., 2012b; Fuhr et al., 2012). Wood rotting fungi are categorized according to their mode of degradation into brown rot, white rot or soft rot (Eriksson et al., 1990; Schwarze, 2007), whereby only brown rot and white rot are relevant for above ground applications. Brown rot fungi directly utilize the more nutritious wood polysaccharides, in initial stages especially pectic polysaccharides and hemicelluloses, and modify lignin only to a limited extent (Goodell, 2003). White rot fungi are further categorized into selective white rot fungi, which first cleave lignin to get access and then decompose the polysaccharide components in the wood cell wall, and simultaneous white rot fungi degrading all wood polymers at the same time (Blanchette, 1984).

The mechanical consequences of fungal decay have been investigated (Wilcox, 1978; Winandy and Morrell, 1993; Curling et al., 2002; Bader et al., 2012a). These studies almost exclusively dealt with the overall macroscopic stiffness and strength loss, which was linked to the altered wood composition after fungal degradation. While showing statistical correlations, such efforts do not deliver causal relations between changed microstructure and loss of mechanical properties. Such structure-stiffness relationships start to be understood for sound wood (Cave, 1968; Niklas, 1992; Bergander and Salmén, 2002; Hofstetter and Gamstedt, 2009; Salmén and Burgert, 2009). However, it is unclear whether they also hold for deteriorated wood.

Fungal degradation of wood always features mass losses and mass density losses, which can be highly variable (Curling et al., 2002; Bader et al., 2012a). This makes investigations of structure-stiffness relationships of decaying wood difficult, as the occurring mass loss often masks effects of changing composition and microstructure in

the remaining wood cell walls on the effective wood properties. Thus it is necessary to step down the hierarchical organization of wood to the cell wall scale where the fungal degradation actually occurs. This can be achieved by multiscale modeling, which is the main focus of this paper. By developing such a model based on homogenization strategies, we aim at enhancing the current understanding of the mechanical consequences of fungal degradation and to derive currently missing structure-stiffness relationships for decayed wood.

Recently we presented results from an experimental campaign, gathering microstructural as well as mechanical data of fungal degraded wood cell walls, separately for EW and LW (Wagner et al., 2014c). The investigated material (Scots pine sapwood) had been deteriorated by either brown rot (BR) or selective white rot (WR) up to mass losses of 10%. In contrast to the common observation of decreasing stiffness upon fungal degradation at the clearwood level, we found increased stiffnesses at the wood cell wall scale. Links between altered composition, microstructure and these cell wall stiffnesses were established by means of multivariate data analysis (Wagner et al., 2014c). Multiscale modeling will allow us to raise these relations from a statistical to a physical level, and to finally derive the sought causal structure-stiffness relationships. It enables to identify the effects of individual altered compositional and microstructural characteristics of wood cell walls on their respective mechanical properties. Moreover, it also allows testing hypotheses on fungal degradation mechanisms, by comparing experimentally observed stiffness changes with predictions of the model obtained for specific assumptions of altered composition and microstructure.

5.2 Materials and Methods

5.2.1 Wood Cell Wall Structure

Wood cells exhibit a multi-layered cell wall, comprising a primary cell wall (P-layer), three secondary cell wall layers (S1, S2 & S3-layer), and the middle lamella (ML). The latter connects individual wood cells and ensures the load transfer between them (Page, 1976; Fengel and Wegener, 2003). The S2 cell wall layer comprises about 80% of the total cell wall volume (Fengel and Wegener, 2003; Salmén and Burgert, 2009). Thus the cell wall layers mainly responsible for the mechanical behavior of wood are the S2 cell wall layer and the ML. Following conventions of Fengel and Wegener (2003), we consider the ML together with the adjacent P-layer and refer to it to as the compound middle lamella (CML). The microstructures of the S2 layer and of the CML, respectively, exhibit different levels of organization. The S2 cell wall layer is described as a natural fiber-reinforced material, with cellulose fibers embedded in a lignin-hemicellulose matrix (Page, 1976; Salmén, 2004). The cellulose fibrils contain crystalline and amorphous regions, with typical crystallite lengths and thicknesses of 30 to 40 nm and 3 to 4 nm, respectively (Andersson et al., 2003; Peura et al., 2008). The cellulose fibrils are surrounded by glucomannan which appears to be oriented along the cellulose fibrils (Stevanic and Salmén, 2009). The so formed bundles, referred to as cellulose aggregates,

range from 15 to 20 nm in diameter and are oriented in parallel and inclined to the cell axis by the so called microfibril angle (MFA) (Salmén, 2004; Fahlén and Salmén, 2005; Donaldson, 2007). The surrounding matrix material consists of lignin and xylan, which have been reported to be only partly oriented, if at all (Stevanic and Salmén, 2009). In view of the lack of qualitative data on the anisotropy, the entire matrix material will be considered to be isotropic, whereas the resulting S2 cell wall layer material is assumed to be transversely isotropic. The CML constitutes a lignified pectic layer between the cells, with some randomly oriented cellulose fibrils intruding from the adjacent P-layers (Hafrén et al., 2000; Fengel and Wegener, 2003). This structure suggests isotropic behavior of the CML. Water and extractives are incorporated in the whole cell wall. 80% of all extractives are reported to be located in the S2 layer. The amount of water in the wood cell wall is determined by the equilibrium moisture content (EMC), which depends on temperature and relative humidity (Fengel and Wegener, 2003). According to the specific composition of each cell wall layer the individual moisture contents (MC) in the S2 layer and the CML are different (Gloimüller et al., 2012).

5.2.2 Homogenization Theory - Continuum Micromechanics

Homogenization theories aim at predicting properties of macroscopically homogeneous materials from their respective heterogeneous microstructure. A wide range of homogenization methods has been developed, ranging from rather simple rules of mixture to the numerical analysis of repetitive unit cells with complex internal structures. When only general statistical data about the microstructure is available but no detailed morphological information, mean field methods have proven powerful and efficient for the estimation of elastic properties (Suquet, 1997; Zaoui, 2002). The level of microstructural detail represented by mean field approaches matches well the level of knowledge of the wood cell wall microstructure, particularly in its degraded state. This motivates the use of mean field approaches in the current study. There, quasi-homogeneous subdomains, so called material phases, have to be chosen within representative volume elements (RVE). The characteristic length of the RVE l has to fulfill $l \gg d$, d standing for the characteristic dimension of the inhomogeneities within the RVE, and $l \ll L$, L being the characteristic dimension of the geometry or loading of a structure made up by the material defined by the RVE (“separation of scales”). The mechanical properties within one RVE can then be estimated from its phases by their inherent mechanical properties, their dosages, their shapes and their interactions, using the solutions for Eshelby-type matrix-inclusion problems (Eshelby, 1957). Depending whether the phase arrangement within the RVE is either fiber-matrix like or dispersed, the Mori-Tanaka method (Mori and Tanaka, 1973; Benveniste, 1987) or the self-consistent scheme (Zaoui, 2002) is applied, respectively. If a single phase exhibits a heterogeneous microstructure itself, the mechanical properties can be estimated by introducing RVEs within this phase, with characteristic lengths $l_2 \ll d$, comprising smaller phases with characteristic dimensions $d_2 \ll l_2$. Repeatedly applied, this leads to a multiscale homogenization scheme.

5.2.3 Multiscale Micromechanical Model for Sound Wood Cell Walls

Our modeling efforts build upon an existing multiscale micromechanical model for wood stiffness (Hofstetter et al., 2005), which will be extended and adapted for degraded material. The existing model has already undergone extensive validation for sound wood (Hofstetter et al., 2005; Hofstetter and Gamstedt, 2009; Bader et al., 2011b), and has also been used to a limited extent to predict mechanical properties of modified wood tissue (Konnerth et al., 2010; Bader et al., 2011a).

Multiscale models enable to go down to sufficiently small scales of observation, where 'universal' phase properties inherent to all wood tissues can be identified (Hofstetter et al., 2005). For the mechanically most relevant S2 cell wall layer, these phases are lignin, amorphous and crystalline cellulose, hemicelluloses, water and extractives (Hofstetter et al., 2005). In the CML also pectin constitutes such a 'universal' phase. The consideration of water as an individual phase with bulk material properties is obviously a simplification. However, it may approximate the physical state of water at moderate and high moisture contents reasonably well, and has been shown to provide suitable model predictions for moisture contents between 5% and 25% (Eitelberger, 2011). Treating water alternatively as softening agent of the other 'universal' phases would require knowledge about the softening behavior of each phase and about the distribution of water across the phases. This knowledge is largely not available and would introduce considerable uncertainty in the model.

The phase stiffnesses follow from molecular dynamic simulations for crystalline cellulose (Tashiro and Kobayashi, 1991) and from tests on extracted materials for amorphous cellulose, hemicellulose, and lignin (Table 5.1). The latter phases are assumed to show isotropic elastic behavior. Possible inaccuracies of the data used to specify the phase stiffnesses are assumed not to change the resulting trends of cell wall stiffness upon fungal decay. As regards pectin, elastic properties reported for individual pectic sugars and for pectic gels show wide ranges, e.g. shear moduli between several hundred MPa and 3 GPa (Axelos et al., 1991; Clark et al., 1994). A choice of $E_{PEC} = 1.3$ GPa and $\nu_{PEC} = 0.3$ leads to a shear modulus μ_{PEC} of 0.5 GPa (bulk modulus $k_{PEC} = 1.08$ GPa), lying within the reported range for quasistatic shear moduli of pectic substances. The full stiffness tensor C_r of each phase r is either defined via its respective bulk and shear moduli k_r and μ_r , or by the respective individual stiffness tensor components $C_{r,ijkl}$.

Only the continuum micromechanical homogenization steps of the mentioned multiscale model are applied herein, in order to predict the mechanical properties of the cell wall material. They are further adapted to account for the two different microstructural arrangements in the S2 layer and the CML. The resulting micromechanical models for the two layers differ in both the amount of homogenization steps and in the microstructure within the respective RVEs.

The multiscale micromechanical model of the CML exhibits 3 RVEs on different observation scales (Figure 5.1 left), being (1) the polymer network, formed by lignin, pectin, water and extractives, (2) the cellulose fibril, consisting of crystalline cellulose

Table 5.1: 'Universal' phase properties, k_r ...bulk modulus of phase r , μ_r ...shear modulus of phase r , $C_{crycel,ijkl}$...stiffness tensor components of crystalline cellulose; a...Eichhorn and Young (2001); b...Cousins (1978); c...Cousins (1976); d...Tashiro and Kobayashi (1991)

phase	material behavior	bulk modulus k [GPa]	shear modulus μ [GPa]	Ref.
amorphous cellulose	isotropic	$k_{amocel} = 5.56$	$\mu_{amocel} = 1.85$	a
hemicellulose	isotropic	$k_{hemcel} = 8.89$	$\mu_{hemcel} = 2.20$	b
lignin	isotropic	$k_{lig} = 5.0$	$\mu_{lig} = 2.2$	c
pectin	isotropic	$k_{pec} = 1.08$	$\mu_{pec} = 0.5$	
water	isotropic	$k_{H2O} = 2.3$	$\mu_{H2O} = 0.0$	
extractives	isotropic	$k_{ext} = 3.0$	$\mu_{ext} = 0.05$	

		stiffness tensor components C_{ijkl} [GPa]		
crystalline cellulose	tranversely isotropic	$C_{crycel,1111} = 34.86$	$C_{crycel,1122} = 0$	d
		$C_{crycel,3333} = 167.79$	$C_{crycel,2233} = 0$	
		$C_{crycel,1313} = 5.81$		

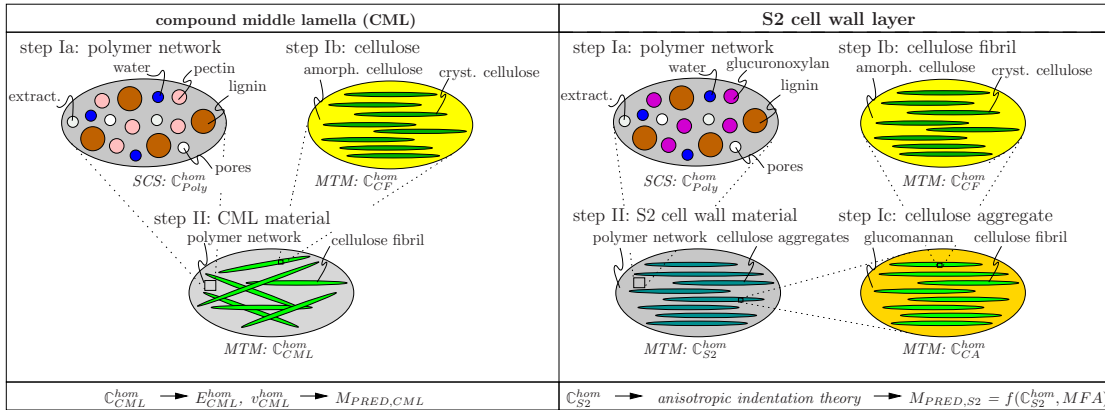


Figure 5.1: Schematic description of the multiscale micromechanical models of the compound middle lamella (CML) material (left) and the S2 cell wall layer (right); SCS...self-consistent scheme; MTM...Mori-Tanaka method; C_{Poly}^{hom} , C_{CF}^{hom} , C_{CML}^{hom} , C_{CA}^{hom} and C_{S2}^{hom} represent the homogenized stiffness of the polymer network, the cellulose fibril, the CML, the cellulose aggregate, and the S2 layer, respectively; E_{ML}^{hom} and ν_{ML}^{hom} are the homogenized Young's modulus and Poisson's ratio of the CML; $M_{PRED,CML}$ and $M_{PRED,S2}$ are the predicted indentation moduli of the CML and the S2 layer

units surrounded by amorphous cellulose, and (3) the CML material, consisting of randomly oriented cellulose fibrils, embedded in the polymer network. The effective elastic stiffnesses of these 3 RVEs are calculated by means of the self-consistent scheme (step Ia - polymer network) and by means of the Mori-Tanaka method (step Ib: cellulose fibril and step II: CML material), respectively.

The multiscale micromechanical model for the S2 cell wall layer differs from the model of the CML, as does the underlying microstructure. Based on the observed microstructure in the S2 layer, 4 RVEs can be defined at different observation scales (Figure 5.1 right). The polymer network (step Ia) and the cellulose fibril (step Ib) in the S2 layer are similar to that of the middle lamella, except for the different composition of the polymer network. The presence of pectin in the S2 layer was neglected (Fengel and Wegener, 2003). Hemicelluloses are divided into the two major compartments, namely glucuronoxylan and glucomannan, from which only glucuronoxylan is considered in the polymer network. The cellulose fibers are agglomerated to cellulose aggregates (3), consisting of parallel oriented cellulose fibrils, embedded in glucomannan. The cellulose aggregates themselves are finally embedded - again oriented in parallel - in the polymer network to form the S2 cell wall layer material (4). The effective elastic stiffnesses of these 4 RVEs are calculated by means of the self-consistent scheme (step Ia - polymer network) and by means of the Mori-Tanaka method (step Ib: cellulose fibril, step Ic: cellulose aggregate and step II: S2 cell wall material), respectively.

The multiscale approach needs volume fractions of the 'universal phases', listed in Table 1, as input, specifically for the S2 layer and the CML. The chemical composition of clearwood is typically specified in terms of dry mass fractions of these constituents. This composition, as well as microstructural characteristics, can also be determined specifically for EW and LW. However, it is impossible, at least by means of standard analysis procedures, to resolve differences between the individual cell wall layers. Therefore, the composition of the layers is determined from the EW/LW specific ones by means of distribution factors of the various components to the different layers given by Fengel and Wegener (2003). Table 5.2 summarizes these factors for cellulose, non-cellulose polysaccharides (i.e. hemicelluloses and pectins) and lignin, showing how much of each component is located in the S2 layer (different values for EW and LW) and how much in the CML.

Table 5.2: Distribution of cell wall components to compound middle lamella (CML), the S2 layer (which is not considered for modeling) and S2 layer in earlywood (EW) and latewood (LW) (Fengel and Wegener, 2003), CML fractions represent values for compound middle lamella (=ML+primary cell wall); CEL...cellulose, HC...hemicellulose, PEC...pectin, LIG...lignin

Layer	CEL	HC+PEC	LIG
CML	0.03	0.18	0.23
S1 (EW/LW)	0.10/0.05	0.26/0.17	0.14/0.07
S2 (EW/LW)	0.87/0.92	0.56/0.65	0.63/0.70

Since two different models are formulated for S2 and CML, the specific moisture content in each of these layers has to be determined as well from the overall moisture content. This is done based on the sorptive capacities of the components, following Gloimüller et al. (2012).

To obtain the sought volume fractions for each homogenization step, the overall mass fractions of the above described 'universal' phases in the S2 layer and in the CML are converted into corresponding volume fractions, using their respective mass densities. Finally, they are related to the respective reference volume of the homogenization step, which is for example the polymer network in step Ia or the cellulose fiber in step Ib (Hofstetter et al., 2005).

5.2.4 Modeling Fungal Degradation

Considering the effects of fungal degradation requires extension of the multiscale micromechanical models for the S2 cell wall layer and the compound middle lamella in sound wood. The occurring mass loss during fungal decay may result from thinning of wood cell walls or from the reduction of the mass density of the wood cell walls themselves by the formation of cell wall porosity, or from a combination of these two effects. Herein, we investigate only the two extreme scenarios, i.e. 'cell walls with pores and constant thickness' and 'cell walls without porosity but with reduced thickness'. Cell wall porosity is considered by introducing an additional pore phase in the model. During early stages of decay, BR mainly affects hemicelluloses and pectins (Fackler et al., 2010) and WR in addition lignin (Blanchette, 1984). Since all these polymers are components of the polymer network, the porosity was integrated in step Ia of the models for both the S2 layer and the CML, respectively (Figure 5.1). The volume fraction of the pores in the polymer network was derived from the overall mass loss. In a simplified manner, cell wall thinning was assumed to not change the relative share of the various cell wall layers and, thus, also not the distribution factors shown in Table 2. In consequence, no changes of the models for the S2 layer and the CML are necessary to incorporate cell wall thinning.

All other effects of fungal degradation, such as changing chemical composition and possible modifications of the properties of the universal phases, can be considered by changing the input parameters of the model, but do not require adaptations of the model itself. Because of limited knowledge and experimental data, some simplifying assumptions were made in a first step. The properties of the 'universal' phases, i.e. their mechanical properties (Table 5.1) and their sorptive capacities (Gloimüller et al., 2012), as well as the distribution factors of these phases over the S2 layer and the CML (Table 5.2) were considered to remain constant during the modeling of degradation. Also the cell wall crystallinity and the dimensions of the cellulose crystallites, in terms of their aspect ratio, were assumed constant, since only early stages of decay are investigated in this study. Some of these assumptions were challenged in the course of the model evaluations, and hypotheses about possible changes of these parameters were assessed from a mechanical point of view. In particular, the effect of a relative increase of cell wall crystallinity due to preferential degradation of amorphous wood polymers (Lee et al., 2007a; Howell et al., 2009) was studied, as well as the consequence of an increase of the stiffness of lignin due to de- and re-polymerization and oxidation during BR decay (Goodell, 2003).

5.2.5 Prediction of Nanoindentation Moduli

The performance of the model as well as the suitability of the aforementioned assumptions about degradation effects are assessed by comparing model predictions with experimental values. We use results obtained by nanoindentation for this purpose, which has established itself as the main method for determining mechanical properties of wood cell walls (Wimmer et al., 1997; Wagner et al., 2014a). It yields the so called indentation modulus M . In the CML, the assumption of isotropy enables to directly link the predicted Young's modulus E_{CML}^{hom} and the Poisson's ratio ν_{CML}^{hom} of the CML material to $M_{PRED,CML}$, following the standard approach by Oliver and Pharr (1992). In the S2 layer, the transverse isotropy of the material prevents such a direct comparison. Here M depends also on the inclination of the cellulose fibers with respect to the indentation axis. This inclination equals the MFA when the indent is done in the direction of the cell axis. M increases with decreasing MFA (Jäger et al., 2011a). A method to determine the indentation modulus from the five independent material constants of a transverse isotropic material and the MFA has been presented by Jäger et al. (2011a). It will be employed here to calculate a predicted indentation modulus of the S2 cell wall layer from the elastic constants obtained from the multiscale model.

5.2.6 Microstructural Input Parameters

The described modeling approach will be tested on data originating from a detailed chemical, microstructural and micromechanical characterization of Scots pine (*Pinus sylvestris* L.) sapwood, degraded by one BR fungus (*Gloeophyllum trabeum* [Pers.] Murril) and one selective WR fungus (*Trametes versicolor* [L.] Lloyd), respectively, as well as in sound, i.e. reference (REF), condition (Bader et al., 2012a,b; Wagner et al., 2014c). Only early stages of degradation with mass losses of approximately 1%, 5%, and 10%, were considered. This corresponds to two, four, and six weeks of BR (BR2, BR4 & BR6) and to two, six, and twelve weeks of WR (WR2, WR6 & WR12), respectively.

The experimental program was carried out on selected annual rings of two REF samples, three BR2 samples, four BR4, BR6, and WR2 samples, and five WR6 and WR12 samples. The cell wall stiffness has been determined by means of nanoindentation in the S2 layer in EW and LW as well as in the CML (Wagner et al., 2014c). For each sample, EW and LW were analyzed separately (i.e. 27 EW and 27 LW samples in total). The sample specific compositions of EW and LW of BR degraded, WR degraded and REF specimens were determined in terms of lignin content and contents of individual monosugars (Wagner et al., 2014c). Assumptions were made regarding the allocation of these monosugars to the distinct cell wall polymers serving as phases in the multiscale model. The sugar composition in galactoglucomannan (ggm) was estimated as being mannan:glucan:galactan (man:glu:gal) as 3:1:0, meaning that the presence of galactan side chains was neglected (Fengel and Wegener, 2003). Thus, for simplicity, galactoglucomannan is referred to as glucomannan. The glucurono-arabinoxylan (gax) sugar composition was estimated as being the sum of the resulting xylan and glucuronan

(xyl+glcA) from the acid methanolysis. The presence of arabinan (ara) in xylan, which according to literature can reach up to 10% (Fengel and Wegener, 2003) in xylans of pine wood, was neglected, thus glucurono arabinoxylan is referred to as glucuronoxylan. Galacturonan (galA), gal, ara, and rhamnan (rha) were summed up, referred to as pectic substances and allocated to the CML. Relating the pectin content to the sum of non-cellulosic polysaccharides yields a percentage of $17\pm 2\%$ (Wagner et al., 2014c), which agrees well with the reported amount of non-cellulose polysaccharides in the CML (Table 5.2) and, thus, justifies neglecting the presence of hemicelluloses in the CML. The extractives contents of EW and LW were assumed as 3.4% (average of all analyzed EW samples) and 2.5% (average of all analyzed LW samples), respectively (Table 5.3-5.4). The cellulose content was determined as residual after the subtraction of the contents of hemicellulose (i.e. gax+ggm), pectic sugars, lignin, and extractives from 100%. This might have led to some inaccuracies of the cellulose contents. Because of the indirect determination of the cellulose content, the cellulose crystallinity was not derived from a measured overall sample crystallinity. It was rather set to a constant value of $2/3$ for all samples (Fengel and Wegener, 2003), which was at first kept constant during degradation as described above.

The amounts of hemicelluloses, pectins, lignin and cellulose were averaged for each respective degradation stage (Table 5.3-5.4). The overall MC was set to the corresponding average EMC determined for each degradation stage (Bader et al., 2012a) and assumed to be constant within one annual ring (Table 5.3-5.4). Therefrom, the corresponding moisture contents of the S2 layer and the CML were determined according to the procedure described in Section 2.3. It results in slightly higher MC in the S2 layer than in the CML (Tables 5.5-5.6). Following the altered chemical composition after fungal degradation, the changes in MC upon degradation are higher in the CML and lower in the S2 layer, as compared to the overall changes in EMC (Tables 5.3-5.4). The mass fractions of the basic components in the S2 layer and the CML followed also from the distribution scheme outlined in Section 2.3. Finally, converting the mass fractions into volume fractions results in the composition data, summarized in Table 5.5 for the cell wall without pores and in Table 5.6 for the porous cell wall. The MFA was set to the average value in EW or in LW, respectively, for each degradation stage (Table 5.3-5.4).

5.3 Results and Discussion

5.3.1 Experimental Observations on Cell Wall Stiffness upon Fungal Degradation

The model performance and the underlying assumptions about degradation mechanisms are assessed by comparing model predictions with experimentally determined indentation moduli M_{EXP} (Wagner et al., 2014c). Indents were placed into the S2 layer of EW and LW tracheids (number of indents per sample $n_{S2,EW/LW} = 25-40$) as well as in the CML in the cell corners across the whole investigated annual ring ($n_{CML} = 10-15$). The indentation tests were conducted at $20\pm 2^\circ\text{C}$ / $60\pm 2\%$ relative humidity. The

indentation results are summarized for each degradation stage (REF, BR2, BR4, BR6, WR2, WR6 and WR12) in terms of the mean values and standard deviations (mean \pm sd) for M_{EXP} in the S2 layer of EW and of LW, respectively, and for M_{EXP} in the CML in Table 5.7. In brief, M_{EXP} was found to increase in the CML during both BR and WR degradation. A similar comparison of M_{EXP} values of the S2 layer for degraded and non-degraded samples is hindered by the pronounced variability of the MFA across the samples and the strong dependence of the indentation modulus on the MFA (Jäger et al., 2011a). However, it is still possible to compare samples with MFAs similar to that of the reference samples. This shows slightly increasing M_{EXP} , again during both BR and WR degradation, in EW as well as in LW. This increase is more pronounced for the WR samples. Also the variability of M_{EXP} in the S2 cell wall layer in EW and LW increased (Wagner et al., 2014c). This might be a consequence of the local nature of the nanoindentation test in combination with locally varying fungal activity. Moreover, also the kiln drying of the samples might have affected the samples and caused local clustering of microfibrils, taking advantage of nanopores created during the degradation. Depending on the indenter position during the test, either on a cluster or between, this would result in increased variability of the test results. When more indents were performed at cluster positions than in between, this may also have contributed to the observed overall stiffness increase.

Basically, an increase of the cell wall stiffness seems to be in contrast to the common observation of stiffness loss at the macroscopic or structural scale (Wilcox, 1978; Winandy and Morrell, 1993; Curling et al., 2002; Bader et al., 2012b). However, these decreases in macroscopic stiffness are mainly a consequence of considerable loss of cell wall material and related mass density loss. A potential slight increase of the stiffness of the remaining cell wall material would not show up at the macroscale because it will be masked by the effect of the loss of cell wall material.

5.3.2 Results from Micromechanical Modeling

The predicted indentation moduli M_{PRED} in the CML and the S2 cell wall layer in EW and LW are plotted in Figure 5.2 over the different stages of BR and WR degradation. Predictions obtained with and without porosity are shown.

The natural variability of wood already in the sound state complicates the identification of the effects of fungal degradation and poses the question how much of the observed variability of the nanoindentation data is related to the fungal activity and how much to the material as such. Variability of nanoindentation moduli of the S2 layer are in large part related to varying MFAs of the samples (Jäger et al., 2011a). Although remaining unchanged during fungal decay, the MFA is subject to variability within EW and LW of a single annual ring as well as within individual tracheids in sound wood (Lichtenegger et al., 2003; Wagner et al., 2013). Therefore, all predictions of M_{PRED} in the S2 layer have been calculated using the mean MFA of each degradation stage in EW and in LW, respectively (Tables 5.3-5.4). In order to investigate whether the MFA can explain the variability of the test results at each degradation stage, additional model

predictions were calculated with the minimum and maximum values of the MFAs of all samples for each stage (Figure 5.3). The resulting range of M_{PRED} using min/max MFA is similar to the experimentally observed range of M_{EXP} for specific degradation stages and either EW or LW. This justifies comparing mean trends observed in the experiments with the model predictions based on average MFAs in the following.

In the CML, the values predicted for a non-porous cell wall agree well with the trend of experimentally determined M_{EXP} for both BR and WR decay. The observed increase of M_{EXP} could be well reproduced with this modeling approach (Figures 2a and 2b). Also in the S2 layer, model predictions for the non-porous approach lie within the observed range of M_{EXP} during BR as well as WR decay (Figures 2c-f). Deviations are only observed after 6 weeks of WR decay in EW (Figure 5.2d), after 2 weeks of BR decay in LW (Figure 5.2e), and for the reference sample in LW (Figure 2f). Model predictions based on the assumption of pore formation in the cell wall are generally considerably lower than the measured values (Figure 5.2a-f). This tendency supports the idea that fungal degradation happens in a rather distributed fashion at the cell wall surfaces rather than at concentrated spots within the walls, eventually resulting in pores.

Basically, sound wood cell walls are considered to be free of pores (Fahlén and Salmén, 2005) or to exhibit only very small pores with diameters below 2 nm, which are accessible only to water and very small molecular substances (Hill et al., 2005). Experimental evidence of an increase of the pore size has only been reported for later stages of BR decay than considered herein (Flournoy et al., 1991). WR fungi use enzymes for wood degradation which can enter also sound (i.e. non-porous) cell walls. Their degradation activity can lead to the evolution of pores already during early stages of WR decay (Lee et al., 2007a), related to the breakdown of individual cell wall components. This seems to be in contrast to our finding that model estimates obtained for non-porous cell walls agree better with experimental results than those for porous ones. A possible explanation for this contradiction is that the pore space that might have evolved during early stages of fungal degradation did not yet become mechanically relevant in an indentation test. The mainly compressive nature of the loading in such a test may have resulted in closure of the still small pores, so that they participate in the load transfer and do not affect the response of the material. Moreover, the water, which is incorporated in the cell wall in moist conditions, might fill parts of the newly evolving pore structure. Considering again the compressive loading mode during the indentation tests together with the incompressibility of water, this filling may have helped to 'bridge' the gaps and prevented any stiffness loss in the indentation test. Finally, the treatment of the samples might have affected their microstructure. All samples were kiln dried at $103 \pm 2^\circ\text{C}$ according to EN 113 (1996) after the degradation in order to stop the fungal activity. The heating may have had an influence on the pore structure of the wood cell wall as well, as re-organizations of cell wall components might have taken place, closing this porosity. In addition, the heating might have altered the cell wall crystallinity (Bhuiyan et al., 2000; Toba et al., 2013), which will be addressed later on, or resulted in clustering of cellulose microfibrils as mentioned above.

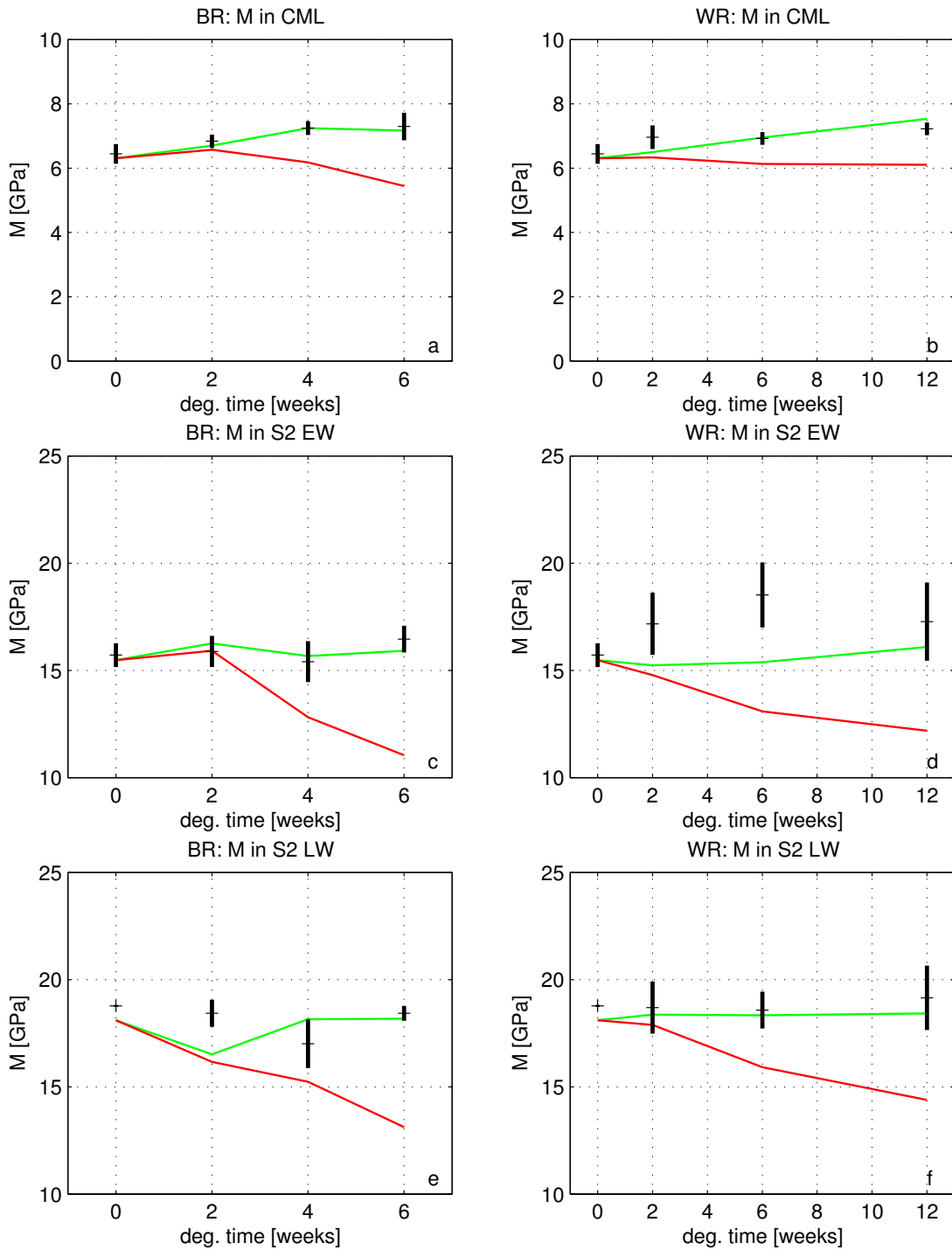


Figure 5.2: Model predicted indentation modulus M_{PRED} for brown rot (BR, a,c,e) and white rot (WR, b,d,f) degradation in compound middle lamella (CML, a-b), S2 layer in earlywood (S2 EW, c-d) and S2 layer in latewood (S2 LW, e-f); green: predictions without cell wall porosity, red: predictions with cell wall porosity, vertical black lines represent the range of experimental results (min-max)

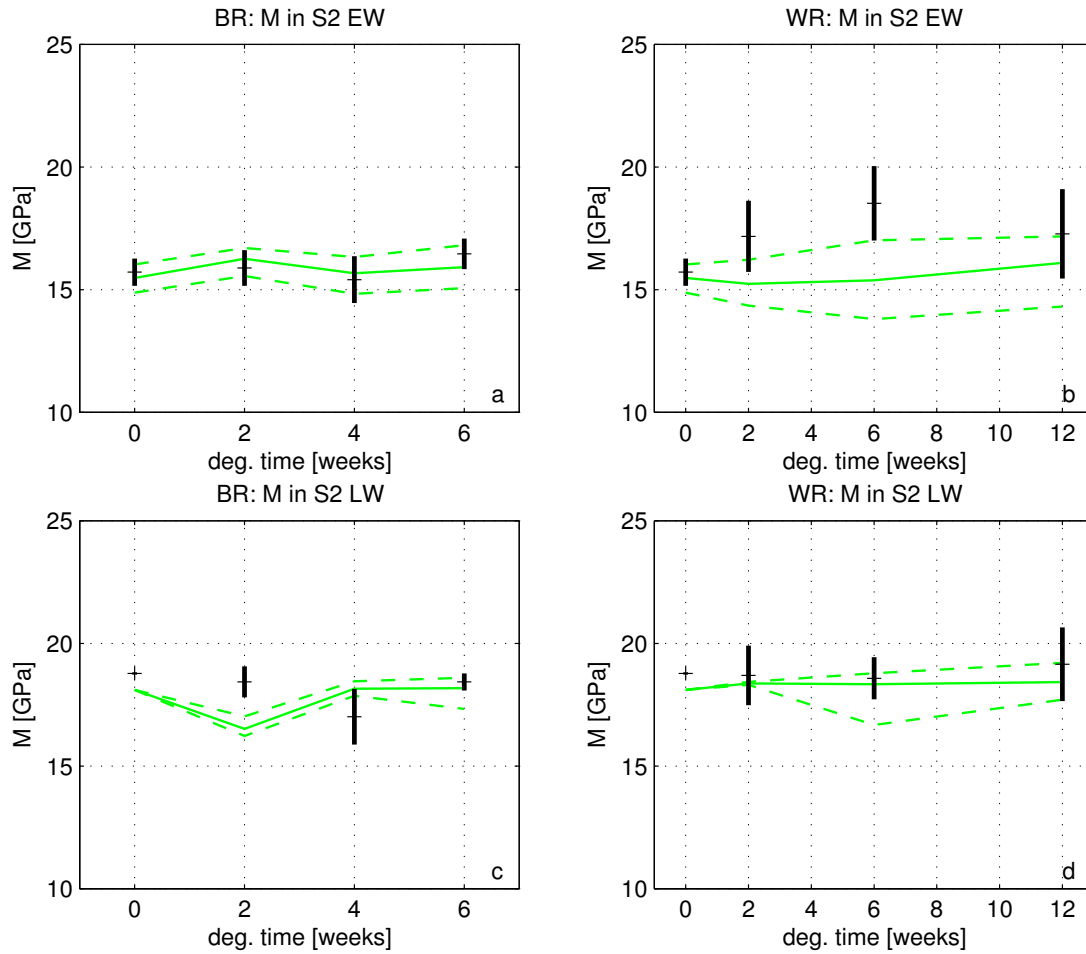


Figure 5.3: Predicted indentation modulus M_{PRED} for the S2 layer in EW (a-b) and LW (c-d) for brown rot (BR, a,c) and white rot (WR, b,d) decay, calculated with mean (solid green) and min/max MFA (dashed green) of the respective set of samples, i.e. degradation stage; vertical black lines represent the range of experimental results (min-max)

In general, the good agreement of model predictions with experimental results underlines the central role of changes in the chemical composition during fungal degradation, which are well captured in the model. The main effects during WR decay in the CML are decreases of the relative contents of pectin and lignin, together with an increase of the relative cellulose content (Table 5.3-5.4). A decrease of the softest component of the cell wall (pectin) and an increase of the by far stiffest component (cellulose) obviously bring about an overall increase of the stiffness in the CML. Since the lignin stiffness lies close to the predicted overall stiffness of the CML, its decrease does not affect the overall stiffness much. During BR decay, the lignin content increases, while cellulose and pectin contents decrease (Table 5.3-5.4). Again, the changing lignin content has no major influence on the CML stiffness. The effects of the decreasing pectin and cellulose contents partially balance each other. Since the reduction of the pectins is

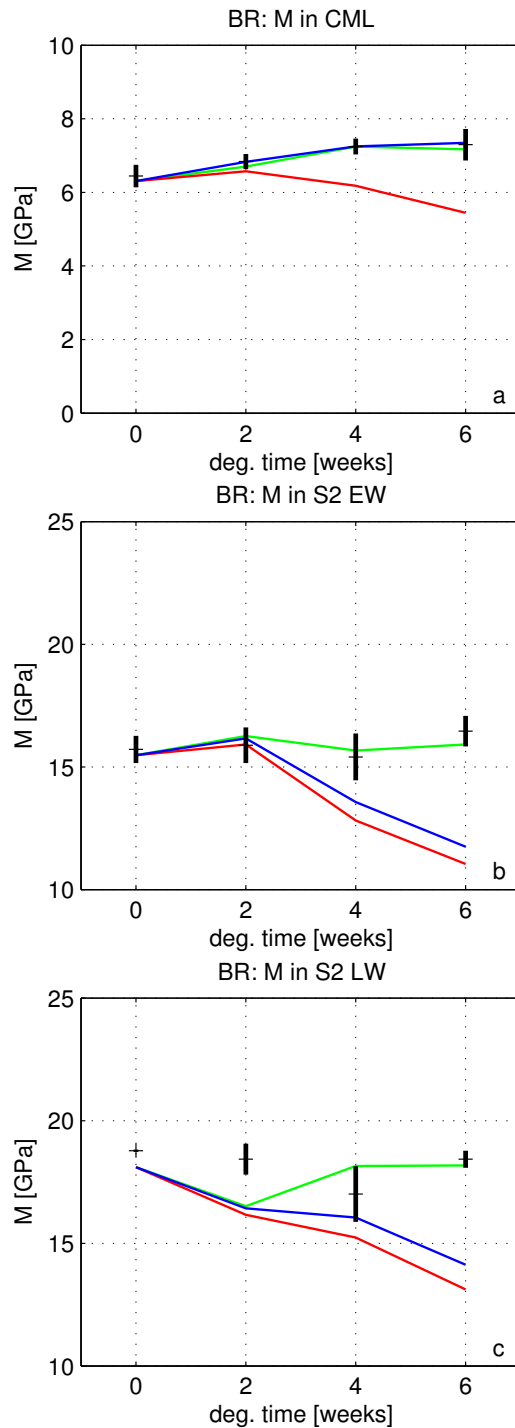


Figure 5.4: Influence of lignin stiffness E_{LIG} on the predicted indentation modulus M_{PRED} of the compound middle lamella (CML) (a) and the S2 layer in EW (b) and LW (c); green: predictions without cell wall porosity, red: predictions with cell wall porosity, blue: predictions with cell wall porosity and increased lignin stiffness to account for the decrease of M_{PRED} due to porosity (reference: $E_{LIG}=6$ GPa, 2 weeks BR: $E_{LIG}=7$ GPa, 4 weeks BR: $E_{LIG}=11$ GPa, 6 weeks BR: $E_{LIG}=19$ GPa), vertical black lines represent the range of experimental results (min-max)

much more pronounced, the overall CML stiffness still slightly increases upon decay. This trend is further reinforced by the decreasing MC in the CML throughout BR and WR decay. These observations seem to provide an explanation for previous findings of a relationship between increasing M and also indentation hardness H in the CML and the decreasing contents of pectic sugars in BR and WR degraded wood cell walls, in the framework of multivariate data analysis (Wagner et al., 2014c).

Similar observations hold for the S2 layer, except for the influence of the pectins which are absent from this layer. Again, the altered cellulose content has the largest effect, due to its high fraction in the S2 layer (Table 5.3-5.4) and its high stiffness (Table 5.1). Unfortunately, the cellulose content was only determined indirectly in this study as the residue after subtraction of all explicitly determined components, i.e. lignin and hemicellulosic and pectic sugars (Wagner et al., 2014c). This might have led to some inaccuracies in the determined cellulose contents, but will not have affected the overall trends discussed here. Again, the decreasing MC in the S2 layer contributes to the slight increases in the stiffness of this layer.

As described in Section 5.2.4, the model is based on some simplifying assumptions about the constancy of particular chemical and microstructural features during decay, in order to assemble the set of input data. In the following, some of these assumptions will be challenged. It will be assessed how sensitive the model predictions are to potential changes of the so far constant parameters, and whether such changes lead to an improved agreement of numerical and experimental results. This can provide support for certain hypothesized degradation effects, which are not yet fully resolved experimentally.

First, the assumption of constant lignin stiffness is analyzed as an example of altered 'universal' phase properties. Lignin was reported to be depolymerized and re-polymerized during brown rot decay (Goodell, 2003; Yelle et al., 2011). These modifications might alter the mechanical properties of lignin and might even increase its stiffness. This would provide another explanation for the observed increase of M_{EXP} during BR degradation, but would lead to an overestimation of M_{EXP} otherwise. One might consider that increased lignin stiffness could balance a potential stiffness loss upon pore formation, and that the negligence of these two effects has resulted in the good agreement of the predictions for the non-porous walls seen before. However, the elastic modulus of lignin would have to increase from its original value of 6 GPa to 7 GPa (+17%), 11 GPa (+83%) and 19 GPa (+217%) for BR2, BR4 and BR6, respectively, to compensate for the decrease of M_{PRED} upon evolving porosity during BR decay in the CML (Figure 5.4a). Moreover, these increases in E_{LIG} cannot balance the decrease of M_{PRED} in the S2 layers in EW and LW due to cell wall porosity (Figure 5.4b-c). Thus, it seems to be unrealistic that lignin stiffening is the reason for the observed increasing cell wall stiffness. Nevertheless, changes of the mechanical properties of the 'universal' phases certainly cannot be ruled out. The cell wall components undergo manifold modifications during BR and WR decay, but their effects on the mechanical properties of these components as well as on their interaction in the cell wall remain a matter of speculation to date. The model can serve as a tool in the future to test hypotheses on such effects, and to evaluate whether the related predicted changes

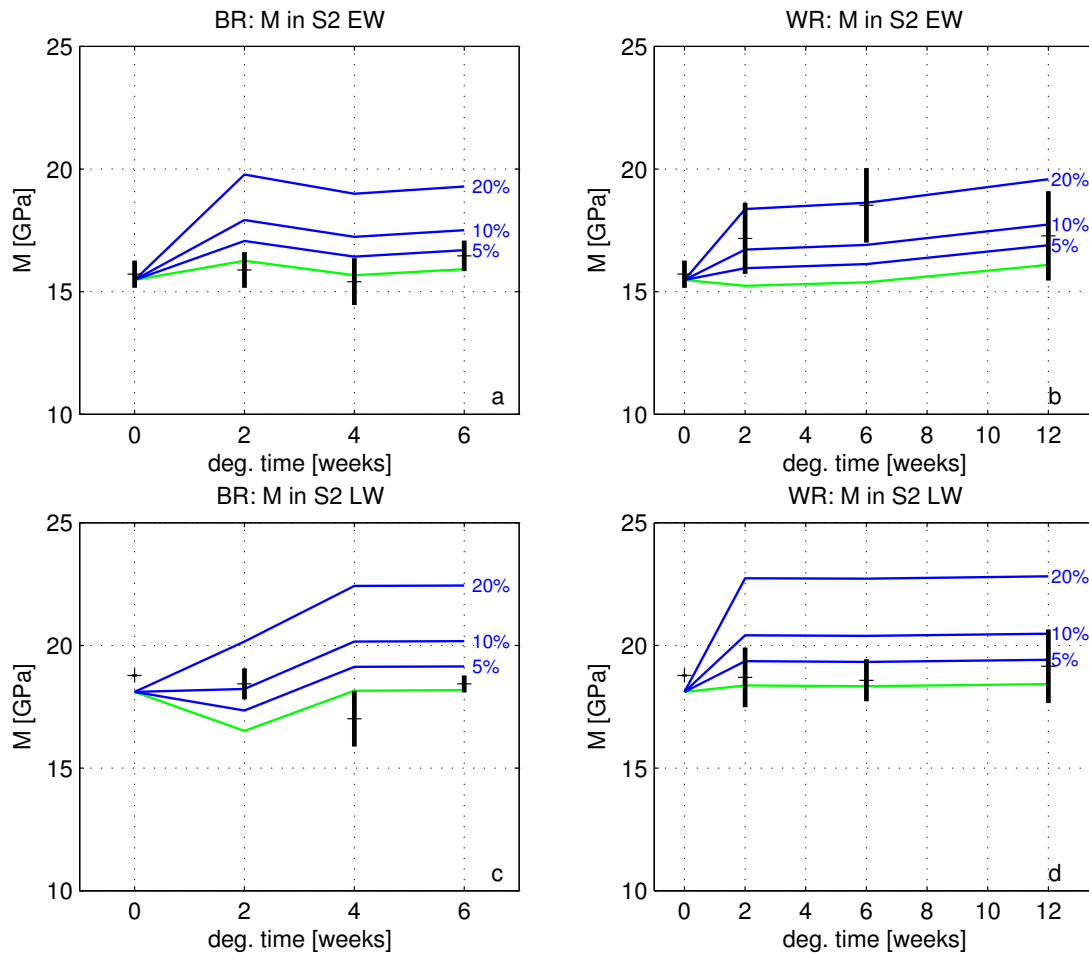


Figure 5.5: Influence of the sample crystallinity on the predicted indentation modulus M_{PRED} for the S2 layer in EW (a-b) and LW (c-d) for (BR, a,c) and white rot (WR, b,d) decay; green: predictions with reference crystallinity, blue: predictions with 5%, 10% and 20% increased crystallinity, vertical black lines represent the range of experimental results (min-max)

of the (observable and known) macroscopic mechanical behavior upon degradation are realistic or not.

Next, the assumption of constant cell wall crystallinity is assessed. Next to the chemical composition, the crystallinity is among the main control parameters of the stiffness of the S2 cell wall layer (Bader et al., 2012c). Crystallinity has been reported to increase in early stages of BR decay (i.e. up to 4 weeks) and then to decrease again (Howell et al., 2009), while WR fungi have been reported only to decrease crystallinity (Kleman-Leyer et al., 1992; Lee et al., 2007a). In the current study, the crystallinity may have also been affected by the kiln drying necessary to stop the fungal activity after the degradation. Heating of wood, especially in moist condition, has been found to result in increased cell wall crystallinity (Bhuiyan et al., 2000; Toba et al., 2013). Model predictions, taking into account the increases of crystallinity of 5%, 10% and 20% during

heating and as result of early BR and WR decay have been calculated (Figure 5.5). It can be seen that increasing crystallinity could provide an explanation for some deviations of M_{PRED} , as predicted by the original model, from M_{EXP} during BR and WR decay. However, the agreement of M_{PRED} to M_{EXP} could not be improved consistently by an increased crystallinity, which prevents drawing general conclusions.

Certainly, also the assumption of a constant distribution of the chemical components to the CML and the S2 layer (according to Table 5.2) is an approximation. It implies that the changes of the contents and, thus, the degradation of the individual components, occur equally in the S2 layer and the CML. This is contrary to some known non-uniform degradation patterns of some fungi. For example, BR fungi have been found to remove the CML while hardly attacking the S2 layer (Lee et al., 2004). Nevertheless these effects are not further explored herein, since not sufficient data are available to re-define, as a whole, the distribution factors to the S2 layer and the CML during fungal decay.

5.4 Conclusions

A multiscale micromechanical model was applied to investigate structure-stiffness relationships of fungal degraded softwood cell walls. Experimentally observed alterations of the wood cell wall composition and microstructure as well as other reported effects of fungal decay were incorporated in the model. Comparing the resulting model predictions with results of nanoindentation tests on degraded material enabled to assess the mechanical relevance of these effects. For merely hypothetical and not yet fully experimentally confirmed assumptions, the model provided some indications on how likely these effects might be. The variability of the experimental data could be to a good part explained by the variability of MFA in wood, existing already in the sound state.

The model predictions support that mass loss during early fungal decay does not necessarily involve the evolution of a mechanically relevant porosity in the S2 layer and the compound middle lamella (CML) which would affect the mechanical behavior, at least not under the compression-dominated loading states during nanoindentation. The predicted and experimentally observed increase of the stiffness of the CML mainly arises from the degradation of pectins, resulting in higher overall stiffness and lower equilibrium moisture content in the CML. The stiffness changes of the S2 layer in EW and LW during decay could be related to the reduction of the content of soft hemicelluloses. Further possible modifications due to fungal degradation, which were not based on results of quantitative chemical/microstructural analyses, were investigated by means of the model. These cover the evolution of pores in the cell wall, stiffening of lignin in consequence of its re-organization during degradation by BR fungi, and increasing cellulose crystallinity. Potential effects of the kiln drying of the samples to stop fungal activity, such as microfibril clustering, may have also contributed to the observed stiffness increase. This has not been investigated by means of the model and constitutes a topic of future research.

Appendix 3: Compositional and Microstructural Input Data

In the following tables all input data used for the multiscale micromechanical models of the S2 cell wall layer and the compound middle lamella (CML) are given. Tables 5.3 & 5.4 show the overall composition of the investigated earlywood (EW) and latewood (LW) regions (i.e. S2 layer and ML) in terms of mass fractions of the dry cell wall, the corresponding microfibril angle (minimum, mean and maximum MFA) (Wagner et al., 2014c), the overall mass loss as well as the overall moisture content u of the original macroscopic samples (Bader et al., 2012b). These mass fractions were converted into volume fractions according to Hofstetter et al. (2005), using their respective mass densities. Tables 5.5 and 5.6 show the composition in terms of volume fractions of the S2 layer in EW and in LW as well as of the ML not considering cell wall porosity and considering porous cell walls, respectively. These volume fractions were allocated to the homogenization steps (Figure 5.1), and related to the composition of the respective RVE (Hofstetter et al., 2005; de Borst and Bader, 2014). Table 5.7 summarizes the experimentally determined indentation moduli M_{EXP} of the S2 layer in EW and LW as well as in the CML.

Table 5.3: Input parameters for earlywood (EW) cell walls; mass fractions of cellulose (w_{CEL}), glucomannan(w_{GLU}), glucuronoxylan (w_{XYL}), lignin (w_{LIG}), pectin (w_{PEC}), extractives (w_{EXT}), microfibril angle (MFA), mass loss and moisture content (u); ^aWagner et al. (2014c); ^bFengel and Wegener (2003); ^cBader et al. (2012b)

EW	REF	BR2	BR4	BR6	WR2	WR6	WR12
w_{CEL} ^a	0.406	0.425	0.448	0.426	0.391	0.438	0.454
w_{GLU} ^a	0.149	0.153	0.130	0.155	0.181	0.154	0.155
w_{XYL} ^a	0.065	0.063	0.064	0.062	0.064	0.067	0.064
w_{LIG} ^a	0.272	0.272	0.281	0.279	0.268	0.244	0.241
w_{PEC} ^a	0.073	0.052	0.043	0.044	0.062	0.064	0.053
w_{EXT} ^b	0.034	0.034	0.034	0.034	0.034	0.034	0.034
MFA (mean) ^a [°]	14.6	12.6	17.2	15.0	15.1	18.3	15.9
MFA (min) ^a [°]	11.7	10.1	14.1	10.3	9.5	10.1	10.6
MFA (max) ^a [°]	17.6	16.1	21.0	19.1	19.6	25.5	24.0
mass loss ^c [%]	0.0	1.0	7.5	12.3	1.3	6.1	9.9
u ^c [%]	11.0	10.5	10.2	9.9	10.7	10.7	10.7

Table 5.4: Input parameters for latewood (LW) cell walls; mass fractions of cellulose (w_{CEL}), glucomannan(w_{GLU}), glucuronoxylan (w_{XYL}), lignin (w_{LIG}), pectin (w_{PEC}), extractives (w_{EXT}), microfibril angle (MFA), mass loss and moisture content (u); ^aWagner et al. (2014c); ^bFengel and Wegener (2003); ^cBader et al. (2012b)

LW	REF	BR2	BR4	BR6	WR2	WR6	WR12
w_{CEL} ^a	0.414	0.407	0.422	0.422	0.426	0.459	0.460
w_{GLU} ^a	0.205	0.196	0.180	0.172	0.197	0.177	0.202
w_{XYL} ^a	0.051	0.066	0.064	0.068	0.057	0.056	0.051
w_{LIG} ^a	0.251	0.249	0.261	0.266	0.239	0.232	0.221
w_{PEC} ^a	0.054	0.057	0.048	0.047	0.055	0.051	0.041
w_{EXT} ^b	0.025	0.025	0.025	0.025	0.025	0.025	0.025
MFA (mean) ^a [°]	7.8	16.4	9.7	9.9	8.9	12.4	12.0
MFA (min) ^a [°]	7.8	14.1	7.8	7.2	8.5	10.2	7.7
MFA (max) ^a [°]	7.8	17.7	11.3	14.1	9.3	19.4	15.2
mass loss ^c [%]	0.0	1.0	7.5	12.3	1.3	6.1	9.9
u ^c [%]	11.0	10.5	10.2	9.9	10.7	10.7	10.7

Table 5.6: Chemical composition of the S2 layer in earlywood (S2 EW) and latewood (S2 LW) as well as in the compound middle lamella (CML), volume fractions of cellulose (f_{CEL}), glucomannan(f_{GLU}), glucuronoxytan (f_{XYL}), lignin (f_{LIG}), water (f_{H_2O}) and extractives (f_{EXT}), with porosity ($f_{PORE} > 0$).

S2 EW							
S2 EW	REF	BR2	BR4	BR6	WR2	WR6	WR12
f_{CEL}	0.446	0.453	0.439	0.401	0.425	0.445	0.435
f_{GLU}	0.103	0.103	0.080	0.092	0.123	0.098	0.093
f_{XYL}	0.045	0.043	0.039	0.037	0.044	0.043	0.038
f_{LIG}	0.230	0.223	0.212	0.202	0.224	0.191	0.178
f_{H_2O}	0.121	0.115	0.105	0.097	0.116	0.111	0.107
f_{EXT}	0.056	0.054	0.050	0.048	0.055	0.052	0.049
f_{PORE}	0.000	0.010	0.075	0.123	0.013	0.061	0.099
S2 LW							
S2 EW	REF	BR2	BR4	BR6	WR2	WR6	WR12
f_{CEL}	0.433	0.426	0.408	0.387	0.441	0.445	0.424
f_{GLU}	0.152	0.145	0.123	0.112	0.145	0.121	0.132
f_{XYL}	0.038	0.049	0.044	0.044	0.042	0.039	0.033
f_{LIG}	0.219	0.218	0.210	0.204	0.206	0.188	0.170
f_{H_2O}	0.121	0.114	0.104	0.096	0.116	0.111	0.107
f_{EXT}	0.038	0.038	0.035	0.033	0.038	0.036	0.034
f_{PORE}	0.000	0.010	0.075	0.123	0.013	0.061	0.099
CML							
S2 EW	REF	BR2	BR4	BR6	WR2	WR6	WR12
f_{CEL}	0.090	0.096	0.096	0.089	0.093	0.100	0.105
f_{LIG}	0.466	0.483	0.482	0.462	0.465	0.429	0.431
f_{PEC}	0.293	0.267	0.214	0.203	0.282	0.268	0.227
f_{H_2O}	0.098	0.090	0.080	0.073	0.093	0.089	0.083
f_{EXT}	0.053	0.054	0.052	0.050	0.054	0.053	0.055
f_{PORE}	0.000	0.010	0.075	0.123	0.013	0.061	0.099

Table 5.7: Experimentally determined indentation moduli M_{EXP} (mean \pm sd) of the compound middle lamella (CML) and the S2 layer in earlywood (EW) and latewood (LW), from Wagner et al. (2014c)

		CML					
	REF	BR2	BR4	BR6	WR2	WR6	WR12
M_{EXP} [GPa]	6.45 \pm 0.31	6.83 \pm 0.21	7.25 \pm 0.22	7.29 \pm 0.43	6.96 \pm 0.37	6.93 \pm 0.20	7.22 \pm 0.20
S2 EW							
	REF	BR2	BR4	BR6	WR2	WR6	WR12
M_{EXP} [GPa]	15.71 \pm 0.55	15.88 \pm 0.73	15.41 \pm 0.95	16.46 \pm 0.62	17.17 \pm 1.45	18.52 \pm 1.52	17.27 \pm 1.82
S2 LW							
	REF	BR2	BR4	BR6	WR2	WR6	WR12
M_{EXP} [GPa]	18.77 \pm 0.05	18.42 \pm 0.63	17.01 \pm 1.13	18.43 \pm 0.35	18.69 \pm 1.22	18.58 \pm 0.86	19.15 \pm 1.50

Appendix 4: Multiscale Micromechanical Model for Fungal Degraded Wood Cell Walls

In the following the mathematical description of the multiscale micromechanical models for the stiffness of the S2 cell wall layer and the compound middle lamella, depicted in Figure 5.1, is presented. The composition, given in mass fractions, has to be converted into the respective volume fractions.

Distributing the Overall Mass Fractions to the S2 Layer and the Compound Middle Lamella

The overall mass fractions are distributed to the respective mass fractions of the S2 layer and the compound middle lamella (CML) according to the factors c_r listed in Table 5.2

$$w_{r,CML|S2} = \frac{c_{r,CML|S2}w_r}{\sum_s c_{s,CML|S2}w_s}, \quad s \in [\text{Cel}, \text{glu}, \text{xyl}, \text{lig}, \text{pec}]. \quad (5.1)$$

where $CML|S2$ has to be understood such that the calculations have to be performed separately for the S2 layer and the CML. In addition the calculations of the S2 layer were performed separately for EW and LW.

Determining the Moisture Content of the S2 layer and the Middle Lamella

The total amount of water within the cell wall reads as

$$w_{H2O} = w_{H2O,ML} + w_{H2O,S2}, \quad (5.2)$$

dividing by m_{dry} and taking into account

$$w_{H2O,CML|S2} = u_{CML|S2}m_{dry,CML|S2}, \quad (5.3)$$

leads to

$$u = w_{S2}u_{S2} + w_{CML}u_{CML}. \quad (5.4)$$

with w_{S2} and w_{CML} as mass fractions of S2 layer and CML. The relation between u_{S2} and u_{CML} is given by

$$\frac{u_{CML}}{u_{S2}} = \frac{s_{CML}}{s_{S2}}, \quad (5.5)$$

with s_{S2} and s_{CML} as the sorptive capacities of the S2 layer and the CML, constituting from the sorptive capacities of the individual phases (see Gloimüller et al. (2012))

$$s_{CML} = \sum_r s_r w_{r,ML} \quad \text{and} \quad s_{S2} = \sum_r s_r w_{r,S2}. \quad (5.6)$$

Converting Mass Fractions to Volume Fractions

The conversion of the mass fractions of the constituents of the S2 layer in EW and LW and the CML to volume fractions requires the respective mass densities of the “universal” phases (i.e. crystalline cellulose, amorphous cellulose, glucomannan, xylan, lignin, pectin, water and extractives) ρ_r , $r \in [\text{crycel}, \text{amocel}, \text{glu}, \text{xyl}, \text{lig}, \text{pec}, \text{H}_2\text{O}, \text{ext}]$, which are reported in literature (see e.g. Fengel and Wegener (2003) or Hofstetter et al. (2005)). To determine the crystalline part of cellulose mass fraction the degree of crystallinity with respect to volume Cr is converted into a degree of crystallinity with respect to mass Cr_w according to Hofstetter et al. (2005):

$$Cr_w = \frac{Cr}{Cr + (1 - Cr)\rho_{\text{amocel}}/\rho_{\text{crycel}}}, \quad (5.7)$$

with ρ_{amocel} and ρ_{crycel} as mass densities of amorphous (amocel) and crystalline cellulose (crycel). The respective mass fractions of amocel and crycel read as

$$w_{\text{crycel}} = Cr_w w_C \text{ and } w_{\text{amocel}} = (1 - Cr_w)w_C. \quad (5.8)$$

The mass fractions are given with respect to the dry cell wall. To calculate the mass fractions with respect to the wet cell wall, each mass fraction w_r is divided by $(1 + u)$, with u as the respective moisture content. The volume fractions f_r are calculated from

$$f_{r,CML|S2} = w_{r,CML|S2} \frac{\rho_{CML|S2}}{\rho_r}, \quad (5.9)$$

with

$$\rho_{CML|S2} = \left(\sum_r \frac{w_{r,CML|S2}}{\rho_r} \right)^{-1}, \quad r \in [\text{crycel}, \text{amocel}, \text{glu}, \text{xyl}, \text{lig}, \text{pec}, \text{H}_2\text{O}, \text{ext}]. \quad (5.10)$$

Stiffness of the ‘Universal’ Phases

The stiffness tensors of the above mentioned ‘universal’ phases have to be defined. Using the bulk and shear moduli k_r & μ_r ($r \in [\text{amocel}, \text{glu}, \text{xyl}, \text{lig}, \text{pec}, \text{H}_2\text{O}, \text{ext}]$), given in Table 5.1, the 4th order stiffness tensor \mathbb{C}_r of the phase r reads as:

$$\mathbb{C}_r = 3k_r \mathbb{J} + 2\mu_r \mathbb{K}, \quad r \in [\text{amocel}, \text{glu}, \text{xyl}, \text{lig}, \text{pec}, \text{H}_2\text{O}, \text{ext}], \quad (5.11)$$

where $\mathbb{J} = 1/3 \mathbf{I} \otimes \mathbf{I}$ and $\mathbb{K} = \mathbb{I} - \mathbb{J}$ are the volumetric and deviatoric parts of the 4th order unity tensor \mathbb{I} with components $I_{ijkl} = 1/2(\delta_{ik}\delta_{jl} + \delta_{il}\delta_{jk})$. The stiffness tensor of cellulose was given by its components $C_{\text{crycel},ijkl}$ (Table 5.1).

Stiffness of the S2 Cell Wall Layer (S2)

The stiffness of the polymer network in the S2 layer (S2,poly) – step Ia – is calculated by means of Self-Consistent scheme. The homogenized stiffness tensor of the polymer network $\mathbb{C}_{S2,poly}^{hom}$ reads as

$$\mathbb{C}_{S2,poly}^{hom} = \sum_r f_{r,S2,poly} \mathbb{C}_r : [\mathbb{I} + \mathbb{P}_r^0 : (\mathbb{C}_r - \mathbb{C}_{S2,poly}^{hom})]^{-1} : \left\{ \sum_s f_{s,S2,poly} [\mathbb{I} + \mathbb{P}_s^0 : (\mathbb{C}_s - \mathbb{C}_{S2,poly}^{hom})]^{-1} \right\}^{-1},$$

$$r, s \in [\text{lig}, \text{xyl}, \text{H2O}, \text{ext}, \text{Pore}]. \quad (5.12)$$

with the respective volume fractions

$$f_{r|s,S2,poly} = \frac{f_{r|s}}{\sum_{r|s} f_{r|s}}, \quad r, s \in [\text{lig}, \text{xyl}, \text{H2O}, \text{ext}, \text{Pore}]. \quad (5.13)$$

The stiffness of the cellulose fibril in the S2 layer (S2,CF) – step Ib – is calculated by means of Mori-Tanaka method. The homogenized stiffness tensor of the cellulose fibril $\mathbb{C}_{S2,CF}^{hom}$ reads as

$$\mathbb{C}_{S2,CF}^{hom} = \sum_r f_{r,S2,CF} \mathbb{C}_r : [\mathbb{I} + \mathbb{P}_r^0 : (\mathbb{C}_r - \mathbb{C}_{amocel})]^{-1} : \left\{ \sum_s f_{s,S2,CF} [\mathbb{I} + \mathbb{P}_s^0 : (\mathbb{C}_s - \mathbb{C}_{amocel})]^{-1} \right\}^{-1},$$

$$r, s \in [\text{amocel}, \text{crycel}]. \quad (5.14)$$

with the respective volume fractions

$$f_{r|s,S2,CF} = \frac{f_{r|s}}{\sum_{r|s} f_{r|s}}, \quad r, s \in [\text{amocel}, \text{crycel}]. \quad (5.15)$$

The stiffness of the cellulose aggregate in the S2 layer (S2,CA) – step Ic – is calculated by means of Mori-Tanaka method. The homogenized stiffness tensor of the cellulose aggregate $\mathbb{C}_{S2,CA}^{hom}$ reads as

$$\mathbb{C}_{S2,CA}^{hom} = \sum_r f_{r,S2,CA} \mathbb{C}_r : [\mathbb{I} + \mathbb{P}_r^0 : (\mathbb{C}_r - \mathbb{C}_{glu})]^{-1} : \left\{ \sum_s f_{s,S2,CA} [\mathbb{I} + \mathbb{P}_s^0 : (\mathbb{C}_s - \mathbb{C}_{glu})]^{-1} \right\}^{-1},$$

$$r, s \in [\text{CF}, \text{glu}]. \quad (5.16)$$

with the respective volume fractions

$$f_{r|s,S2,CA} = \frac{f_{r|s}}{\sum_{r|s} f_{r|s}}, \quad r, s \in [CF, glu]. \quad (5.17)$$

The stiffness of the S2 layer material (S2,CWM) – Step II – is calculated by means of Mori-Tanaka method. The homogenized stiffness tensor of the S2 layer material $\mathbb{C}_{S2,CWM}^{hom}$ reads as

$$\begin{aligned} \mathbb{C}_{S2,CWM}^{hom} = & \sum_r f_{r,S2,CWM} \mathbb{C}_r : [\mathbb{I} + \mathbb{P}_r^0 : (\mathbb{C}_r - \mathbb{C}_{S2,poly})]^{-1} : \\ & \left\{ \sum_s f_{s,S2,CWM} [\mathbb{I} + \mathbb{P}_s^0 : (\mathbb{C}_s - \mathbb{C}_{S2,poly})]^{-1} \right\}^{-1}, \\ & r, s \in [CA, poly], \end{aligned} \quad (5.18)$$

with the respective volume fractions

$$f_{r|s,S2,CWM} = \frac{f_{r|s}}{\sum_{r|s} f_{r|s}}, \quad r, s \in [CA, poly]. \quad (5.19)$$

Stiffness of the Compound Middle Lamella (CML)

The stiffness of the polymer network in the CML (CML,poly) – Step Ia – is calculated by means of Self-Consistent scheme. The homogenized stiffness tensor of the polymer network $\mathbb{C}_{CML,poly}^{hom}$ reads as

$$\begin{aligned} \mathbb{C}_{CML,poly}^{hom} = & \sum_r f_{r,CML,poly} \mathbb{C}_r : [\mathbb{I} + \mathbb{P}_r^0 : (\mathbb{C}_r - \mathbb{C}_{CML,poly}^{hom})]^{-1} : \\ & \left\{ \sum_s f_{s,CML,poly} [\mathbb{I} + \mathbb{P}_s^0 : (\mathbb{C}_s - \mathbb{C}_{CML,poly}^{hom})]^{-1} \right\}^{-1}, \\ & r, s \in [lig, HC, H2O, ext, Pore], \end{aligned} \quad (5.20)$$

with the respective volume fractions

$$f_{r|s,CML,poly} = \frac{f_{r|s}}{\sum_{r|s} f_{r|s}}, \quad r, s \in [lig, HC, H2O, ext, Pore]. \quad (5.21)$$

The stiffness of the cellulose fibril in the CML (CML,CF) – step Ib – is calculated by means of Mori-Tanaka method. The homogenized stiffness tensor of the cellulose fibril

$\mathbb{C}_{CML,CF}^{hom}$ reads as

$$\mathbb{C}_{CML,CF}^{hom} = \sum_r f_{r,CML,CF} \mathbb{C}_r : [\mathbb{I} + \mathbb{P}_r^0 : (\mathbb{C}_r - \mathbb{C}_{amocel})]^{-1} : \left\{ \sum_s f_{s,CML,CF} [\mathbb{I} + \mathbb{P}_s^0 : (\mathbb{C}_s - \mathbb{C}_{amocel})]^{-1} \right\}^{-1},$$

$$r, s \in [\text{amocel}, \text{crycel}], \quad (5.22)$$

with the respective volume fractions

$$f_{r|s,CML,CF} = \frac{f_{r|s}}{\sum_{r|s} f_{r|s}}, \quad r, s \in [\text{amocel}, \text{crycel}]. \quad (5.23)$$

The stiffness of the ML material (CML,CWM) – step II – is calculated by means of Mori-Tanaka method. The homogenized stiffness tensor of the ML material $\mathbb{C}_{CML,CWM}^{hom}$ reads as

$$\mathbb{C}_{CML,CWM}^{hom} = \sum_r f_{r,CML,CWM} \mathbb{C}_r : [\mathbb{I} + \mathbb{P}_r^0 : (\mathbb{C}_r - \mathbb{C}_{CML,poly})]^{-1} : \left\{ \sum_s f_{s,CML,CWM} [\mathbb{I} + \mathbb{P}_s^0 : (\mathbb{C}_s - \mathbb{C}_{CML,poly})]^{-1} \right\}^{-1},$$

$$r, s \in [\text{CF}, \text{poly}]. \quad (5.24)$$

with the respective volume fractions

$$f_{r|s,CML,CWM} = \frac{f_{r|s}}{\sum_{r|s} f_{r|s}}, \quad r, s \in [\text{CF}, \text{poly}]. \quad (5.25)$$

Summary and Outlook

In the following the main findings of the thesis are summarized and an outlook to future research perspectives, building on the work presented herein, is given.

Main Findings

A contribution to the ongoing discussion about the effect of the sample preparation process for nanoindentation, especially the effect of the embedding material, was made. Using different embedding materials did not lead to significant changes of the measured indentation moduli and hardnesses in the S2 cell wall layer. Apparently non-embedded cell walls did not show significantly different properties either. However, due to possible damage during the sample preparation process, apparently non-embedded cell walls tend to show substantially higher experimental scatter in their measured properties of the S2 layer. In addition, repeated drying and wetting of the wood samples prior to embedding had no significant effect on the resulting indentation moduli and hardnesses of both the S2 cell wall layer and the cell corner middle lamella (CCML). Only a slight increase of indentation hardness of both the S2 layer and the CCML could be detected. Finally, it could be shown that reasonable mechanical properties, i.e. indentation modulus and hardness, can be measured in the CCML, even when the size of the indent approaches the diameter of the CCML. A range of suitable indentation depths for the CCML was determined, which was applied in the following investigations.

Nanoindentation of cell walls of different wood species at varying moisture contents (MC) revealed common trends for the stiffness and creep properties in both the S2 cell wall layer and the middle lamella (ML). Cell wall stiffnesses were found to decrease with increasing MC. This effect was found to be predominated by the hemicellulose-lignin matrix, reflected by larger decreases in stiffness in the S2 layer with rising microfibril angle (MFA), as well as larger decreases in the ML as compared to the S2 layer in general. The curves showing the cell wall stiffness over MC exhibited a pronounced S-shape with the steepest decline between 5 and 10% MC, which was associated with the softening of hemicelluloses. Further losses of stiffness from MC at 80% relative humidity to fiber saturation were ascribed to additional softening of para-crystalline regions in the cellulose fibers. Creep values increased with increasing MC. In the S2 layer this increase started below 10% MC and was found to continue until fiber saturation, which could again be associated with softening of cellulose. The creep properties in the

ML were only affected to a smaller degree by changing MC below 10%, followed by a sharp transition at higher MC and again only small changes until fiber saturation.

Experimental investigations of variability patterns of wood stiffness within single trees at different length scales revealed an increase of the longitudinal stiffness as well as the rather constant transverse stiffness from pith to bark. Using the multiscale micromechanical modeling it could be shown that the variation of microstructural data such as the MFA and the mass density, determined by SilviScan-3™, could give an explanation for the experimentally observed pith-to-bark trends. It could be shown that not only the mass density, but also the MFA has to be considered to explain these stiffness trends. The variability patterns of cell wall stiffness were experimentally investigated from pith-to-bark as well as within selected annual rings from earlywood (EW) to latewood (LW) by means of nanoindentation. On the cellular level only the MFA is left as major microstructural influence parameter. On the pith-to-bark scale both the MFA and the indentation modulus turned out to be too localized measures and thus too much subject to random variability on top of the pith-to-bark trends in order to identify any trend of cell wall stiffness across this span. Within annual rings, i.e. from EW to LW, an increase of cell wall stiffness could be detected, which comes along with a decrease of the MFA. Multiscale micromechanical modeling was also applied to determine the variability of cell wall stiffness from pith-to-bark and within-annual-ring. Next to the influence of the MFA to the experimentally observed variability pattern of the cell wall stiffness, also the influence of the local chemical composition could be shown.

A detailed chemical, microstructural and micromechanical characterization of fungal degraded softwood cell walls revealed the different changes of composition, microstructure and mechanical properties of the S2 cell wall layer and the ML. The wood cell walls were affected differently, according to the different degradative strategies of white rot (WR) and brown rot (BR) fungi, respectively. In general, these alterations were highly variable. Most striking was the observed increase of stiffness of the S2 layer and the ML, which was in contrast to all previous findings at the macroscopic, i.e. clearwood, level. A possible explanation for this observation was proposed, based on the fact that increased stiffness of the remaining material at the cell wall level does not necessarily show up at the macroscopic level, in case that a sufficient amount of this stiffer material has been lost due to degradation, i.e. mass loss. The altered mechanical properties of the S2 layer and the ML could be linked to altered composition and altered microstructural characteristics, like the cell wall crystallinity, by means of multivariate data analysis. Principle component analysis and partial least squares regression analysis were applied. The altered mechanical properties of the S2 layer could be linked to ultrastructural changes of lignin, lignin content as well as to microstructural changes during fungal degradation. The increased stiffness and hardness of the ML could be linked to the degradation of pectic polysaccharides.

Multiscale mechanical modeling was applied to the results of the chemical and microstructural assessment of softwood cell walls, degraded by either BR or WR fungi, in order to investigate the causal relationships of the aforementioned links between composition, microstructure and mechanical properties of the S2 layer and the ML. Different

hypotheses about the impact of changes of composition and microstructure upon degradation have been tested, and the resulting stiffnesses were compared to the measured indentation moduli. According to our modeling results the mass loss at the cellular level might have its origin rather in a thinning of cell walls, than in a formation of a mechanically relevant cell wall porosity, if only altered composition upon BR or WR decay is considered. Invoking degradation related changes of the properties of wood cell wall components or changes in microstructural characteristics, enabled to partly compensate for decreases of the cell wall stiffness caused by evolving cell wall porosity.

Perspectives and Future Research Studies

The detailed chemical and microstructural characterization of the various hardwood and softwood samples, investigated by means of nanoindentation at different moisture contents (Wagner et al., 2014d), builds up the experimental reference to further study the **effect of water** on the mechanical properties of wood cell walls also by means of micromechanical modeling. Moisture related changes of cell wall stiffness might include re-considering the current way how water is considered in the mechanical model. One approach, which has been developed previously, is the application of poromechanics in the micromechanical model (see e.g. Bader et al. (2011b)). Water could also be considered in different steps of the multiscale micromechanical model, i.e. not only in the polymer matrix but also in e.g. the cellulose fibrils or cellulose aggregates, accounting for water sorption of the para-crystalline regions in the cellulose fibrils. Another, somewhat different, possibility would be not to treat water as a 'universal' phase, but to include a moisture dependency in the stiffness properties of the cell wall polymers, e.g. lignin, hemicelluloses or amorphous cellulose.

The gained insight on the degradation mechanisms of fungi and their effects on microstructure, composition and mechanical properties of wood cell walls have recently been used to investigate **archaeological wood**, which has been degraded by different kinds of bacteria in waterlogged conditions. Fragments of the *Oseberg* ship have been investigated by wet chemical methods and nanoindentation (Bader et al., 2013). A similar ongoing study is intended to investigate decay-related effects on the cell wall properties of wood fragments from the *Vasa* shipwreck. The *Vasa* shipwreck has been subject of many research studies before (Bjurhager et al., 2012; Svedström et al., 2012) and is thus well characterized in terms of microstructure and composition as well as in terms of macroscopic mechanical properties, i.e. stiffness and strength. In addition also the preservation treatment of the *Vasa*, namely the impregnation with polyethylene glycol (PEG), and its effects on the degraded wood material have been investigated (Sandström et al., 2002; Glastrup et al., 2006; Almkvist and Persson, 2008). As indicated herein, mass loss (and mass density loss) related changes of macroscopic stiffness potentially mask effects of altered cell wall stiffnesses. Nanoindentation tests on the cell walls of fragments of the *Vasa* shipwreck, in combination with existing and additional data from chemical and microstructural characterization, is expected to bring new insights into the effects of bacterial decay and effect of impregnation with PEG.

The gained compositional and microstructural data, together with the mechanical characterization by means of nanoindentation, could again be used to apply micromechanical modeling to the *Vasa* material. The investigations might also include the effect of the impregnation material (PEG) on the cell wall stiffness.

The **experimental micromechanical characterization** of wood cell walls, herein performed by means of nanoindentation, might be augmented by further methods, such as microtensile testing (Burgert et al., 2002, 2005a; Eder et al., 2009; Fischer et al., 2012) or microcompression tests (Zhang et al., 2010; Raghavan et al., 2012). These tests induce by far simpler stress states in the tested material, as compared to nanoindentation. Such tests, in combination with multiscale micromechanical modeling, will enable to investigate e.g. the role of the middle lamella stiffness and strength in overall longitudinal shear stiffness and strength of clearwood by means of tensile testing of the fiber-fiber bond of wood tracheids in situ or test S2 cell wall material in compression in different directions with respect to the MFA, to determine the transversely isotropic material constants for this layer experimentally.

Furthermore this work forms a framework for future numerical and experimental investigations of **modified wood** in general, i.e. thermally or chemically modified wood.

It has to be stated that the work presented in this thesis is clearly assigned to the field of basic research. The findings related to wood variability and wood degradation, gained herein, have to be translated to the clearwood scale first and then, by including growth irregularities like knots (Hackspiel et al., 2014; Lukacevic and Füssl, 2014), to the structural timber scale. Then, the effects of these findings at the cell wall scale might serve as basis for input parameters, e.g. for finite element simulations of structural timber.

Bibliography

- Alfredsen, G., Bader, T. K., Dibdiakova, J., Filbakk, T., Bollmus, S., and Hofstetter, K. (2012). Thermogravimetric analysis for wood decay characterisation. *European Journal of Wood and Wood Products*, 70:527–530.
- Almkvist, G. and Persson, I. (2008). Degradation of polyethylene glycol and hemicellulose in the *Vasa*. *Holzforschung*, 62:64–70.
- Alteyrac, J., Cloutier, A., Ung, C. H., and Zhang, S. Y. (2006). Mechanical properties in relation to selected wood characteristics of black spruce. *Wood and Fiber Science*, 38:229–237.
- Anagnost, S. E., Mark, R. E., and Hanna, R. B. (2002). Variation of microfibril angle within individual tracheids. *Wood and Fiber Science*, 34:337–349.
- Andersson, S., Serimaa, R., Paakkari, T., Saranpää, P., and Pesonen, E. (2003). Crystallinity of wood and the size of cellulose crystallites in Norway spruce (*Picea abies*). *Journal of Wood Science*, 49:531–537.
- Andréa, J. H. (1790). *Karakteristik inländischer Forstbäume und Sträucher in Tabellen kurz dargestellt. Nebst einem alphabetischen Verzeichniß der vornehmsten Schriftsteller über das Forstwesen. (in German)*. in der Andréaischen Buchhandlung, Frankfurt am Main.
- Arantes, V., Jellison, J., and Goodell, B. (2012). Peculiarities of brown-rot fungi and biochemical fenton reaction with regard to their potential as a model for bioprocessing biomass. *Applied Microbiology and Biotechnology*, 94:323–338.
- Astley, R. J., Harrington, J. J., and Stol, K. A. (1997). Mechanical modelling of wood microstructure, an engineering approach. *IPENZ Transactions*, 24:21–29.
- Astley, R. J., Stol, K. A., and Harrington, J. J. (1998). Modelling the elastic properties of softwood. Part II: The cellular microstructure. *Holz als Roh- und Werkstoff*, 56:43–50.
- ASTM D4761 (2013). Standard test methods for mechanical properties of lumber and wood-base structural material. *American Society for Testing and Materials (ASTM)*, West Conshohocken, PA, USA.

- Auty, D. (2011). *Modelling the effects of forest management on the wood properties and branch characteristics of UK-grown Scots pine*. PhD thesis, University of Aberdeen, Aberdeen.
- Auty, D., Gardiner, B. A., Achim, A., Moore, J. R., and Cameron, A. D. (2013). Models for predicting microfibril angle variation in Scots pine. *Annals of Forest Science*, 70:209–218.
- Axelos, M. A. V., Lefebvre, J., Qui, C.-G., and Rao, M. A. (1991). *The Chemistry and Technology of Pectin*, chapter Rheology of pectin dispersions and gels, pages 227–250. Academic Press Inc., San Diego.
- Back, E. and Salmén, L. (1982). Glass transition of wood components hold implications for molding and pulping process. *Tappi Journal*, 65:107–110.
- Bader, T. K., Alfredsen, G., Bollmus, S., and Hofstetter, K. (2012a). Changes in microstructure and stiffness of Scots pine (*Pinus sylvestris*) sapwood degraded by *G. trabeum* and *T. versicolor* - Part II: Anisotropic stiffness properties. *Holzforschung*, 66:199–206.
- Bader, T. K., Alfredsen, G., Bollmus, S., and Hofstetter, K. (2012b). Microstructure and stiffness of Scots pine (*Pinus sylvestris*) sapwood degraded by *G. trabeum* and *T. versicolor* - Part I: Physicochemical alterations. *Holzforschung*, 66:191–198.
- Bader, T. K., de Borst, K., Fackler, K., Ters, T., and Braovac, S. (2013). A nano to macroscale study on structure-mechanics relationships of archaeological oak. *Journal of Cultural Heritage*, 14:377–388.
- Bader, T. K., Hofstetter, K., Alfredsen, G., and Bollmus, S. (2011a). Decrease of stiffness properties of degraded wood predicted by means of micromechanical modelling. In *Proceedings of the 42nd Annual Meeting of the International Research Group on Wood Protection, Queenstown, New Zealand, May 8-11, 2011, Document Nr. IRG/WP 11-40570*.
- Bader, T. K., Hofstetter, K., Eberhardsteiner, J., and Keunecke, D. (2012c). Microstructure-stiffness relationships of Common yew and Norway spruce. *Strain*, 48:306–316.
- Bader, T. K., Hofstetter, K., Hellmich, C., and Eberhardsteiner, J. (2011b). The poroelastic role of water in cell walls of the hierarchical composite 'softwood'. *Acta Mechanica*, 217:75–100.
- Bendtsen, B. A. and Senft, J. (1986). Mechanical and anatomical properties in individual growth rings of plantation-grown Eastern cottonwood and Loblolly pine. *Wood and Fiber Science*, 18:23–38.
- Benveniste, Y. (1987). A new approach to the application of Mori-Tanaka's theory in composite materials. *Mechanics of Materials*, 6:147–157.

- Bergander, A. and Salmén, L. (2002). Cell wall properties and their effects on the mechanical properties of fibers. *Journal of Materials Science*, 37:151–156.
- Bhuiyan, M. T. R., Hirai, N., and Sobue, N. (2000). Changes of crystallinity in wood cellulose by heat treatment under dried and moist conditions. *Journal of Wood Science*, 46:431–436.
- Bjurhager, I., Halonen, H., Lindfors, E.-L., Iversen, T., Almkvist, G., Gamstedt, E. K., and Berglund, L. A. (2012). State of degradation in archaeological oak from the 17th century *Vasa* ship: substantial strength loss correlates with reduction of (holo)cellulose molecular weight. *Biomacromolecules*, 13:2521–2527.
- Blanchette, R. A. (1984). Screening wood decayed by white rot fungi for preferential lignin degradation. *Applied and Environmental Microbiology*, 48:647–653.
- Bodig, J. and Jayne, B. A. (1982). *Mechanics of Wood and Wood Composites*. Van Nostrand Reinhold, New York.
- Booker, R. E. and Sell, J. (1998). The nanostructure of the cell wall of softwoods and its functions in a living tree. *Holz als Roh- und Werkstoff*, 56:1–8.
- Briscoe, B. J., Fiori, L., and Pelillo, E. (1998). Nano-indentation of polymeric surfaces. *Journal of Physics D: Applied Physics*, 31:2395–2405.
- Bucur, V. (2006). *Acoustics of Wood*. Springer Verlag, Berlin Heidelberg New York.
- Burgert, I. (2006). Exploring the micromechanical design of plant cell walls. *American Journal of Botany*, 93:1391–1401.
- Burgert, I., Eder, M., Frühmann, K., Keckes, J., Fratzl, P., and Stanzl-Tschegg, S. (2005a). Properties of chemically and mechanically isolated fibres of spruce [*Picea abies* (L.) Karst.]. Part 3: Mechanical characterisation. *Holzforschung*, 59:354–357.
- Burgert, I., Frühmann, K., Keckes, J., Fratzl, P., and Stanzl-Tschegg, S. (2005b). Properties of chemically and mechanically isolated fibres of spruce [*Picea abies* (L.) Karst.]. Part 2: Twisting phenomena. *Holzforschung*, 59:247–251.
- Burgert, I. and Jungnikl, K. (2004). Adaptive growth of gymnosperm branches - ultrastructural and micromechanical examinations. *Journal of Plant Growth Regulation*, 23:76–82.
- Burgert, I., Keckes, J., Frühmann, K., Fratzl, P., and Tschegg, S. E. (2002). A comparison of two techniques for wood fiber isolation - evaluation by tensile tests on single fibers with different microfibril angle. *Plant Biology*, 4:9–12.
- Burgert, I. and Keplinger, T. (2013). Plant micro- and nanomechanics: experimental techniques for plant cell-wall analysis. *Journal of Experimental Botany*, 64:4635–4649.

- Carrington, H. (1922). The elastic constants of spruce as influenced by moisture. *The Aeronautical Journal*, 24:462–471.
- Cave, I. D. (1966). Theory of X-Ray measurement of microfibril angle in wood. *Forest Products Journal*, 16:37–42.
- Cave, I. D. (1968). The anisotropic elasticity of the plant cell wall. *Wood Science and Technology*, 2:268–278.
- Cave, I. D. and Walker, J. C. F. (1994). Stiffness of wood in fast-grown plantation softwoods: The influence of microfibril angle. *Wood Science and Technology*, 31:225–234.
- Clark, A. H., Evans, K. T., and Farrer, D. B. (1994). Shear modulus-temperature melt-down profiles of gelatin and pectin gels. A cascade theory description. *International Journal of Biological Macromolecules*, 16:125–130.
- Côté, W. A. (1965). *Cellular Ultrastructure of Woody Plants*. Syracuse University Press, New York, USA.
- Cousins, W. J. (1976). Elastic modulus of lignin as related to moisture content. *Wood Science and Technology*, 10:9–17.
- Cousins, W. J. (1978). Young's modulus of hemicellulose as related to moisture content. *Wood Science and Technology*, 12:161–167.
- Cramer, S., Kretschmann, D., Lakes, R., and Schmidt, T. (2005). Earlywood and latewood elastic properties in Loblolly pine. *Holzforschung*, 59:531–538.
- CSM Instruments (2002). Overview of mechanical testing standards. *Applications Bulletin*, No. 18.
- Curling, S. F., Clausen, C. A., and Winandy, J. E. (2001). The effect of hemicellulose degradation on the mechanical properties of wood during brown rot decay. In *Proceedings of the 32nd Annual Meeting of the International Research Group on Wood Protection, Nara, Japan, May 20-25, 2001, Document Nr. IRG/WP 01-20219*.
- Curling, S. F., Clausen, C. A., and Winandy, J. E. (2002). Relationships between mechanical properties, weight loss and chemical composition of wood during incipient brown-rot decay. *Forest Products Journal*, 52:34–39.
- Davis, M. F., Schroeder, H. A., and Maciel, G. E. (1994). Solid state ¹³C nuclear magnetic resonance studies of wood decay. *Holzforschung*, 48:301–307.
- de Borst, K. and Bader, T. K. (2014). Structure-function relationships in hardwood - insight from micromechanical modelling. *Journal of Theoretical Biology*, 345:78–91.

- de Borst, K., Bader, T. K., and Wikete, C. (2012). Microstructure-stiffness relations of ten European and tropical hardwood species. *Journal of Structural Biology*, 177:532–542.
- Déjardin, A., Laurans, F., Arnaud, D., Breton, C., Pilate, G., and Leplé, J. C. (2010). Wood formation in angiosperms. *Comptes Rendus Biologies*, 333:325–334.
- Donaldson, L. A. (2007). Cellulose microfibril aggregates and their size variation within cell wall type. *Wood Science and Technology*, 41:443–460.
- Donaldson, L. A. (2008). Microfibril angle: Measurement, variation and relationships - A review. *IAWA Journal*, 29:345–386.
- Downes, G. M., Nyakuengama, J. G., Evans, R., Northway, R., Blakemore, P., Dickson, R. L., and Lausberg, M. (2002). Relationship between wood density, microfibril angle and stiffness in thinned and fertilized *Pinus radiata*. *IAWA Journal*, 23(3):253–265.
- Eastwood, D. C., Floudas, D., Binder, M., Majcherczyk, A., Schneider, P., Aerts, A., Asiegbu, F. O., Baker, S. E., Barry, K., Bendiksby, M., Blumentritt, M., Coutinho, P. M., Cullen, D., de Vries, R. P., Gathman, A., Goodell, B., Henrissat, B., Ihrmark, K., Kauserud, H., Kohler, A., LaButti, K., Lapidus, A., Lavin, J. L., Lee, Y.-H., Lindquist, E., Lillz, W., Lucas, S., Morin, E., Murat, C., Oguiza, J. A., Park, J., Pisabarro, A. G., Riley, R., Rosling, A., Salamov, A., Schmidt, O., Schmutz, J., Skrede, I., Stenlid, J., Wiebenga, A., Xie, X., Kües, U., Hibbett, D. S., Hoffmeister, D., Högborg, N., Martin, F., Grigoriev, I. V., and Watkinson, S. C. (2011). The plant cell wall-decomposition machinery underlies the functional diversity of forest fungi. *Science*, 333:762–765.
- Eberhardsteiner, J. (2002). *Mechanisches Verhalten von Fichtenholz: - Experimentelle Bestimmung der biaxialen Festigkeitseigenschaften (in German)*. Springer Wien New York.
- Eder, M. (2007). *Structure, properties and function of single wood fibres of Norway spruce (Picea abies [L.] Karst.)*. PhD thesis, University of Natural Resources and Life Sciences, Vienna.
- Eder, M., Arnould, O., Dunlop, J. W. C., Hornatowska, J., and Salmén, L. (2013). Experimental micromechanical characterization of wood cell walls. *Wood Science and Technology*, 47:163–182.
- Eder, M., Jungnikl, K., and Burgert, I. (2009). A close-up view of wood structure and properties across a growth ring of Norway spruce (*Picea abies* [L.] Karst.). *Trees - Structure and Function*, 23:79–84.
- Ehrnrooth, E. M. L. and Kolseth, P. (1984). Tensile testing of single wood pulp fibers in air and in water. *Wood and Fiber Science*, 16:549–566.

- Eichhorn, S. J. and Young, R. J. (2001). The Young's modulus of a microcrystalline cellulose. *Cellulose*, 8:197–207.
- Eitelberger, J. (2011). *A multiscale material description for wood below the fiber saturation point with particular emphasis on wood-water interactions*. PhD thesis, Vienna University of Technology.
- El Omri, A., Fennan, A., Sidoroff, F., and Hihi, A. (2000). Elastic-plastic homogenization for layered composites. *European Journal of Mechanics A/Solids*, 19:585–601.
- EN 113 (1996). Wood preservatives - Method of test for determining the protective effectiveness against wood destroying basidiomycetes - Determination of the toxic values. *European Committee for Standardization (CEN), Brussels, Belgium*.
- EN 13183-1 (2002). Moisture content of a piece of sawn timber - Part 1: Determination by the oven dry method. *European Committee for Standardization (CEN), Brussels, Belgium*.
- EN 408 (2012). Timber Structures - Structural timber and glued laminated timber - Determination of some physical and mechanical properties. *European Committee for Standardization (CEN), Brussels, Belgium*.
- Engelund, E. T., Thygesen, L. G., Svensson, S., and Hill, C. A. S. (2013). A critical discussion of the physics of wood-water interactions. *Wood Science and Technology*, 47:141–161.
- Eriksson, D., Lindberg, H., and Bergsten, U. (2006). Influence of silvicultural regime on wood structure characteristics and mechanical properties of clear wood in *Pinus sylvestris*. *Silva Fennica*, 40:743–762.
- Eriksson, K. E. L., Blanchette, R. A., and Ander, P. (1990). *Microbial and Enzymatic Degradation of Wood and Wood Composites*. Springer New York Wien.
- Eshelby, J. D. (1957). The determination of the elastic field of an ellipsoidal inclusion and related problems. *Proceedings of the Royal Society of London. Series A, Mathematical and Physical Sciences*, 241:376–396.
- Evans, R. (1999). A variance approach to the X-Ray diffractometric estimation of microfibril angle in wood. *Appita Journal*, 52:283–294.
- Evans, R. (2006). *Characterization of the cellulosic cell wall*, chapter Wood stiffness by X-ray diffractometry, pages 138–146. Blackwell Publishing, Ames, IO, USA.
- Evans, R. and Ilic, J. (2001). Rapid prediction of wood stiffness from microfibril angle and density. *Forest Products Journal*, 51(3):1–6.
- Fackler, K. and Schwanninger, M. (2012). How spectroscopy and microspectroscopy of degraded wood contribute to understand fungal wood decay. *Applied Microbiology and Biotechnology*, 96:587–599.

- Fackler, K., Stevanic, J. S., Ters, T., Hinterstoisser, B., Schwanninger, M., and Salmén, L. (2010). Localisation and characterisation of incipient brown-rot decay within spruce wood cell walls using FT-IR imaging microscopy. *Enzyme and Microbial Technology*, 47:257–267.
- Fackler, K., Stevanic, J. S., Ters, T., Hinterstoisser, B., Schwanninger, M., and Salmén, L. (2011). FT-IR imaging microscopy to localise and characterise simultaneous and selective white-rot decay within spruce wood cells. *Holzforschung*, 65:411–420.
- Fahlén, J. and Salmén, L. (2005). Pore and matrix distribution in the fiber wall revealed by atomic force microscopy and image analysis. *Biomacromolecules*, 6:433–438.
- Fengel, D. and Wegener, G. (2003). *Wood - Chemistry, Ultrastructure, Reactions*. De Gruyter, Berlin.
- Fischer, W. J., Hirn, U., Bauer, W., and Schennach, R. (2012). Testing of individual fiber-fiber joints under biaxial load and simultaneous analysis of deformation. *Nordic Pulp & Paper Research Journal*, 27:237–244.
- Flournoy, D. S., Kirk, T. K., and Highley, T. L. (1991). Wood decay by brown-rot fungi: Changes in pore structure and cell wall volume. *Holzforschung*, 45:383–388.
- Fratzl, P. and Weinkamer, R. (2007). Nature's hierarchical materials. *Progress in Material Science*, 52:1263–1334.
- Fuhr, M. J., Stührk, C., Münch, B., Schwarze, F. W. M. R., and Schubert, M. (2012). Automated quantification of the impact of the wood-decay fungus *Physisporinus vitreus* on the cell wall structure of norway spruce by tomographic microscopy. *Wood Science and Technology*, 46:769–779.
- Gardiner, B., Leban, J.-M., Auty, D., and Simpson, H. (2011). Models for predicting wood density of british-grown sitka spruce. *Forestry*, 84:119–132.
- Gerhards, C. C. (1982). Effect of moisture content and temperature on the mechanical properties of wood: an analysis of immediate effects. *Wood and Fiber*, 14:4–36.
- Gindl, W. and Gupta, H. S. (2002). Cell-wall hardness and Young's modulus of melamine-modified spruce wood by nanoindentation. *Composites Part A: Applied Science and Manufacturing*, 33:1141–1145.
- Gindl, W., Gupta, H. S., and Grünwald, C. (2002). Lignification of spruce tracheid secondary cell walls related to longitudinal hardness and modulus of elasticity using nano-indentation. *Canadian Journal of Botany*, 80:1029–1033.
- Gindl, W., Gupta, H. S., Schöberl, T., Lichtenegger, H. C., and Fratzl, P. (2004). Mechanical properties of spruce wood cell walls by nanoindentation. *Applied Physics A: Materials Science & Processing*, 79:2069–2073.

- Glastrup, J., Shashoua, Y., Egsgaard, H., and Mortensen, M. N. (2006). Degradation of peg in the warship vasa. *Macromolecular Symposia*, 238:22–29.
- Gloimüller, S., de Borst, K., Bader, T. K., and Eberhardsteiner, J. (2012). Determination of the linear elastic stiffness and hygroexpansion of softwood by a multilayered unit cell using poromechanics. *Interaction and Multiscale Mechanics*, 5:229–264.
- Goodell, B. (2003). *Deterioration and Preservation: Advances in Our Changing World*, chapter Brown Rot Fungal Degradation of Wood: Our Evolving View, page 465p. American Chemical Society Series, Oxford University Press.
- Grønli, M. G., Várhegyi, G., and Blasi, C. D. (2002). Thermogravimetric analysis and devolatilization kinetics of wood. *Industrial and Engineering Chemistry Research*, 41:4201–4208.
- Groom, L., Mott, L., and Shaler, S. (2002). Mechanical properties of individual Southern pine fibers. Part I. Determination and variability of stress-strain curves with respect to tree height and juvenility. *Wood and Fiber Science*, 34:14–27.
- Hackspiel, C., de Borst, K., and Lukacevic, M. (2014). A numerical simulation tool for wood grading: model development. *Wood Science and Technology*, 48:633–649.
- Hafrén, J., Fujino, T., and Itoh, T. (1999). Changes in cell wall architecture of differentiating tracheids of *Pinus thunbergii* during lignification. *Plant Cell Physiology*, 40:532–541.
- Hafrén, J., Fujino, T., Itoh, T., Westermark, U., and Terashima, N. (2000). Ultrastructural changes in the compound middle lamella of *Pinus thunbergii* during lignification and lignin removal. *Holzforschung*, 54:234–240.
- Harrington, J. J., Booker, R., and Astley, R. J. (1998). Modelling the elastic properties of softwood. Part I: The cell-wall lamellae. *Holz als Roh- und Werkstoff*, 56:37–41.
- Hashin, Z. (1983). Analysis of composite materials: A survey. *Journal of Applied Mechanics*, 50:481–505.
- Hein, P. R. G. (2010). Multivariate regression methods for estimating basic density in eucalyptus wood from near infrared spectroscopic data. *Cerne*, 16:90–96.
- Hellmich, C., Barthélémy, J.-F., and Dormieux, L. (2004). Mineral-collagen interactions in elasticity of bone ultrastructure - a continuum micromechanics approach. *European Journal of Mechanics A/Solids*, 23:783–810.
- Heß, R. (1895). *Die Eigenschaften und das forstliche Verhalten der wichtigeren in Deutschland vorkommenden Holzarten. (in German)*. Parey, Berlin.

- Hill, C. A. S., Foster, S. C., Farahani, M. R. M., Hale, M. D. C., Ormondroyd, G. A., and Williams, G. R. (2005). An investigation of cell wall micropore blocking as a possible mechanism for the decay resistance of anhydride modified wood. *International Biodeterioration and Biodegradation*, 55:69–76.
- Hofstetter, K. and Gamstedt, K. (2009). Hierarchical modelling of microstructural effects on mechanical properties of wood. A review. *Holzforschung*, 63:130–138.
- Hofstetter, K., Hellmich, C., and Eberhardsteiner, J. (2005). Development and experimental validation of a continuum micromechanics model for the elasticity of wood. *European Journal of Mechanics A/Solids*, 24:1030–1053.
- Hofstetter, K., Hellmich, C., and Eberhardsteiner, J. (2007). Micromechanical modeling of solid-type and plate-type deformation patterns within softwood materials: A review and an improved approach. *Holzforschung*, 61:343–351.
- Howell, C., Steenkjær-Hastrup, A. C., Goodell, B., and Jellison, J. (2009). Temporal changes in wood crystalline cellulose during degradation by brown rot fungi. *International Biodeterioration and Biodegradation*, 63:414–419.
- Irvine, G. M. (1984). The glass transitions of lignin and hemicellulose and their measurement by differential thermal analysis. *Tappi Journal*, 67:118–121.
- Jäger, A., Bader, T. K., Hofstetter, K., and Eberhardsteiner, J. (2011a). The relation between indentation modulus, microfibril angle and elastic properties of wood cell walls. *Composites Part A: Applied Science and Manufacturing*, 42:677–685.
- Jäger, A., Hofstetter, K., Buksnowitz, C., Gindl-Altmutter, W., and Konnerth, J. (2011b). Identification of stiffness tensor components of wood cell walls by means of nanoindentation. *Composites Part A: Applied Science and Manufacturing*, 42:2101–2109.
- Jakes, J. E., Frihart, C. R., Beecher, J. F., Moon, R. J., Resto, P. J., Melgarejo, Z. H., Suarez, O. M., Baumgart, H., Elmustafa, A. A., and Stone, D. S. (2009). Nanoindentation near the edge. *Journal of Materials Research*, 24:1016–1031.
- Jakes, J. E., Frihart, C. R., Beecher, J. F., Moon, R. J., and Stone, D. S. (2008). Experimental method to account for structural compliance in nanoindentation measurements. *Journal of Materials Research*, 23:1113–1126.
- Kamke, F. A. and Lee, J. N. (2007). Adhesive penetration in wood - a review. *Wood and Fiber Science*, 39:205–220.
- Kačuráková, M., Capek, P., Sasinková, V., Wellner, N., and Ebringerová, A. (2000). Fr-ir study of plant cell wall model compounds: pectic polysaccharides and hemicelluloses. *Carbohydrate Polymers*, 43:195–203.
- Kelley, S. S., Rials, T. G., and Glasser, W. G. (1987). Relaxation behavior of the amorphous components of wood. *Journal of Materials Science*, 22:617–624.

- Kersavage, P. C. (1973). Moisture content effect on tensile properties of individual Douglas-fir latewood tracheids. *Wood and Fiber*, 5:105–117.
- Kim, J.-W., Harper, D. P., and Taylor, A. M. (2012). Technical note: Effect of embedment on micromechanical properties of brown-rot-decayed wood cell walls assessed with nanoindentation. *Wood and Fiber Science*, 44:103–107.
- Kirk, T. K. (1975). Effects of a brown-rot fungus, *Lenzites trabea*, on lignin in spruce wood. *Holzforschung*, 29:99–107.
- Kirk, T. K. and Highley, T. L. (1973). Quantitative changes in structural components of conifer woods during decay by white and brown rot fungi. *Phytopathology*, 63:1338–1342.
- Kleman-Leyer, K., Agosin, E., Conner, A. H., and Kirk, T. K. (1992). Changes in molecular size distribution of cellulose during attack by white rot and brown rot fungi. *Applied and Environmental Microbiology*, 58:1266–1270.
- Kohlhauser, C., Hellmich, C., Vitale-Brovarone, C., Rota, A., and Eberhardsteiner, J. (2009). Ultrasonic characterisation of porous biomaterials across different frequencies. *Strain*, 45:34–44.
- Kojima, Y. and Yamamoto, H. (2005). Effect of moisture content on the longitudinal tensile creep behavior of wood. *Journal of Wood Science*, 51:462–467.
- Kollmann, F. (1982). *Technologie des Holzes und der Holzwerkstoffe; Teil 1 (in German)*. Springer Verlag, Berlin Heidelberg New York.
- Konnerth, J., Eiser, M., Jäger, A., Bader, T., Hofstetter, K., Follrich, J., Ters, T., Hansmann, C., and Wimmer, R. (2010). Macro- and micro-mechanical properties of red oak wood (*Quercus rubra* L.) treated with hemicellulases. *Holzforschung*, 64:447–453.
- Konnerth, J., Gierlinger, N., Keckes, J., and Gindl, W. (2009). Actual versus apparent within cell wall variability of nanoindentation results from wood cell walls related to cellulose microfibril angle. *Journal of Materials Science*, 44:4399–4406.
- Konnerth, J., Harper, D., Lee, S. H., Rials, T. G., and Gindl, W. (2008). Adhesive penetration of wood cell walls investigated by scanning thermal microscopy (SThM). *Holzforschung*, 62:91–98.
- Koponen, T., Karppinen, T., Hæggström, E., Saranpää, P., and Serimaa, R. (2005). The stiffness modulus in Norway spruce as a function of year ring. *Holzforschung*, 59:451–455.
- Kröner, E. (1958). Berechnung der elastischen Konstanten des Vielkristalls aus den Konstanten des Einkristalls. *Zeitschrift für Physik*, 151:504–518.
- Lakes, R. (1993). Materials with structural hierarchy. *Nature*, 361:511–515.

- Laws, N. (1977). The determination of stress and strain concentrations at an ellipsoidal inclusion in an anisotropic material. *Journal of Elasticity*, 7:91–97.
- Lee, J.-W., Gwak, K.-S., Park, J.-Y., Park, M.-J., Choi, D.-H., Kwon, M., and Choi, I.-G. (2007a). Biological pretreatment of softwood *Pinus densiflora* by three white rot fungi. *The Journal of Microbiology*, 45:485–491.
- Lee, K.-H., Wi, S.-G., Singh, A. P., and Kim, Y.-S. (2004). Micromorphological characteristics of decayed wood and laccase produced by the brown-rot fungus *Coniophora puteana*. *Journal of Wood Science*, 50:281–284.
- Lee, S. H., Wang, S., Pharr, G. M., Kant, M., and Penumadu, D. (2007b). Mechanical properties and creep behavior of lyocell fibers by nanoindentation and nano-tensile testing. *Holzforschung*, 61:254–260.
- Leppänen, K., Andersson, S., Torkkeli, M., Knaapila, M., Kotelnikova, N., and Serimaa, R. (2009). Structure of cellulose and microcrystalline cellulose from various wood species, cotton and flax studied by X-ray scattering. *Cellulose*, 16:999–1015.
- Li, W., Wang, H., Wang, H., and Yu, Y. (2014). Moisture dependence of indentation deformation and mechanical properties of Masson pine (*Pinus massoniana* Lamb.) cell walls as related to microfibrillar angle. *Wood and Fiber Science*, 46:228–236.
- Lichtenegger, H. C., Müller, M., Wimmer, R., and Fratzl, P. (2003). Microfibril angles inside and outside crossfields of Norway spruce tracheids. *Holzforschung*, 57:13–20.
- Lichtenegger, H. C., Reiterer, A., Stanzl-Tschegg, S. E., and Fratzl, P. (1999). Variation of Cellulose Microfibril Angles in Softwoods and Hardwoods - A Possible Strategy of Mechanical Optimization. *Journal of Structural Biology*, 128:257–269.
- Lukacevic, M. and Füssl, J. (2014). Numerical simulation tool for wooden boards with a physically based approach to identify structural failure. *European Journal of Wood and Wood Products*, DOI 10.1007/s00107-14-0803-y.
- MacDonald, E. and Hubert, J. (2002). A review of the effects of silviculture on timber quality of Sitka spruce. *Forestry*, 75:107–138.
- Mäkinen, H., Mäkelä, A., and Hynynen, J. (2009). Predicting wood and branch properties of norway spruce as a part of a stand growth simulation system. Technical report, USDA Forest Service - General Technical Report PNW-GTR 791.
- Meng, Y., Wang, S., Cai, Z., Young, T. M., Du, G., and Li, Y. (2013). A novel sample preparation method to avoid influence of embeddig medium during nano-indentation. *Applied Physics A: Materials Science & Processing*, 110:361–369.
- Meylan, B. A. (1967). Measurements of microfibril angle by X-ray diffraction. *Forest Products Journal*, 17:51–58.

- Mittra, E., Akella, S., and Qin, Y.-X. (2006). The effects of embedding material, loading rate and magnitude and penetration depth in nanoindentation of trabecular bone. *Journal of Biomedical Materials Research*, 79:86–93.
- Moore, J. R., Lyon, A. J., Searles, G. J., and Vihermaa, L. E. (2009). The effects of site and stand factors on the tree and wood quality of Sitka spruce growing in the United Kingdom. *Silva Fennica*, 43:383–396.
- Mori, T. and Tanaka, K. (1973). Average stress in matrix and average elastic energy of materials with misfitting inclusions. *Acta Metallurgica*, 21:571–574.
- Niklas, K. J. (1992). *Plant Biomechanics - An Engineering Approach to Plant Form and Function*. The University of Chicago Press.
- Nix, W. D. and Gao, H. (1998). Indentation size effects in crystalline materials: a law for strain gradient plasticity. *Journal of Mechanics and Physics of Solids*, 43:411–425.
- Oliver, W. C. and Pharr, G. M. (1992). An improved technique for determining hardness and elastic modulus using load and displacement sensing indentation experiments. *Journal of Materials Research*, 7:1564–1583.
- Oliver, W. C. and Pharr, G. M. (2004). Measurement of hardness and elastic modulus by instrumented indentation: Advances in understanding and refinements to methodology. *Journal of Materials Research*, 19:3–20.
- Olsson, A.-M. and Salmén, L. (1997). Humidity and temperature affecting hemicellulose softening in wood. In *Proceedings of the International Conference of COST Action E8 "Mechanical Performance of Wood and Wood Products"*, pages 269–279.
- Olsson, A.-M., Salmén, L., Eder, M., and Burgert, I. (2007). Mechano-sorptive creep in wood fibres. *Wood Science and Technology*, 41:59–67.
- Page, D. H. (1976). A note on the cell-wall structure of softwood tracheids. *Wood and Fiber*, 7:246–248.
- Page, D. H., El-Hosseiny, F., and Winkler, K. (1971). Behaviour of single wood fibres under axial tensile strain. *Nature*, 229:252–253.
- Pandey, K. K. and Pitman, A. J. (2003). FTIR studies of the changes in wood chemistry following decay by brown-rot and white-rot fungi. *International Biodeterioration and Biodegradation*, 52:151–160.
- Peura, M., Müller, M., Vainio, U., Sarén, M.-P., Saranpää, P., and Serimaa, R. (2008). X-ray microdiffraction reveals the orientation of cellulose microfibrils and the size of cellulose crystallites in single Norway spruce tracheids. *Trees - Structure and Function*, 22:49–61.
- Plomion, C., Leprovost, G., and Stokes, A. (2001). Wood formation in Trees. *Plant Physiology*, 127:1513–1523.

- Qing, H. and Mishnaevsky, L. (2009). 3D hierarchical computational model of wood as a cellular material with fibril reinforced, heterogeneous multiple layers. *Mechanics of Materials*, 41:1034–1049.
- Raghavan, R., Adusmalli, R.-B., Buerkli, G., Hansen, S., Zimmermann, T., and Michler, J. (2012). Deformation of the compound middle lamella in spruce latewood by micro-pillar compression of double cell walls. *Journal of Materials Science*, 47:6125–6130.
- Reis, D., Vian, B., and Roland, J.-C. (1994). Cellulose-glucuronoxylans and plant cell wall structure. *Micron*, 25:171–187.
- Reuss, A. (1929). Berechnung der Fließgrenze von Mischkristallen auf Grund der Plastizitätsbedingung für Einkristalle. *ZAMM - Journal of Applied Mathematics and Mechanics*, 9:49–58.
- Ross, R. J., editor (2010). *Wood Handbook - Wood as engineering material*. Forest Products Laboratory.
- Sakagami, H., Matsumura, J., and Oda, K. (2007). Shrinkage of tracheid cells with desorption visualized by confocal laser scanning microscopy. *IAWA Journal*, 28:29–37.
- Salmén, L. (1982). *Temperature and water induced softening behaviour of wood fiber based materials*. PhD thesis, The Royal Institute of Technology, Stockholm.
- Salmén, L. (2004). Micromechanical understanding of the cell-wall structure. *Comptes Rendus Biologies*, 327:873–880.
- Salmén, L. and Burgert, I. (2009). Cell wall features with regard to mechanical performance. A review. COST Action E35 2004-2008: Wood machining - micromechanics and fracture. *Holzforschung*, 63:121–129.
- Salmén, L. and de Ruvo, A. (1985). A model for the prediction of fiber elasticity. *Wood and Fiber Science*, 17:336–350.
- Sandström, M., Jalilehvand, F., Persson, I., Gelius, U., Frank, P., and Hall-Roth, I. (2002). Deterioration of the seventeenth-century warship vasa by internal formation of sulphuric acid. *Nature*, 415:893–897.
- Sarén, M.-P., Serimaa, R., Andersson, S., Paakkari, T., Saranpää, P., and Pesonen, E. (2001). Structural variation of tracheids in norway spruce (*Picea abies* [L.] karst.). *Journal of Structural Biology*, 136:101–109.
- Savitzky, A. and Golay, M. J. E. (1964). Smoothing and differentiation of data by simplified least squares procedures. *Analytical Chemistry*, 36:1627–1639.
- Schmidt, O. (2006). *Wood and Tree Fungi: Biology, Damage, Protection, and Use*. Springer Verlag, Berlin Heidelberg New York.

- Schwanninger, M., Rodrigues, J. C., Pereira, H., and Hinterstoisser, B. (2004). Effects of short-time vibratory ball milling on the shape of FT-IR spectra of wood and cellulose. *Vibrational Spectroscopy*, 36:23–40.
- Schwarze, F. W. M. R. (2007). Wood decay under the microscope. *Fungal Biology Reviews*, 21:133–170.
- Sedighi-Gilani, M., Sunderland, H., and Navi, P. (2005). Microfibril angle non-uniformities within normal and compression wood tracheids. *Wood Science and Technology*, 39:419–430.
- Sedighi-Gilani, M., Sunderland, H., and Navi, P. (2006). Within-fiber nonuniformities of microfibril angle. *Wood and Fiber Science*, 38:132–138.
- Segal, L., Creely, J. J., Martin, A. E., and Conrad, C. M. (1959). An empirical method for estimating the degree of crystallinity of native cellulose using the X-ray diffractometer. *Textile Research Journal*, 29:786–794.
- Senft, J. F. and Bendtsen, B. A. (1985). Measuring microfibrillar angles using light microscopy. *Wood and Fiber Science*, 17:564–567.
- Shishkina, O., Lomov, S. V., Verpoest, I., and Gorbatikh, L. (2014). Structure-property relations for balsa wood as function of density: modelling approach. *Archive of Applied Mechanics*, DOI 10.1007/s00419-014-0833-2.
- Skaar, C. (1988). *Wood-Water Relations*. Springer Verlag, Berlin Heidelberg New York.
- Stelte, W., Clemons, C., Holm, J. K., Ahrenfeldt, J., Henriksen, U. B., and Sanadi, A. R. (2011). Thermal transitions of the amorphous polymers in wheat straw. *Industrial Crops and Products*, 34:1053–1056.
- Stevanic, J. and Salmén, L. (2009). Orientation of the wood polymers in the cell wall of spruce wood fibers. *Holzforschung*, 63:497–503.
- Struik, L. C. E. (1987). The mechanical and physical ageing of semicrystalline polymers: 1. *Polymer*, 28:1521–1533.
- Sundberg, A., Sundberg, K., Lillandt, C., and Holmbom, B. (1996). Determination of hemicelluloses and pectins in wood and pulp fibers by acid methanolysis and gas chromatography. *Nordic Pulp & Paper Research Journal*, 11:216–219.
- Suquet, P. (1987). *Homogenization Techniques for composite media*, chapter Elements of homogenization for inelastic solid mechanics, pages 109–143. Springer Verlag, Wien New York.
- Suquet, P., editor (1997). *Continuum Micromechanics*. Springer New York Wien.

- Svedström, K., Bjurhager, I., Kallonen, A., Peura, M., and Serimaa, R. (2012). Structure of oak wood from the Swedish warship Vasa revealed by X-ray scattering and microtomography. *Holzforschung*, 66:355–363.
- Swadener, J. G. and Pharr, G. M. (2001). Indentation modulus of elastically anisotropic half-spaces by cones and parabolae of revolution. *Philosophical Magazine A*, 81:447–466.
- TAPPI Test Method T222 (1988). Acid-Insoluble Lignin in Wood and Pulp. *Tappi Test Methods*, Technical Association of the Pulp and Paper Industry.
- Tashiro, K. and Kobayashi, M. (1991). Theoretical evaluation of three-dimensional elastic constants of native and regenerated celluloses: role of hydrogen bonds. *Polymer*, 32:1516–1526.
- Taylor, A. M., Gartner, B. L., and Morrell, J. J. (2002). Heartwood formation and natural durability - a review. *Wood and Fiber Science*, 34:587–611.
- Terashima, N., Yoshida, M., Hafrén, J., Fukushima, K., and Westermark, U. (2012). Proposed supramolecular structure of lignin in softwood tracheid compound middle lamella regions. *Holzforschung*, 66:907–915.
- Toba, K., Yamamoto, H., and Yoshida, M. (2013). Crystallization of cellulose microfibrils in wood cell wall by repeated dry-and-wet treatment, using X-ray diffraction technique. *Cellulose*, 20:633–643.
- Tze, W. T. Y., Wang, S., Rials, T. G., Pharr, G. M., and Kelley, S. S. (2007). Nanoindentation of wood cell walls: Continuous stiffness and hardness measurements. *Composites Part A: Applied Science and Manufacturing*, 38:945–953.
- VanLandingham, M. R., Villarrubia, J. S., Guthrie, W. R., and Meyers, G. F. (2001). Nanoindentation of polymers: an overview. *Macromolecular Symposia*, 167:15–43.
- Vihermaa, L. (2010). *Influence of site factors and climate on timber properties of Sitka spruce (Picea sitchensis [Bong.] Carr.)*. PhD thesis, University of Glasgow, Glasgow.
- Vlassak, J. J., Chiavarella, M., Barber, J. R., and Wang, X. (2003). The indentation modulus of elastically anisotropic materials for indenters of arbitrary shape. *Journal of Mechanics and Physics of Solids*, 53:1701–1721.
- Voigt, W. (1889). Über die Beziehung zwischen den beiden Elasticitäts-Constanten isotroper Körper. *Annalen der Physik*, 38:573–587.
- Wagner, L., Bader, T. K., Auty, D., and de Borst, K. (2013). Key parameters controlling stiffness variability within trees: a multiscale experimental-numerical approach. *Trees - Structure and Function*, 27:321–336.

- Wagner, L., Bader, T. K., and de Borst, K. (2014a). Nanoindentation of wood cell walls: Effects of sample processing and sample preparation. *Journal of Materials Science*, 49:94–102.
- Wagner, L., Bader, T. K., Eberhardsteiner, J., and de Borst, K. (2014b). Fungal degradation of softwood cell walls: enhanced insight through micromechanical modeling. *accepted by International Biodeterioration & Biodegradation*, DOI: 10.1016/j.ibiod.2014.05.010.
- Wagner, L., Bader, T. K., Ters, T., Fackler, K., and de Borst, K. (2014c). A combined view on composition, micromechanics and molecular structure of fungal degraded softwood. *revisions submitted to Holzforschung*.
- Wagner, L., Bos, C., Bader, T. K., Rautkari, L., and de Borst, K. (2014d). Effect of water on the mechanical properties of wood cell walls - results of a nanoindentation study. *submitted to Holzforschung*.
- Wang, S., Lee, S.-H., Tze, W. T. Y., Rials, T., and Pharr, G. M. (2006). Nanoindentation as a tool for understanding nano-mechanical properties of wood cell wall and biocomposites. In *Proceedings of International Conference on Nanotechnology for the Forest Product Industry, Atlanta, Georgia, USA, April 26-28, 2006*.
- Weinkamer, R. and Fratzl, P. (2011). Mechanical adaptation of biological materials - the examples of bone and wood. *Materials Science and Engineering C*, 31:1164–1173.
- Westad, F. and Martens, H. (2000). Variable selection in near infrared spectroscopy based on significance testing in partial least squares regression. *Journal of Near Infrared Spectroscopy*, 8:117–127.
- Wilcox, W. W. (1978). Review of literature on the effects of early stages of decay on wood strength. *Wood and Fiber*, 9:252–257.
- Wimmer, R. and Lucas, B. N. (1997). Comparing mechanical properties of secondary wall and cell corner middle lamella in spruce wood. *IAWA Journal*, 18:77–88.
- Wimmer, R., Lucas, B. N., Tsue, T. Y., and Oliver, W. C. (1997). Longitudinal hardness and Young's modulus of spruce tracheid secondary walls using nanoindentation technique. *Wood Science and Technology*, 31:131–141.
- Winandy, J. E. and Morrell, J. J. (1993). Relationship between incipient decay, strength and chemical composition of Douglas fir heartwood. *Wood and Fiber Science*, 25:278–288.
- Yang, J. L. and Evans, R. (2003). Prediction of MOE of eucalypt wood from microfibril angle and density. *Holz als Roh- und Werkstoff*, 61:449–452.
- Yelle, D. J., Wei, D., Ralph, J., and Hammel, K. E. (2011). Multidimensional NMR analysis reveals truncated lignin structures in wood decayed by the brown rot basidiomycete *Postia placenta*. *Environmental Microbiology*, 13:1091–1100.

- Yin, Y., Berglund, L., and Salmen, L. (2011a). Effect of steam treatment on the properties of wood cell walls. *Biomacromolecules*, 12:194–202.
- Yin, Y., Bian, M., Song, K., Xiao, F., and Xiaomei, J. (2011b). Influence of microfibril angle on within-tree variations in the mechanical properties of chinese fir (*Chunninghamia lanceolata*). *IAWA Journal*, 32:431–442.
- Yu, Y., Fei, B., Wang, H., and Tian, G. (2011). Longitudinal mechanical properties of cell wall of Masson pine (*Pinus massoniana* Lamb) as related to moisture content: A nanoindentation study. *Holzforschung*, 65:121–126.
- Zaoui, A. (2002). Continuum micromechanics. Survey. *Journal of Engineering Mechanics-ASCE*, 128:808–816.
- Zhang, B., Fei, B., Yu, Y., and Zhao, R. (2007). Microfibril angle variability in Masson pine (*Pinus massoniana* Lamb.) using X-ray diffraction. *Forest Studies in China*, 9(1):33–38.
- Zhang, X., Wang, Q. Z. S., Trejo, R., Lara-Curzio, E., and Du, G. (2010). Characterizing strength and fracture of wood cell wall through uniaxial micro-compression test. *Composites Part A: Applied Science and Manufacturing*, 41:632–638.
- Zhang, Y., Meng, Y., Wu, Y., Wang, S., Du, G., Jiang, H., and Zhou, Z. (2012). Effect of enzyme treatment on the mechanical properties of wood cell walls by nanoindentation. *BioResources*, 7:2249–2259.
- Zhou, C., Chui, Y. H., and Gong, M. (2012). Within-stem variation in wood properties of red pine (*Pinus resinosa* Ait.). *Wood and Fiber Science*, 44:412–421.
- Zienkiewicz, O. C. and Taylor, R. L. (2000). *The Finite Element Method, Fifth Edition, Volume 1: The Basis*. Butterworth Heinemann, Oxford.
- Zysset, P. K. (2009). Indentation of bone tissue: a short review. *Osteoporosis International*, 20:1049–1055.

Publications and Conference Contributions

Publications

Gečys, T., Daniūnas, A., Bader, T. K., Wagner, L., Eberhardsteiner, J.:
3D Finite element analysis of a new type of timber beam-to-beam connection and its experimental validation.
submitted to Engineering Structures, 2014.

Conference Papers

Wagner, L., Bader, T. K., de Borst, K., Ters, T., Fackler, K.:
Cell wall properties of softwood deteriorated by fungi: combined chemical analyses, FT-IR spectroscopy, nanoindentation and micromechanical modeling.
In: *Proceedings of the 44th Annual Meeting of the International Research Group of Wood Protection (IRG/WP 44)*, Stockholm, Sweden, 16/06/2013–20/06/2013 (Document number: IRG/WP 13-20527).

Conference Presentations and Posters

Wagner, L., Bader, T. K., Hofstetter, K., Fackler, K., Ters, T.:
Nanoindentation and micromechanical modeling to explore the mechanical performance of deteriorated softwood.
COST Action FP0802 Workshop – Hierarchical structure and mechanical characterization of wood, Helsinki, Finland, 24/08/2011–25/08/2011 (poster presentation).

Wagner, L., Bader, T. K., Fackler, K., Ters, T., de Borst, K.:
Fungal degradation of Scots pine (*Pinus sylvestris* L.) sapwood: micromechanical and microstructural characterization at the cell wall level.
7th Plant Biomechanics Conference, Clermont-Ferrand, France, 20/08/2012–24/08/2012 (poster presentation).

Wagner, L., Bader, T. K., de Borst, K.:
Mechanical properties of Scots pine (*Pinus sylvestris* L.) cell walls after fungal degradation: multiscale micromechanical modeling and experimental validation.
6th European Conference on Computational Methods in Applied Sciences (ECCOMAS 2012), Vienna, Austria, 10/09/2012–14/09/2012 (oral presentation).

Wagner, L., Bader, T. K., de Borst, K., Eberhardsteiner, J.:
Nanoindentation to study within-tree variability of wood cell wall stiffness.
29th Danubia Adria Symposium on Advances in Experimental Mechanics (DAS 29), Belgrade, Serbia, 26/09/2012–29/09/2012 (poster presentation).

Wagner, L., Bader, T. K., Auty, D., de Borst, K.:
Control parameters for within-tree variability of wood stiffness at different length scales: multiscale modeling and experimental investigations.
COST Action FP0802 Workshop – Micro-characterization of wood materials and properties, Edinburgh, Scotland, UK, 24/10/2012–26/10/2012 (oral presentation).

Wagner, L., Bader, T. K., de Borst, K., Ters, T., Fackler, K.:
Cell wall properties of softwood deteriorated by fungi: combined chemical analyses, FT-IR spectroscopy, nanoindentation and micromechanical modeling.
44th Annual Meeting of the International Research Group of Wood Protection (IRG/WP 44), Stockholm, Sweden, 16/06/2013–20/06/2013 (oral presentation).

Wagner, L., Bader, T. K., de Borst, K.:
Nanoindentation of wood cell walls: effects of different sample preparation methods.
30th Danubia Adria Symposium on Advances in Experimental Mechanics (DAS 30), Primošten, Croatia, 25/09/2013–28/09/2013 (poster presentation).

Curriculum Vitae

Personal Data

Name: **Dipl.-Ing. Leopold WAGNER**
Date of Birth: 26th November 1983
Place of Birth: Waidhofen/Ybbs, Austria
Nationality: Austrian
Current address: Leitermayergasse 50/9, 1180 Wien, Austria

Education

11/2010 – 06/2014 Doctoral studies in Civil Engineering at Vienna University of Technology, Vienna, Austria
09/2004 – 09/2010 Diploma Studies in Mechanical Engineering at Vienna University of Technology, Vienna, Austria
09/1998 – 06/2003 High School Student in Mechanical and Industrial Engineering, Waidhofen/Ybbs, Austria

Activities Abroad

07/2011 CISM Advanced School “Experimental and Theoretical Multi-scale Analysis of Materials and Structures”, International Centre for Mechanical Sciences (CISM), Udine, Italy.
09/2011–10/2011 Short Term Scientific Mission on “Microstructural Characterization of Fungal Deteriorated Pine Sapwood”, Max Planck Institute for Colloids and Interfaces, Potsdam-Golm, Germany

Awards

2009 Award for excellent performance as a student, granted by the Faculty of Mechanical and Industrial Engineering, Vienna University of Technology
2013 Ron Cockcroft Award, granted by the International Research Group on Wood Protection (IRG/WP)
2013 Award to Young Researcher, granted by the Danubia Adria Society for Advances in Experimental Methods